ABSTRACT

ANTHONY, JOHN MICHAEL Systematics of K-Auger Electron Production by 4 - 8 MeV Carbon Ions Following Collisions with Gas Targets. (Under the direction of Professors Steven M. Shafroth and Christopher R. Gould).

Absolute carbon K-Auger production cross sections for transitions with emitter rest frame energies between 200 and 300 eV were measured following 4 to 8 MeV collisions with H_2, He, Ne, and Ar at observation angles between 9.6° and 10.6° in the laboratory frame of reference.

Spectra were measured using the high resolution projectile electron spectrometer (HRPES). HRPES is a double pass electrostatic parallel plate spectrometer having an 8 x 53 mm exit window and a position sensitive micro-channel plate detector equipped with a resistive anode encoder. Doppler broadening of electron spectra from the fast ion beam was overcome by positioning the detector at a calculated refocusing position.

For incident beams of two electron ions (C^{4+}), single electron capture into various n,ℓ orbital vacancies ($n \geq 2$) of incident $C^{4+}(1s2s\ ^3S)$ metastable ions was the primary mechanism giving rise to the observed transitions. Cross section measurements for single electron capture into n≥2, n=2 and n≥3 shells are presented and compared with a semi-classical Bohr-Lindhardt calculation. High resolution spectra showed that the $1s(2s2p\ ^3P)^2P$ - $1s^2\ ^1S$ transition was 2.7 times more intense than the $1s(2s2p\ ^1P)^2P$ - $1s^2\ ^1S$ transition, while the ratio of fractional parentage coefficients for these configurations is 3.00. The $1s2s^2\ ^2S$ - $1s^2\ ^1S$ transition was was only 12% as intense as the $1s(2s2p\ ^3P)\ ^2P$ - $1s^2\ ^1S$ transition but increased to 45% at 8 MeV. Assuming that electron capture into all L-shell orbital vacancies is equaly probable, the $1s2s^2\ ^2S$ - $1s^2\ ^1S$ transition, which results from capture into the single 1s vacancy of the incident $1s2s\ ^3S$ ions, should be equal

in intensity to the $1s(2s2p\ ^3P)\ ^2P$ - $1s^2\ ^1S$ transition, which occurs 1/6 of the time when an electron is captured into one of the 6 2p vacancies. Suppression of capture into the 2s sub-shell is thought to be due to the presence of the 2s spectator electron in the incident metastable ions.

Evidence of resonant and non resonant transfer and excitation (RTE and NTE respectively) in the production of excited $1s2p^2\ ^2D$ and $2s2p^2\ ^2D$ configurations following collisions of C^{4+} ions with helium and neon is also presented.

Systematics of K-Auger Electron Production by 4 - 8 MeV Carbon Ions Following Collisions with Gas Targets

by

John Michael Anthony

A thesis submitted to the Graduate Faculty of
North Carolina State University
in partial fulfillment of the
requirements for the degree of
Doctor of Philosophy in the

Department of Physics

Raleigh

1989

Approved By:

Chairman of Advisory Committee

Chairman of Advisory Committee

ACKNOWLEDGEMENTS

Although a single name appears on this thesis, this research project has been influenced by a number of important contributors. I have tried to compile at least a partial list below. My apologies are extended to anyone who's name does not appear. Any omissions are due to my poor memory and not to a lack of appreciation.

The most important and appreciated contributions to my professional and personal development during the course of this work were made by the members of my family. To my wife Alta, thanks for being my best friend when times were tough. To my sons Robert and John, I would like to say I love you very deeply. I regret not saying this enough over the past years. You are, have been and will always be the most important people in my life.

Thanks are also extended to all past and present members of the atomic collisions group at the University of North Carolina. Even though I was not a Carolina student, they always made me feel at home. Professor Stephen M. Shafroth, my mentor, has been a true friend and inspiration in every conceivable way. I thank him for his guidance, open mind, tolerance, and for providing a truly excellent environment in which to work. To Joseph Swenson who built the HRPES spectrometer, thanks for your excellent technical advice, help, and friendship. Thanks to Malika Benhenni who shared many late hours with me in the lab. To Professor Eugen Merzbacher, thanks for a wonderful atomic collisions course, for helpful comments during our weekly seminars, for lunch hour comradery, and also for taking my sons sailing. Thanks are also extended to Mark Clark and Mark Reed.

Many scientists have provided invaluable information, criticism and encouragement following my talks at APS conferences. Among them, I would especially like to thank Prof. Nico Stolterfoht, Patrick Richard, John Tanis and Joseph Macek.

I am very fortunate to have had the guidance of Professor Gary Mitchell, the Physics Department graduate administrator at NCSU. Rarely has an advisor had as much impact on

a student's development as he has had on mine. In addition to providing generous and honest guidance during the past 6 years, I consider him a very close friend.

Indispensable assistance in the later stages of this experiment was provided by David Peterson and Skip Hendrick of Francis Marrion College, Ed Strait of Macalester College, and Theo Zouros of Kansas State University.

The personnel at TUNL provided an excellent atmosphere of cooperation and friendship. A special thanks is extended to the director E. G. Bilpuch, the support staff including Sid Edwards, Paul Carter, and Bob Rummel, and to all of the Duke graduate students.

Finally, I would like to thank my present colleagues at the United States Naval Academy for their understanding and encouragement during the writing of this thesis. Special thanks to the department chairman Graham Gutsche, and to Professors Jim Huddle and Dave Correll.

Early stages of this work were supported by the Division of Chemical Sciences, U.S. Department of Energy, under contract No. De-AS05-78ER06027.

John M Anthony

March, 1989

TABLE OF CONTENTS

TABLE OF CONTENTS (CONTINUED)

LIST OF FIGURES

LIST OF FIGURES (CONTINUED)

1. INTRODUCTION

When a swiftly moving ion collides with a gas atom, several things may occur. Collision events are often classified as elastic or inelastic according to whether the total kinetic energy of the system (ion and target atom) is conserved or not. For example, elastic nuclear scattering measurements obtained by Geiger and Marsden[1,2,3] were used by Rutherford[4] in 1911 to establish the nuclear or planetary model of the atom. If the internal energy associated with electrons in the orbital cloud or the nuclear particles of either collision partner is affected, the collision is classified as inelastic since some kinetic energy is used in forming the excited atomic or nuclear state.

Naturally occuring radioactive elements provided the earliest source of fast ions for the study of atomic collision processes. However, the present technology for creating and accelerating ions involves an ion source, an ion accelerator as well as various magnetic steering and focusing elements. With these tools, a greater number of ionic species as well as absolute control of the ion's velocity are available for more selective collision studies. For example, a typical beam of C^{4+} ions accelerated to an energy of 6 million electron volts (MeV), is composed of carbon ions each containing 2 orbital electrons traveling at ~1 x 10^7 m/s in roughly the same direction.

In a single collision event, several processes can occur with varying degrees of probability. The excitation of an atomic orbital electron is, for example, much more likely than a nuclear excitation. It has become traditional to express inelastic transition probabilities in terms of a quantity known as the scattering cross section (σ) having units of area. Information about the quantum mechanical wave functions describing excited atomic or ionic states can be obtained by studying inelastic atomic cross sections as a function of various collision parameters. Obviously, both the projectile ion and target atom may become excited. From a theoretical point of view, the ideal experiment is one which measure as many properties of the collision as possible. These include the final excited

states of both the ion and the target atom, their recoil angles and their final charge states. Some recent experiments, for example, have studied the interference effect of nuclear excitations on atomic processes.

In the present work, decays of the projectile ion's electron cloud following collisions with a target atoms were observed. Such decays can proceed through the emission of either a photon or an electron. In these experiments, mono-energetic Auger electrons which were ejected during the decay of excited ions were observed using the High Resolution Projectile Electron Spectrometer (HRPES). Auger electron spectra are composed of various lines which peak at energies that depend on both the atomic number of the decaying ion and the configuration of its orbital electrons. A specification of the electronic configuration includes information about the number of orbital electrons, their distribution in the respective shells and sub-shells (eg 1s, 2s, 2p etc.), and the coupling of their spin and angular momenta .

Projectile electron spectroscopy (the study of decays from moving ions), although technically more difficult, has several advantages over target electron spectroscopy. Whereas most excited target states are formed through ionization, the probability of forming excited configurations through such processes as capture and excitation is much greater for ions than for neutral target atoms. In addition, modern ion sources are capable of producing micro-Ampere beams of almost any element in monatomic form, and the limitation of studying only a few naturally occurring monatomic target gases can be avoided. Lastly, foil or gas stripping of ions can be used in conjunction with magnetic selection to control the incident charge and, to some degree, the electronic configuration of the incident ion.

1.1 Decay Modes

The importance of the study of ion-atom collisions has been understood since the early part of the present century. In 1913, for example, Chadwick[5] and others recognized that atomic ionization was responsible for producing an x-ray line spectrum characteristic of a

particular target element when it was exposed to high energy alpha particles. In these studies, a photon is emitted when an outer shell orbital electron jumps to fill a vacancy created by the ionization of an inner shell electron due to the passage of the alpha particle through the orbital cloud.

Auger decay, or the emission of a mono-energetic electron from excited atomic configurations, was first observed and interpreted by Pierre Auger[6,7]. As a graduate student in 1922, Auger helped construct the first Wilson cloud chamber built in France. This device allowed the tracks of electrons, ions and atoms to be made visible as vapor tracks formed along the trajectories of the charged particles. He later built a second cloud chamber in hopes of measuring the angular distribution of photo-electrons ejected from a target atom after bombardment by x-rays[8]. However, Auger was surprised to find that the tracks seemed to occur only in multiplets with one having a variable length and the others having fixed lengths. He found that the length of the mono-energetic electron tracks were characteristic of the target element and that their yield depended on the target atomic number. On pursuing this "bavure sans importance", he was lead to conclude that certain excited ions could decay by a spontaneous emission of an electron and postulated that autoionization resulted from the conversion of atomic potential energy into kinetic energy of the autoionized electron.

Auger's picture was confirmed theoretically by G. Wentzel[9] who in 1927 presented the non-relativistic formalism for the Auger effect and confirmed that the mutual repulsion between electrons could serve as a mechanism for energy transfer between the jumping electron and an outer shell electron.

Although x-ray emission is the decay mode generally associated with atomic decays, it has been pointed out[10] that radiative decay is dominant only for K and L shell transitions from atoms with atomic number between 32 and 83. Auger yields (a) and fluorescence yields (ω) are quantities which reflect the relative strength of these decay modes:

(1.1) $\omega + a + o = 1$

o represents yields from other decay modes including Coster - Kronig[11], Super Coster Kronig[12], and higher order Auger transitions[13]. These competing decay modes are illustrated in figure 1.

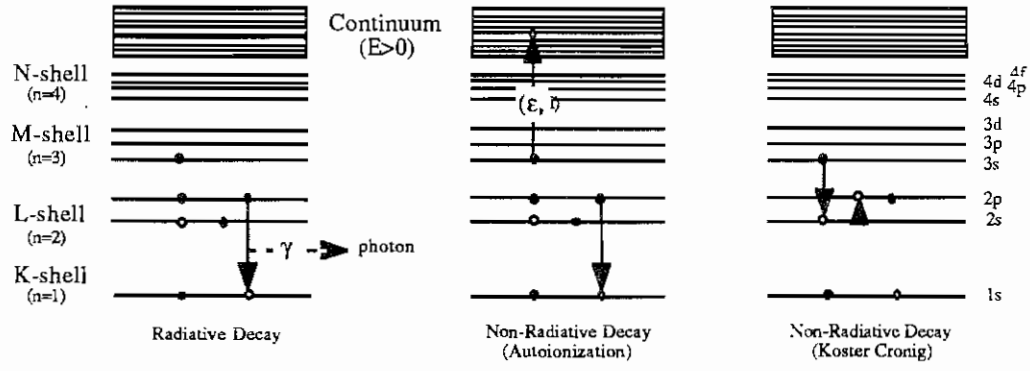

Figure 1 Illustration of the various decay modes for an excited configuration

1.2 Review of Relevant Research

Since Chadwick's early studies of the line spectra of x-rays emitted by excited atoms and of the dependance of spectral properties on collision conditions, an enormous mass of data has been collected. Although a number of broad issues have been pursued, several differences and similarities can be identified.

The objective of these investigations can roughly be divided into three categories: 1) measurement of the energy differences between atomic levels; 2) measurement of transition rates for atomic decays, and 3) measurement of the probabilities of forming excited atomic states.

In addition, an assortment of methods have been used to achieve these goals. Since the decay of ions or atoms can proceed by either photon or Auger electron emission; the experimental techniques can be broadly categorized as either x-ray or Auger spectroscopy. Often, the yield of one decay mode is small, and the experimental technique of choice is pre-determined by the collision system, or by the particular configuration of interest. Also, since x-ray emission is a relatively slow process as compared to Auger emission[14] the

natural width of an x-ray lines is much less than that of the corresponding Auger line. In this sense, x-ray spectroscopy is better suited for determining decay energies. It is, however, an accepted fact that an increase in x-ray resolution results is accompanied by a corresponding decrease in detection efficiency. This problem is not as severe in Auger spectroscopy where only an electric or magnetic field is required to separate the charged electrons so that improved resolution can easily be implemented by increasing the field strength.

Further differences in experimental technique can be identified with the method used to produce the excited configurations. They include bombardment of an atomic system by electrons, ions and photons. The formation of excited states through heavy ion bombardment, was chosen in this work partly since strict selection rules do not apply to these excitations and many configurations which are not readily populated by photon or electron impact are easy to produce. Photon impact excitation of core electrons is most difficult and generally limited to electric dipole (E1) transitions having selection rules:

(1.2) $\Delta L = L_f - L_i = \pm 1 \qquad \Delta M = M_f - M_i = \pm 1 \qquad \Delta J = J_f - J_i = \pm 1 \qquad \Delta\pi = \pi_f - \pi_i = \pm 1$

That similar restrictions apply to electron impact has already been noted by Mehlhorn[15].

1.2.1 Projectile Auger Spectroscopy

In this section, several recent experiments in the field Auger spectroscopy will be described. However, due to the abundance of research in this field and the limited scope of this work, the following is not intended to serve as a complete review of the field. Instead, the interested reader is referred to several recent review articles[16].

In the late 1960's and early 1970's, I. A. Sellin and collaborators were among the first to investigate Auger electrons emitted during in-flight-decays by ions excited in collisions with thin foil targets[17]. By studying the intensity of Auger electron emission as a function of distance from a the foil, Sellin was able to measure lifetimes and transition energies of the metastable $1s2s2p\ ^4P - 1s^2\ ^1S$ decays of various elements[18]. Although this was a valuable technique for studying lifetimes, prompt Auger transitions were not studied.

Within the dense target foil each ion would experience many collisions and a rich spectrum of excited ionic configurations would be produced with high probability. The spectra of Auger electrons emitted by ions as they emerged from the foil surface were impossible to interpret due to line blending (many decays having nearly the same energy). The line blending problems were further complicated by collisional broadening as a result of energy straggling of ions within the foil.

Schneider et. al. showed that these problems could largely be overcome by using sufficiently fast and highly stripped ions[19,20]. Since energy differences between excited K and L shell configurations are greatest, and since high velocity collisions limit the formation of excited configurations to those shells, the resulting projectile decay spectra are composed of fewer and more dispersed transitions. In flight decays from excited projectiles were measured following 2 MeV collisions of carbon ions with thin ($5\mu gm/cm^2$) carbon foils. A complete identification of lines found in the prompt Auger electron spectra was given, and transition energies were determined to within a few tenths of an eV. The success in identifying these K-Auger transitions, was due in part to ab initio energy calculations by the authors for a host of excited configurations. Many transition energies and line identifications were useful in identifying carbon K-Auger transitions the early stages of the present work.

Experimental accuracy in determining Auger transition energies was improved in a landmark experiment by Rodbro et al[21]. Projectile Auger spectra were measured for low energy (0.1 MeV to 0.5 MeV)) beams of light ions (Li, Be, B and C) in collisions with helium and other noble gas targets. Low Z (Z ≡ atomic number) ions were used as their Auger spectra contain fewer lines due to the small number vacancies in the incident ion. The effective thickness of the target was kept small enough to insure single collisions thus reducing ion straggling as well as other multiple collision problems. Berry potentials, space charge potentials and energy shifts caused by the kinematics of electron emission by

the moving ion were carefully taken into account in the absolute energy calibration of the spectral transitions.

The absolute energy calibration of the Rodbro's data was by Chung who employed his "saddle point" technique[22] to calculate the $1s2s2p\ ^4P \rightarrow 1s^2\ ^1S$ transition energy. This result was then used to re-calibrate the K-Auger electron spectra of boron and carbon[23,24]. Relativistic and mass polarization effects were included in Chung's calculations and a comparison with experimental measurements of the $1s2p^2\ ^4P \rightarrow 1s2s2p\ ^4P$ optical transition has helped establish these values as benchmark quality ($\lambda_{exp} = 1344.2 \pm 0.3$ Å compared to $\lambda_{Chung} = 1344.22$ Å).

Although the problem of line blending can be partially avoided by using highly stripped low Z ions, recent techniques have been developed to help further circumvent this problem. Since the primary cause is that lines corresponding to various projectile charge states all contribute strongly to the Auger spectrum, the solution is either to limit the number of post collision charge states or to use electron-ion coincidence techniques[25]. The coincidence techniques developed to date, however, are troubled by counting rates that are much too low for present high resolution spectrometers. Itoh et. al[26] were able to obtain Auger spectra for a particular projectile charge state by using low Z target atoms. This method has come to be known as ion surgery, and involves the selective excitation or ionization of a single inner shell projectile electron.

Electron capture has also been used to limit the charge state distribution of excited post collision ions. Before the collision, the ions are prepared in a highly stripped state so that a number of electron vacancies exist including the possibility of some K (or inner shell) vacancies. For both the K-vacancy bearing, and ground state ions, electron capture to an outer shell occurs 10^3 to 10^4 times more frequently than does excitation or ionization of an inner shell electron. Also, for the K vacancy bearing ions, the resulting post collision ion is almost always in an electronic configuration suitable for Auger decay. Experimenters at the MacDonald Laboratory of Kansas State University began studying Auger decay spectra

from excited configurations formed by electron capture early in the 1980's[27]. Vacancy bearing ions were prepared by passing fast fluorine ions through a thin carbon foil. In this process, a distribution of fluorine charge states are created as well as a number of excited configurations. In general, the excited configurations have a very short lifetime, and decay to the ground state before reaching the target cell located several meters from the foil. However, two-electron (He-like) ions formed by post stripping contain a strong component of the long lived 1s2s ^{3}S configuration that may survive the flight to the interaction region. Using experimentally measured values of metastable lifetimes, the Kansas group estimated that ~99.6% of the 9.5 MeV 1s2s ^{3}S F^{7+} beam produced in the stripping foil survive the 10 meter flight to the target cell before decay.

They were also able to measure the fraction, f_{3_S}, of the 1s2s ^{3}S component of ions produced by post stripping for several elements as a function of the beam energy[28]. A plot of the KSU group's metastable fraction vs. collision velocity for the various ionic species of He-like ions is shown in figure 2. The horizontal axis is actually the ratio of collision velocity to V_K -the velocity of an electron in the ion's K-shell. The solid line is a fit to the experimental data.

These measurements involve determining relative yields of Ti K-x-rays as a function of the ion's incident charge state. It relies on K-shell vacancy sharing between the projectile ions and atoms within a thin Ti foil, and has been discussed in detail elsewhere[29].

1.2.2 Simultaneous Transfer and Excitation

From a purely scientific view point, the motivation for research involving atomic transitions is to gain information about the principles governing the behavior of the atomic electron cloud. The laws of quantum mechanics have slowly emerged since the turn of the century and developed into a substantial theory to explain atomic processes. That experiment has played a vital role in this evolution would have been expected. However, the complexity of the mathematics involved in finding an exact solution for a system as simple as 3 electrons bound to a point nucleus renders the problem hopelessly difficult.

Figure 2 The fraction, $f_{^3S}$, of the 1s2s ^{3}S component for various incident two-electron ionic systems as a function of the ratio of the ion velocity to the ion's K-shell electron velocity. Taken from ref. 29.

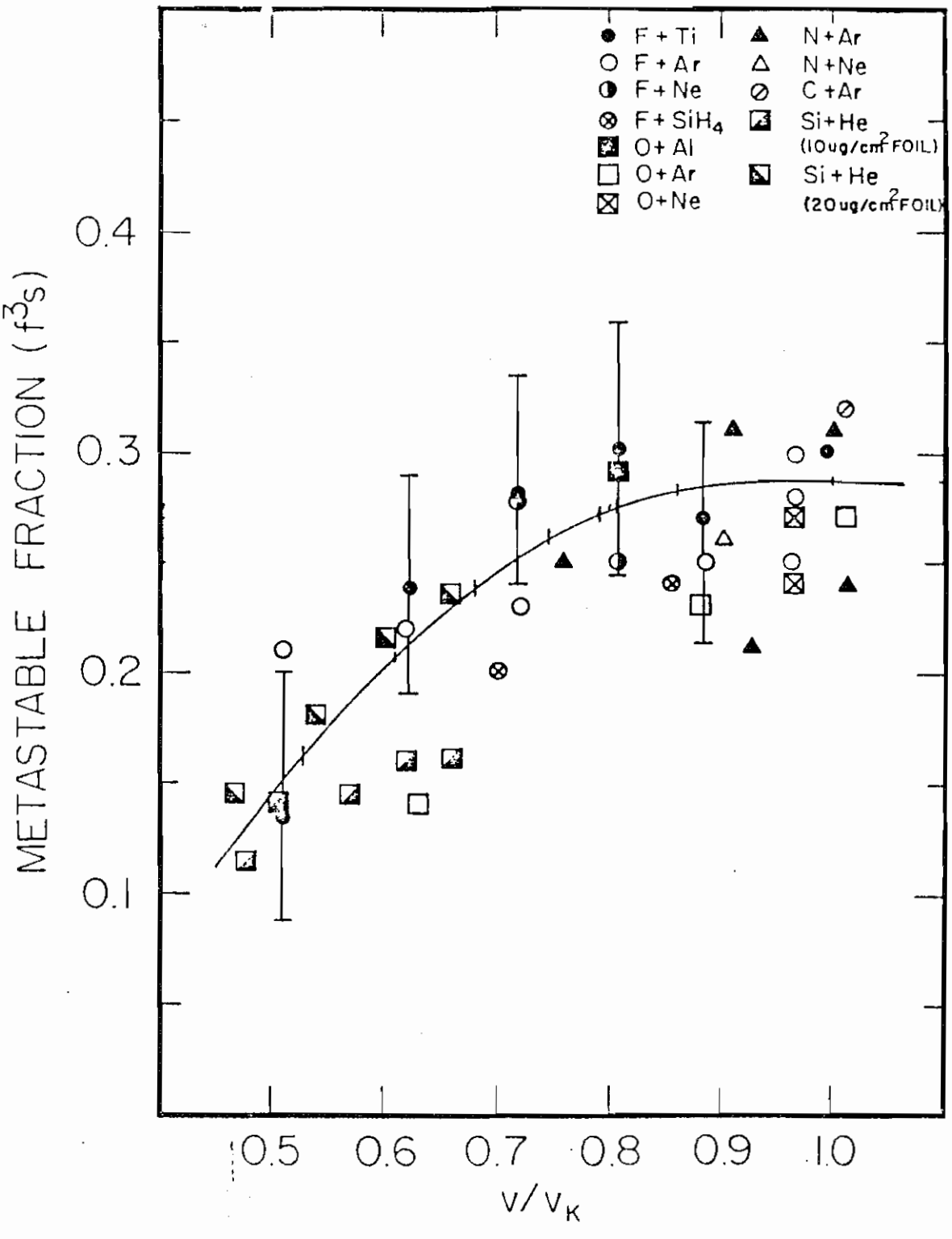
F + Ti
F + Ar
F + Ne
F + SiH4
O + Al
O + Ar
O + Ne
N + Ar
N + Ne
C + Ar
Si + He (10ug/cm2 FOIL)
Si + He (20ug/cm2 FOIL)
METASTABLE FRACTION (f3S)
0.4
0.3
0.2
0.1
0.5
0.6
0.7
0.8
0.9
1.0
V/VK

Figure 2

Instead, approximations are implemented to obtain a rough solution.

A number of atomic phenomena involving strong electron-electron potentials and unorthodox collision schemes, have been studied recently to gain insight into atomic excitation and decay mechanisms. They include: REC (radiative electron capture); DR (di-electronic recombination); and RTE (resonant transfer and excitation). In addition to the basic knowledge that a study of these exotic processes brings to atomic physics, there is a clear need for these measurements in many other areas such as the plasma fusion program.

For example, REC occurs when a free electron is captured into an inner shell of an ion and the ion emits a photon whose energy is equal to difference between, the relative kinetic energy of the electron before capture, and the potential energy of the bound electron (after capture). The DR process, on the other hand, occurs when an electron is captured into an inner shell and a second inner shell electron is promoted to a higher orbital. The resulting ion can then decay by emission of an x-ray. Photon emission via the REC and DR channels are leading causes of plasma energy loss, and can have a significant plasma cooling effect. DR has been called the inverse Auger effect since it is the time reversed process of atomic decay by electron emission.

In 1980, Tanis devised a method to measure a process analogous to DR[30]. Instead of using free electrons contained in a plasma or from an electron beam prepared in the laboratory, he proposed using electrons loosely bound to a target atom such as the orbital electrons of hydrogen or helium gas atoms, and a highly ionized beam of sulfur (Li-like S^{13+}) to play the role of the ions found in a hot plasma. In the Tanis scheme, a high velocity ion beam would pass through a gas cell of H_2 or He, capture a "nearly free" electron and convert the electron's relative kinetic energy into atomic potential energy by the promotion of a K-shell electron. This process has come to be known as RTE (resonant transfer and excitation) to distinguish it from a competing process, originally investigated by Pepmiller[31], known as NTE (nonresonant transfer and excitation).

Obviously, RTE is very similar to DR, however a few differences are worth emphasizing. In the DR environment (ie. a thermal plasma), the massive ions are relatively motionless, while the lighter electrons move rapidly. In RTE, the electrons are bound to nearly stationary atoms[32] while the ions move rapidly. Also, the motion of the electrons within the target atoms (ie. electron orbital motion) makes a significant contribution to the kinetic energy of the captured electron in the ion's rest frame.

RTE has been treated theoretically by Brandt[33] and Feagin[34], while MacLaughlin and Hahn[35] have calculated DR cross sections. Brandt showed that in the impulse approximation, RTE cross sections could be calculated from DR cross sections.

Although the coincidence technique employed by Tanis has provided clear proof for the existence of RTE as well as many interesting twists more detailed information can be obtained by studying this process using high resolution Auger spectroscopy.

Recently several experimenters have reported observing RTE in high resolution[36,37,38,39]. These measurements were in excellent qualitative agreement with theory, and have revealed new information which should further our understanding of the process.

A competing process (NTE) can result in production of the same excited configurations as RTE. In the NTE process, a target electron may be captured by the ion and a second electron may become excited in the same collision. Although this characterization is the same for both RTE and NTE, the difference lies in the manner in which the electron excitation takes place. In NTE, the excitation is driven by the time varying electric potential of the target nucleus, while in RTE it is driven by the field between the captured and excited electrons. As a result RTE is called a correlated process, while NTE is uncorrelated.

1.3 Objectives and Applications of the Present Work

The research that follows is concerned with measuring projectile Auger electron production cross sections from carbon ions which were excited in 3-8 Mev collisions with

thin gas targets of H_2, He, Ne, and Ar, and using them to infer various atomic process cross sections. Cross sections for simple electron capture into projectile n=2 shells (2s and 2p sub-shells), n=3 shells (3s,3p and 3d sub-shells), as well as n=4,5 shells were obtained. In addition, it was found that the production of several excitation configurations were most likely formed through higher order processes such as resonant and nonresonant transfer and excitation, and are often the result of strong electron-electron potentials.

The spectrometer used to measure Auger electron intensity vs. kinetic energy spectra was designed and constructed recently at the University of North Carolina at Chapel Hill. This High Resolution Projectile Electron spectrometer , or simply HRPES, is a tandem, 30° parallel plate electrostatic analyzer. The novel design and uniqueness of this spectrometer lies both in the manner in which electrons are detected and the method used to deal with spectral line broadening induced by kinematic effects. Conventional spectrometers utilize an exit slit which defines the spectrometer's intrinsic resolution. However, the HRPES has instead a .0.200 inch – .2.250 inch exit window cut in the base plate at the exit of the second stage field, and electrons are detected on a position sensitive micro-channel plate detector. The rectangular 8 – 50 mm micro-channel plate detector can be remotely positioned by two vacuum compatible, computer controlled, stepping motors so that the MCP distance from and angle with respect to the base plate exit window can be adjusted. This capability allows the detector to be remotely positioned along a calculated Doppler refocusing plane. The spectrometer and the principle of refocusing have been described previously[40].

In the early pages of this chapter, an attempted has been made to develop some of the fundamental reasons for the study of atomic collisions. Also, it was mentioned that RTE is closely related to DR and that both processes are of great interest in the magnetic confinement fusion program. A primary difficulty in the fusion program is the ability to achieve and sustain plasma temperatures sufficient for fusion. The need to minimize radiative energy loss mechanisms has created a strong demand for DR cross sections.

While direct measurements of DR cross sections have been plagued with experimental problems and generally limited to the least important outer shells, RTE measurements have been useful for checking recently calculated DR cross sections for inner shells. Furthermore, measured atomic collision cross sections can be used to interpret the intensities of spectral line emission giving information about local density, temperature, and ion mobility within the plasma.

As stated in a recent review article on the role of atomic spectroscopy[41] in astrophysics, most of our knowledge of the universe has come from the study of spectral lines emitted by astronomical objects. Indeed, since most of the universe is a plasma, atomic collision measurements are needed in astrophysics to infer solar temperatures, ion velocities and the abundance of elements in the universe. Metastable ions are of particular interest as noted in reference 41.

A rapidly growing and diverse set of needs for atomic structure information within the health care, energy and defense communities has created a specific demand for this information. In the health care field, the energy loss of highly charged ions in matter depend on ionization cross sections. Recent work on X-Ray lasers has shown that highly charged ions are perhaps the best hope for obtaining energetic correlated photon beams.

1.4. Summary

In chapter 2, the experimental apparatus will be presented. After sketching the various beam preparation facilities available at the Triangle Universities Nuclear Lab, the target leg apparatus, computer interface (including signal processing electronics) and spectrometer will be examined. A brief review of refocusing and improvement of spectrometer resolution by deceleration of electrons before the analyzer will be given.

The procedure used in the analysis of raw data is given in the following chapter. The presentation includes particulars about the normalization of measured yields into absolute Auger electron production cross sections. An examination of various spectrometer efficiency factors such as the efficiency vs position along the MCP detector and the effect

of electron deceleration are also included in chapter 3. Comparison will be made to similar measurements made in other laboratories.

Finally, the results will be presentedin chapter 4, and discussed in chapter 5.

2 EXPERIMENTAL METHOD

2.1 Ion Beam Preparation

Experiments were performed at the Triangle Universities Nuclear Laboratory (TUNL) located on the campus of Duke University in Durham, North Carolina. The facilities include a model FN tandem Van de Graaf capable of achieving up to 8 million terminal Volts for ion acceleration. A diagram of the TUNL accelerator bay appears in figure 3.

C^- ions were obtained from a high brightness sputter ion source[42] (SIS). Heat is applied to a reservoir containing cesium causing Cs atoms. As the Cs atoms migrate through a hot tungsten ionizer, the neutral atoms become ionized and C^- ions are produced when the Cs^+ beam is focused onto a graphite target cone. Large yields of C^- result since Cs^+ is a strong electron donor. Since a bias of -50 KV is applied to the SIS, the C^- ions are accelerated into the grounded beam pipe and subsequently are deflected into the accelerator tube by an electromagnet (M2 in figure 3). H^- beams were also needed for spectrometer efficiency calibration (see section 3.3.4). They were obtained from the "Dennis II" direct extraction plasma source (also shown in figure 3). A high voltage arc passing through low pressure H_2 gas within the Dennis II diode chamber produces various positive and negative charge states of Hydrogen including H^- ions.

When the ions reach the Van de Graaf terminal, they pass through a stripper canal containing low pressure oxygen gas (O_2). Some negative ions then become positively charged due to electron stripping. Assuming the incident charge to be -1, the energy of the ion beam (E_I) emerging from the accelerator is given by:

$$E_I = V_T (Q+1) \tag{2.1}$$

where Q is the charge of the positive ion after stripping, V_T is the accelerator terminal voltage and E_I is given in electron volts (eV). Since electron stripping from the individual ions in the beam is a statistical process, the positive beam emerging from the accelerator is composed of several components each having a characteristic charge state (Q) and ion energy (E_I).

Figure 3 Ion beam preparation at the Triangle Universities Nuclear Lab. The diagram shows equipment located in the accelerator bay including: the model FN tandem Van de Graaf accelerator; various negative ion sources; and magnetic elements used for beam focusing and steering.

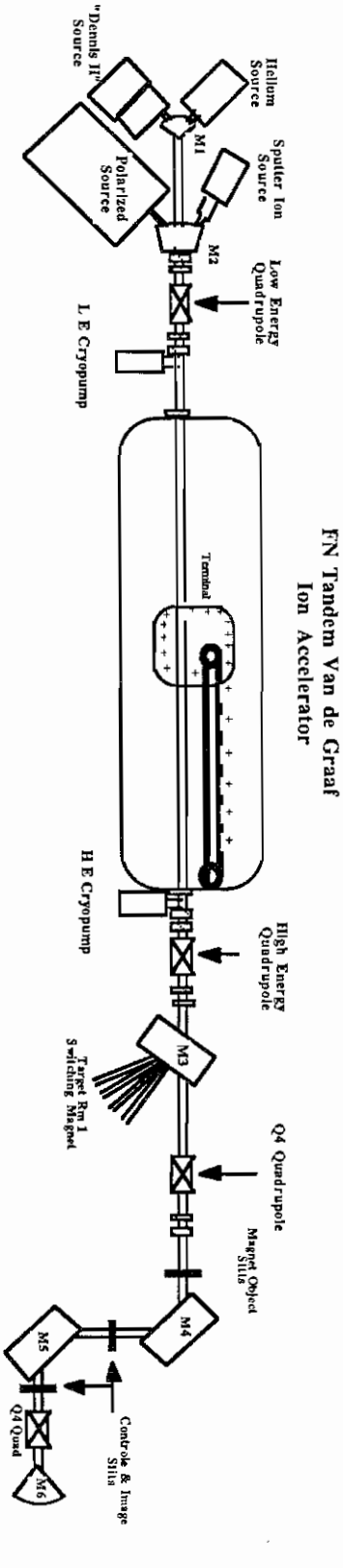
FN Tandem Van de Graaf
Ion Accelerator
"Dennis II" Source
Helium Source
Sputter Ion Source
Polarized Source
M1
M2
Low Energy Quadrupole
L E Cryopump
Terminal
H E Cryopump
High Energy Quadrupole
M3
Target Rm 1 Switching Magnet
Q4 Quadrupole
Magnet Object Slits
M4
M5
90-90 Magnet System
Q4 Quad
Control & Image Slits
M6
Target Rm 2 Switching Magnet

Figure 3

Selection of a particular component from the distribution of tandem charge states was accomplished using the 90° - 90° electromagnet system (M4 and M5 in figure 3). If the bending radius of the magnets (R) is known, the magnetic field strength (B) can be set to select ions having a characteristic mass (M_I), energy (E_I) and and charge (Q) :

$$(2.2) \quad B = \frac{\sqrt{2M_I E_I}}{QR}$$

For terminal voltages used in these experiments, the C^{2+} component was usually chosen since it was found to be the most intense. C^{4+} ions were obtained by post acceleration stripping. This was accomplished by lowering a thin carbon foil (~5μg/cm^2) into the path of C^{2+} beam emerging from the 90-90 system. The C^{4+} beam was then deflected into target room #2 by a final switching magnet (M6 in figure 4).

Focusing of the ion beam before the target leg was accomplished using the four magnetic quadrupole lenses also shown in figure 3. Magnetic steering elements located at both ends of the accelerator and 90-90 magnet system were used to maximize transmission through the accelerator and bending magnets.

A terminal feed-back amplifier system was used to help reduce periodic drifts in acceleration voltage. Control slits located at the exit of the 90-90 magnet system were used to locate the ion beam. Slit currents were read by a difference amplifier whose output was used as feedback to the terminal amplifier to lock the beam onto a desired energy.

2.2 Target Leg

Once an ion beam having the desired energy and charge had been prepared, it was deflected into the 70° target leg shown in figure 4. The target leg consists of elements used to position the beam along the transmission axis, the collision chamber containing the spectrometer and target cell, and a Faraday cup in which the beam is collected and measured.

The beam was brought to a focus at the target cell using using the Q7C and the target leg quadrupole lenses shown in figures 3 and 4 respectively. Pairs of vertical and horizontal

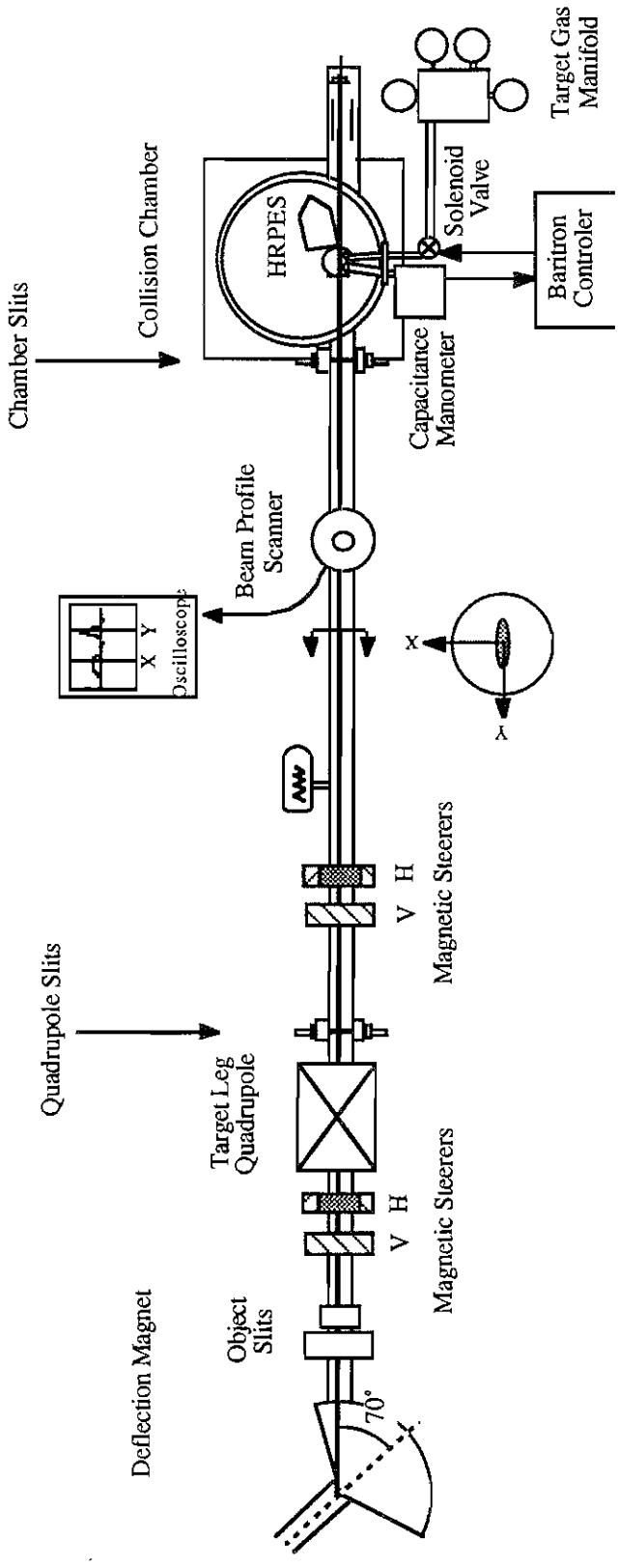

Figure 4 Experimental apparatus along the 70° leg located in target room #2.

magnetic steering elements (labeled V and H in figure 4) were needed to change the angle and position of the ion beam. The quadrupole and chamber collimation slits were carefully adjusted to limit the ion beam divergence and ensure that no ions were lost by beam scraping on the 0.375" x 0.375" exit aperture of the gas cell. This procedure helped insure that all ions able to emit Auger electrons within the spectrometer viewing region were collected in the Faraday cup.

Also shown in the figure is a beam profile scanner. Signals from the scanner were displayed on a standard oscilloscope so that the absolute position and the density profile of the ion beam could be inspected.

The 24" diameter collision chamber contained the HRPES spectrometer, the target cell, and the electron hot wire. The inside of the collision chamber was covered with 1/8" thick μ–metal shielding in order to annul any magnetic fields which might be found near the HRPES. Such fields can seriously perturb electron trajectories within the HRPES and degrade its resolution. This material is commonly used for magnetic shielding because of its large magnetic permeability. The target gas cell and the HRPES spectrometer are described in sections 2.2.1 and 2.2.2 below.

The hot wire provided a source of mono-energetic electrons needed for energy calibration (see section 3.1) and other tests. The hot wire consisted of two D.C. power supplies and a tungsten filament. A schematic is shown in figure 5. The intensity of electrons emitted from the filament could be controlled by adjusting the 0 - 20 Volt filament (V_F) supply, while the energy of the electrons was set using the 0 - 1000 Volt bias supply (V_B). The filament and ground plate were mounted on the end of a rod which extended through the wall of the collision chamber so that it could be rotated into the test position while the chamber was at vacuum and could be rotated out of the path of the beam during runs.

After exiting the collision chamber, ions were collected in an electrically isolated

Faraday cup and measured by a current integration device[43] (BCI meter). A suppressor ring, biased at ~ -1,000 Volts, was used to prevent false enhancement of ion current due to electrons being expelled from the entrance aperture of the cup.

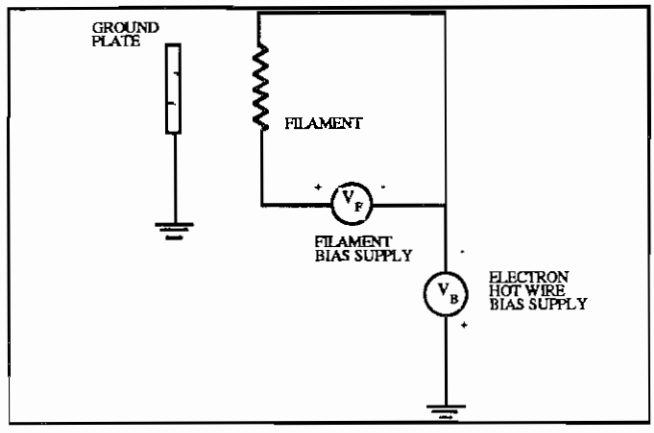

Figure 5 Electron hot wire schematic.

2.2.1 The High Resolution Projectile Electron Spectrometer

The HRPES is a tandem parallel plate analyzer consisting of a central plate (held at ground potential) and two deflection plates each maintained at the same negative plate voltage (V_P). Design parameters for the HRPES have been presented elsewhere along with a detailed treatment of its focusing properties (see reference 40). A diagram of the target cell, spectrometer and ion beam orientation is shown in figure 6. Spectrometer components were constructed from aluminum or stainless steel to minimize magnetic fields which may be found in ferrous metals.

Electrons in a uniform electric field travel in parabolic trajectories whose range (R) depends on the strength of the electric field (the field is given by $\frac{V_P}{s}$ where s is the separation between the base plate and deflection plate), the angle (ϕ) with respect to the field at which electrons enter the spectrometer, and the electron's energy (E). The range can be calculated using the expression:

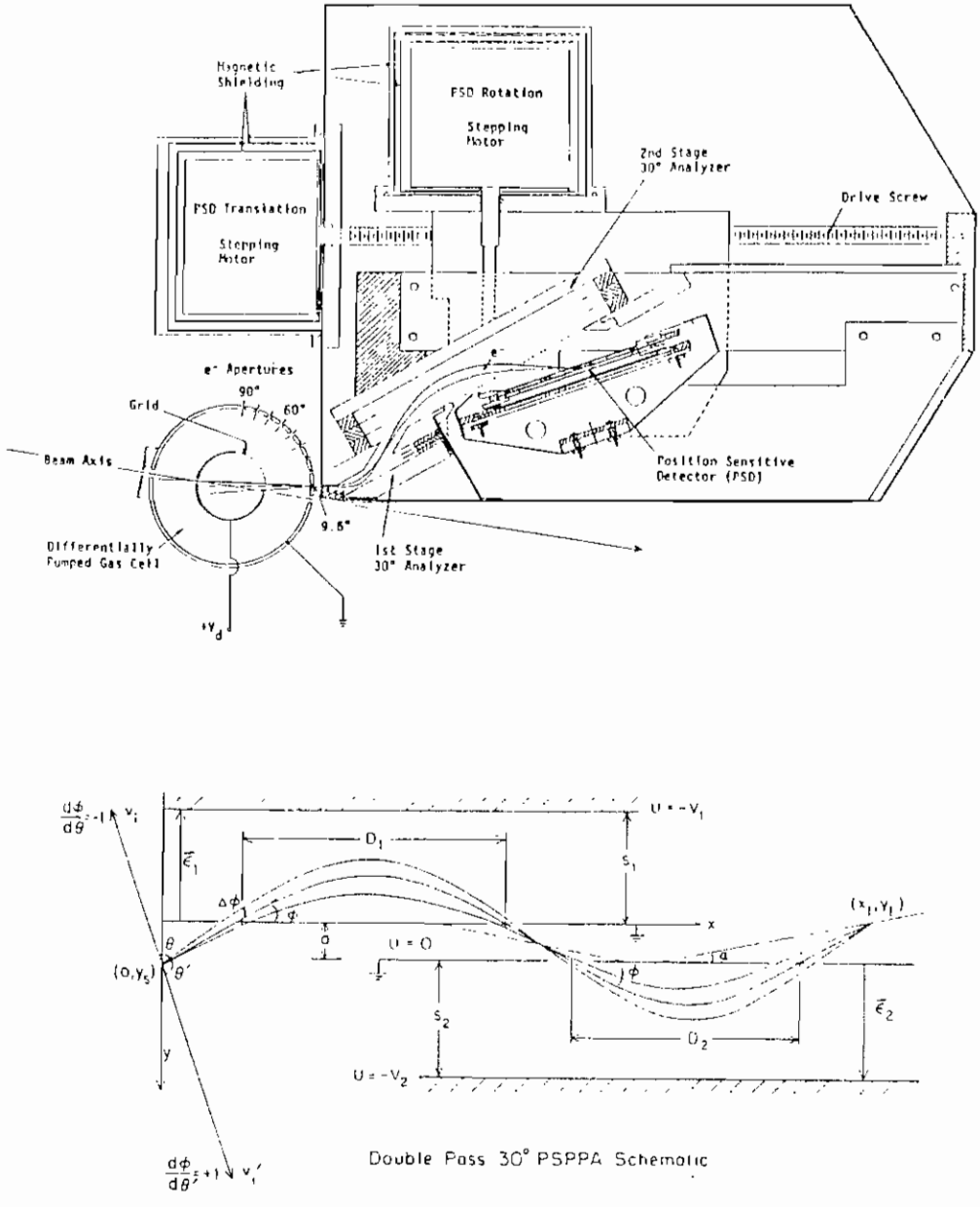

Figure 6 Schematic diagram showing the HRPES Parallel Plate Analyzer, differentially pumped target cell, and the beam - target - analyzer orientation.

$$R = 2E \frac{s}{e V_P} \sin 2\phi \qquad (2.3)$$

where e is the charge of an electron (1.6×10^{-19} C).

In most conventional parallel plate analyzers, electrons enter the analyzer field through a narrow slit in the ground plate and are recorded by a detector placed behind a similar exit slit located some distance R from the entrance slit. In such a set up, the range (R) and plate separation (s) are fixed. With V_P set at a given voltage, detection counts represent electrons having rather well defined energy given by equation (2.3). The combined width of the entrance and exit slits, however introduces some error (ΔR) into the range and consequently into the energy (ΔE) of the detected electrons. The quantity $\frac{\Delta E}{E}$ is known as the spectrometer resolution and slit widths are usually kept small in order to improve resolution. Slit width is usually ~1% of the range since extremely narrow slits limit spectrometer efficiency. Also, the range and slit widths fix the spectrometer entrance angle limits ($\phi_0 \pm \Delta\phi$).

A problem with the conventional electron spectrometer occurs when electron intensity is to be measured over a range of energies. The plate voltage is usually stepped or ramped in order to build a spectrum of counts vs. electron energy and a great deal of time is taken up in the process. The HRPES overcomes this problem by using a 53 mm exit window and a 50 mm position sensitive detector. The detector is equipped with a resistive anode device for position encoding (see section 3.2). Position sensitive detection has the advantage over a conventional analyzer of simultaneous detection of electrons over a range of electron energies and the need for scanning is eliminated. The HRPES is able to simultaneously detect electrons over an energy range covering 50% of the central energy. The central ray spectrometer constant which gives the ratio of the electron energy to the plate voltage needed to cause the electron to strike the center of the detector, was found to be 1.98. A dark count rate of ~ 1 count / second was measured with chamber vacuum of 8×10^{-6} Torr.

Since Auger spectra measured in this work can be seriously degraded by Doppler broadening effects (see section 3.4) and since electrons differing in energy by as much as 50% could be transmitted through the HRPES exit window, the intrinsic focusing properties of this analyzer were studied in detail. High energy resolution was obtained by positioning the detector at a calculated refocusing position and orientation. The detector position and angle relative to the spectrometer exit window was set by the two stepping motors shown in figure 6. The motors were located inside of a vacuum housing and kept at atmospheric pressure as they were not vacuum compatible. Annulment of the magnetic fields of the motor armatures was accomplished by lining the vacuum housings with μ-metal shielding.

Refocusing of electrons emitted by a moving projectile was first discussed by Bachmann et. al.[44] as a means of improving resolution. They derived the first order focusing condition and applied their technique to a conventional PPA in which spectra were acquired in a multiscaling fashion using a ramped deflection voltage. The concept of refocusing is based on finding a plane at which to place the detector such that the x coordinate of the electron trajectories is independent of ϕ. Referring to the schematic shown in figure 6, the expression for the x component of an electron trajectory is given by:

$$x = (2a + y_s - y)\cot\phi + \frac{2E}{V_P}(s_1 + s_2)\sin 2\phi \qquad (2.4)$$

a = separation distance between the first and second stage electric fields

y_s = the initial y coordinate of the emitted electron

V_P = the deflection voltage applied to the 1st and 2nd stage deflection plates

E = the electron energy in electron Volts

s_1 = the distance between the ground plate and the first stage deflection plate

s_2 = the distance between the ground plate and the second stage deflection plate

First order focusing is obtained when $\frac{\partial x}{\partial \phi} = 0$ which, together with (2.4) determines the y coordinate of the focal plane:

$$(2.5)\quad \frac{\partial x}{\partial \phi} = (2a + y_s - y_f)(-\csc^2 \phi) + \frac{2E}{V_P}(s_1 + s_2)\ (2\cos 2\phi) = 0$$

$$\text{or,}\quad y_f = 2a + ys - \frac{4E}{V_P}(s_1 + s_2)\sin^2 \phi \cos 2\phi$$

The x coordinate of the focal plane can be found in terms of y_f:

$$(2.6)\quad x_f = (2a + y_s - y_f)\cot \phi \left(1 + \frac{1}{\cos 2\phi}\right)$$

and the angle defined by the focal plane and the exit window is:

$$(2.7)\quad \tan \beta = \frac{\partial y_f}{\partial x_f} = -\tan \phi \ \frac{\cos 2\phi}{1 + \cos 2\phi}$$

Second order focusing occurs when $\frac{\partial^2 x}{\partial \phi^2} = 0$. This condition can only be satisfied for ϕ = 30° and results in a value of $\beta = -10.9°$.

For electrons emitted by a moving source, the situation becomes more complex. Swenson has shown that for moving sources the first order focusing condition is satisfied on a plane that is displaced a distance R_f from the focusing position for a stationary source:

$$(2.8)\quad R_F = \frac{4E}{V_P}(s_1 + s_2)\sin 2\phi \sin \phi \left(\frac{\sin \theta}{\sqrt{\frac{E}{\varepsilon}} - \cos \theta}\right)$$

and making an angle β with the exit window given by:

$$(2.9)\quad \tan \beta = -\left(\cot \phi - \frac{2K \sin 2\phi}{\partial y_f / \partial E}\right)$$

second order focusing could only be achieved at an observation angle of $\theta = 9.6°$.

2.2.2 The Target Gas Cell

The target cell assembly is composed of concentric aluminum cylinders having outer diameters of 1.0 and 2.5 inches. They are held in place by an insulating Teflon top piece which also contains a hole to allow target gas to flow into the inner cylinder, and a second hole so that target pressure can be monitored by a capacitance manometer. Target pressure was regulated using an electronic MKS model 220 control circuit which can maintain the cell pressure to within 1% of the set point value. Gas from the inner cell was able to escape into the region between the cells through the ion beam entrance and exit apertures and

through the spectrometer viewing slots shown in figure 6. To minimize contamination of the ion beam before the spectrometer viewing region, the target cell assembly was mounted over a 4 inch diffusion pump having a pumping speed of 500 liters/second. A second diffusion pump in the collision chamber was used to lower the chamber pressure and enhance spectrometer operation. A target gas manifold system was used so that the target gas could easily be changed from the control room using a panel of switches to open and close solenoid valves to the desired gas or to a mechanical pump which was used to remove old gas. In changing gases, the manifold was normally flushed two or more times while monitoring the manifold pressure to ensure the pressure between flushes was below ~3 mTorr.

Target pressures were chosen carefully to ensure single collision conditions. This is satisfied when the pressure is sufficiently low that ions interact with no more than one target atom in the trip through the target cell. Since the number of target atoms is directly proportional to the cell pressure, single collision conditions were ensured by observing the linearity of yield with target pressure. Pressure studies were made for all gases at a collision energies of 3 MeV for C^{4+} ions. Figure 7 shows the results of a typical pressure study.

The target cell assembly had provisions for spectrometer observation over a range of angles near the ion beam axis ($-2° \leq \theta \leq 13.5°$) and at 10° increments between 20° and 60°. Observation angles less than 9.4° were not used due to beam scraping on the corner of the spectrometer nearest the beam. The discrete viewing angles were defined by several 0.020" x 0.087" rectangular slots in the inner cell, and corresponding 0.063" x 0.200" slots in the outer cell. The central angle of these slots were carefully measured and found to be at θ = 19.5°, 28.7°, 39.9°, 49.6°, 59.8°.

Since the spectrometer entrance slits rotate about the central axis of the inner cell at a distance of 0.862 inches from the inner cell, the acceptance angle for the .020 in discrete

Figure 7 Experimental yield for the $1s(2s2p\ ^3P)\ ^2P$ - $1s^2\ ^1S$ (2_P+ top figure), $1s(2s2p\ ^1P)\ ^2P$ - $1s^2\ ^1S$ (2_P- middle figure), and the $1s2p^2\ ^2D$ - $1s^2\ ^1S$ Auger decays (2_D bottom figure) measured at various target pressures. Linearity of Auger yields ensures single collision conditions.

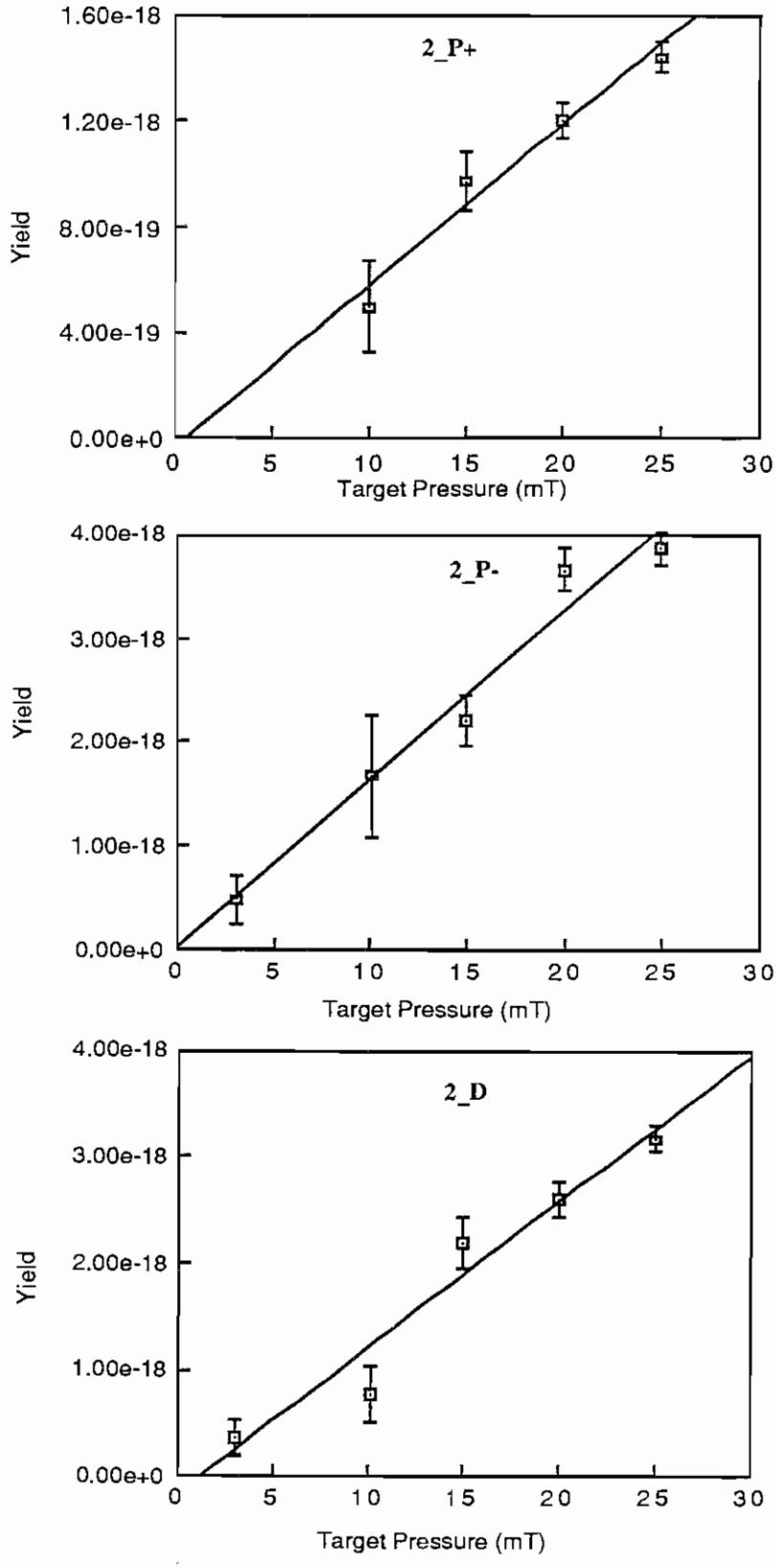
2_P+
Yield
1.60e-18
1.20e-18
8.00e-19
4.00e-19
0.00e+0
0
5
10
15
20
25
30
Target Pressure (mT)
2_P-
Yield
4.00e-18
3.00e-18
2.00e-18
1.00e-18
0.00e+0
Target Pressure (mT)
2_D
Yield
4.00e-18
3.00e-18
2.00e-18
1.00e-18
0.00e+0
Target Pressure (mT)

Figure 7

slots can be calculated:

(2.10) $$\alpha_{slot} = 2 \times \mathrm{Tan}^{-1}\left(\frac{0.010}{0.862}\right) = 1.328^\circ$$

For observation angles less than ~18.5°, the natural acceptance angle of the spectrometer ($\alpha_{HRPES} = 1.6^\circ$) was unrestricted.

Enhancement of spectrometer resolution was obtained by decelerating the Auger electrons before the analyzer. This was accomplished by biasing the target region defined by the inner cylinder of the target cell to a positive potential V_d. Electrons with energy E_A emitted in the decay of excited projectile ions are decelerated by the resulting electric field between the concentric cylinders of the target cell. The energy, E_A', of the electrons entering the analyzer is then given by:

(2.11) $E_A' = E_A - eV_d$

and the resulting spectrometer resolution $\Delta E_A/E_A$ is enhanced in proportion to the deceleration factor $F = E_A/E_A'$.

2.3 Computer Interface and Electronics

A diagram of the electronics is shown in figure 8. Electrons emerging from the HRPES second stage exit window are spatially dispersed so that their position along the detector is proportional to the electron's kinetic energy in the analyzer. The low and high energy ends of the detector are indicated in the figure (LE and HE respectively). The detector was composed of an array of individual micro-channels with each channel able to multiply an electron's charge much like a continuous dynode. Charge multiplication occurs when electrons collides with the curved channel wall and a spray of secondary electrons is emitted. Since a multiplication bias is applied to the detector so that the exit end of each curved channel is at +2000 Volts with respect to the entrance end, the primary and all secondary electrons accelerate progressively along through the channel and continue to create avalanches until the entire charge pulse is deposited on the Resistive Anode Encoder (RAE).

Figure 8 Signal processing electronics for the HRPES spectrometer. Pairs of Q_A and Q_B charge pulses result from charge division whenever an electron's multiplied charge is deposited on the resistive anode encoder. Two parallel sets of electronics modules produced fast NIM standard timing signals from each pair of Q_A and Q_B pulses. After introducing a 2μs time delay into the Q_A signal to ensure that the Q_B signal always leads, the time between pulses was measured by a time to voltage converter (0-2 μs time range; 0 - 8 V voltage range) whose output voltage was read by an Analog to Digital Converter and used to build an electron count vs TAC voltage spectrum in VAX memory. The numbered bubbles (eg. ⓝ) indicate outputs to the computer interface electronics shown in figure 9.

①	Q_A pulse height spectrum
②	Q_B pulse height spectrum
③	Q_A scaler counter
④	Q_B scaler counter
⑤	Strobe scaler counter
⑥	Timing spectrum

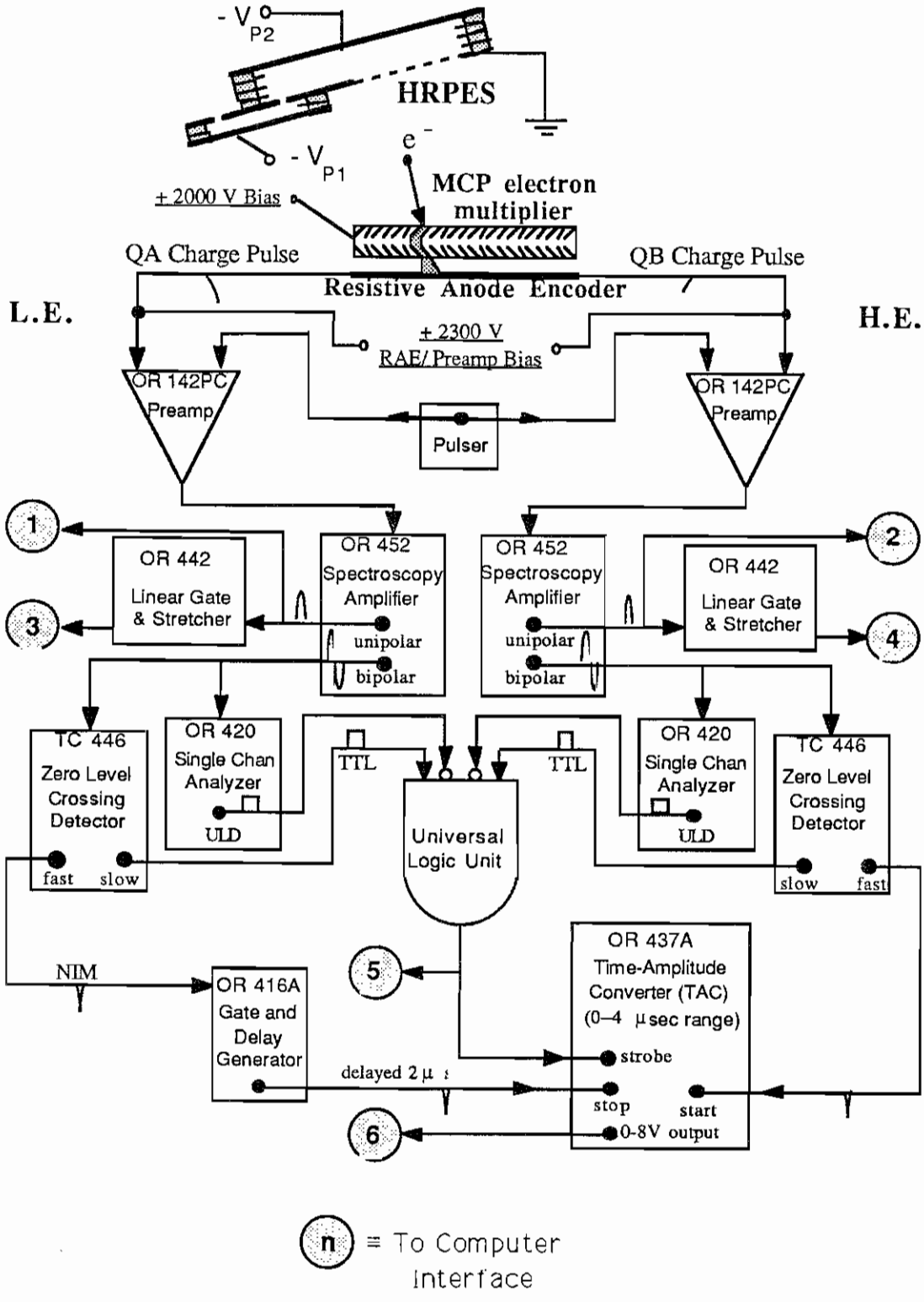
- V P2
HRPES
- V P1
e -
± 2000 V Bias
MCP electron multiplier
QA Charge Pulse
QB Charge Pulse
Resistive Anode Encoder
L.E.
H.E.
± 2300 V
RAE/ Preamp Bias
OR 142PC Preamp
Pulser
OR 142PC Preamp
1
2
3
4
OR 442
Linear Gate & Stretcher
OR 452
Spectroscopy Amplifier
unipolar
bipolar
OR 452
Spectroscopy Amplifier
unipolar
bipolar
OR 442
Linear Gate & Stretcher
TC 446
Zero Level Crossing Detector
fast
slow
OR 420
Single Chan Analyzer
ULD
TTL
TTL
Universal Logic Unit
OR 420
Single Chan Analyzer
ULD
TC 446
Zero Level Crossing Detector
slow
fast
NIM
OR 416A
Gate and Delay Generator
5
OR 437A
Time-Amplitude Converter (TAC)
(0–4 μsec range)
strobe
delayed 2 μ s
stop
start
6
0-8V output
n ≡ To Computer Interface

Figure 8

The HRPES electronics can be divided into two functional sections. The first section includes all electronics modules shown in figure 8, except the time to amplitude converter (TAC). The primary function of these modules is to generate pairs of fast rise time signals (ie. NIM standard signals) for each QA - QB pulse pair, and for generating a TTL strobe signal to enable the TAC. The second serves as the computer interface and extracts

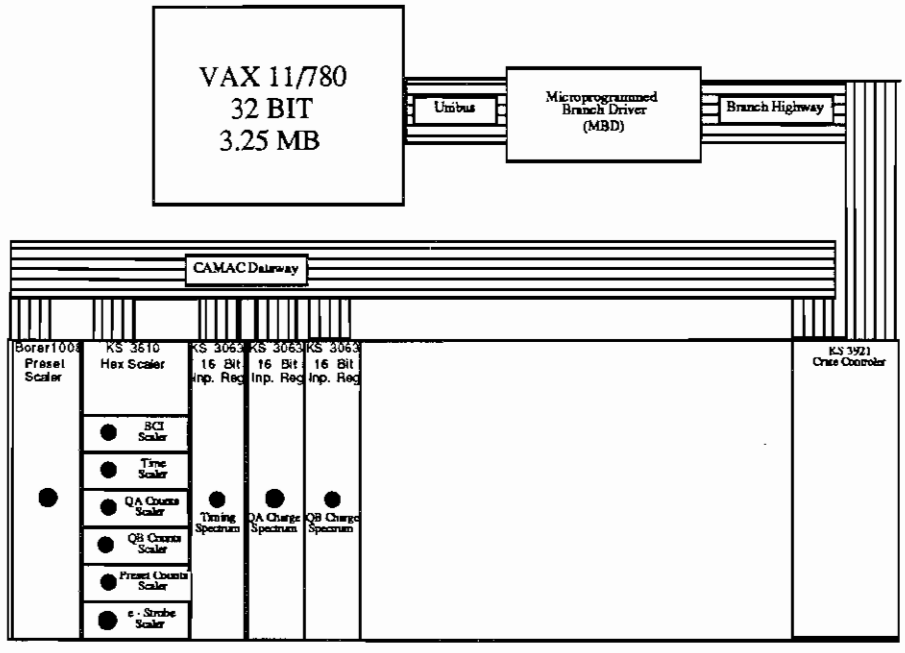

Figure 9 Schematic showing relevant components of the Triangle University Nuclear Laboratory's computer interface. A standard CAMAC interface is used.

position information from the time delay between the Q_A and Q_B pulses of each pair. The counts are physically transferred to the VAX via a standard CAMAC interface using a 32 bit microcomputer, known as an MBD, and a Unibus. The MBD was able to transfer data by direct memory access to global sections of VAX memory. Three spectra were measured for each run and were built from the incoming data by a VAX Data Acquisition Program (also known as a DAP file). The VAX interface electronics are illustrated schematically in figure 9.

It was necessary to take great care in matching the signal processing for Q_A and Q_B in order to obtain a high quality timing spectrum. Pulses from the Q_A and Q_B pre-amp outputs were amplified by identical Ortec model 452 spectroscopy amplifiers whose gains were carefully matched. In addition, pulse height spectra for Q_A and Q_B were recorded for every run. The four input universal logic unit shown in figure 8 provided the TAC strobe and was monitored by a KS-3610 50 MHz counter.

Since the lowest energy Carbon K-Auger transition observed in this work (at 227.2 eV) is only ~80 eV less than the highest energy transition (at ~300 eV), the amount of charge (Q) resulting from multiplication in the detector did not differ significantly for various Auger transitions. The 2000 Volt bias helped eliminate systematic errors such as those caused by pulse height discrimination level settings. The RAE is composed of a material having a uniform and isotropic resistivity, and each end is connected to the biased (+2300 V) input of an Ortec model 142PC fast pre-amp (~1×10^6 Hz count rate). The charge pulse Q divides into Q_A and Q_B pulses according to the resistance between Q and each pre-amp. Also, the RAE is capacitively coupled to ground so that the propagation velocity of pulses to the Q_A and Q_B pre-amps is given by:

(2.11) $v = \sqrt{k}\ c$

where k is the dielectric constant of the capacitor and c is the velocity of light. The total delay time across the RAE was determined by using a biased (typically, 200 V) hot wire as a source of monoenergetic electrons and scanning the spectrometer plate voltage to locate them on the LE edge of the detector. Pulses arriving at the HE edge were found to be delayed by 1.8 μsec with respect to those at the LE edge.

With hot wire electrons on the center of the MCP, the spectroscopy amplifier gains were adjusted so that the Q_A and Q_B distribution centroids are coincident. The Q_A and Q_B unipolar pulses were also counted in a scaler and could be compared with values from the TAC strobe scaler giving an indication of the amount of noise on each circuit.

The TUNL data acquisition interface is shown in figure 9, and a detailed description of the TUNL data acquisition system can be found elsewhere[45]. The interface system contains CAMAC[46] hardware and software to facilitate communication between the Crate Controller (CC) and various slave modules. In these experiments, a KS-3610 scaler was used to count pulses from:

1) the beam current intergater (BCI);

2) & 3) the unipolar output of the Q_A and Q_B spectroscopy amplifiers (raw Q_A counts and raw Q_B counts);

4) a 60 Hz clock(run time); and finally

5) TAC strobe pulses generated by the universal logic unit (e-strobe counts).

The scaler values for the various runs were recorded in a run log book and were not dumped to VAX memory. However, the Auger electron timing spectra and the Q_A and Q_B charge distribution spectra were saved. The spectra were dumped to disk files which were later copied to magnetic tape. They were measured using KS-3063 16 bit input/output registers after the pulses were digitized by Northern model 8192 ADC's. Although slower CAMAC compatible ADC's are available, the 100 MHz Northern ADC's eliminated the need for ADC dead time corrections. The length of the run was controlled by a Borer model 1008 count down preset scaler (50 MHz). The preset value could be software set before starting a run and the preset is decremented whenever a BCI pulse is sensed at its input. When the preset register reaches zero, the Borer raises an inhibit signal halting data taking by all CAMAC modules.

A Brookhaven model 1000 Current Integrater (BCI meter) was used to integrate ion beam currents collected in the target leg Faraday cup. This device produces TTL standard logic output pulses (BCI pulses) and each represents a unit of charge equal to the full scale current x 10^{-2} seconds. The BCI amplifier zero was carefully adjusted before connecting the Faraday cup coaxial cable at the start up of an experiment, and the input balance was

then adjusted with the cable connected, no ion beam current in the cup and the input scale set to the desired range (15 ranges from $2x10^{-9}$ to $2x10^{-2}$ Amperes full scale). An output is also provided for driving remote current indicating meters throughout the lab which were used to help maximize FC beam currents while adjusting the beam.

The TUNL data acquisition and analysis system software for the VAX 11/780 is known as XSYS and several comprehensive overviews of XSYS have appeared in the literature[47].

3 DATA ANALYSIS

The HRPES dispersed electrons along a 50 mm x 8 mm position sensitive MCP detector. A typical raw spectrum is shown in figure 10 (top figure). Spectra appear in a histogram format with the channel number on the horizontal axis representing detection position along the MCP and the vertical axis representing the total number of electrons detected. As discussed elsewhere (see pages 22 and 42), detection position was directly proportional to the kinetic energy of electrons on entering the HRPES analyzer. Auger electron spectra were accumulated and stored in global sections of computer memory known as data areas. Each data area was composed of 512 integers and each integer was 32 bits long.

Raw spectra were saved as Fortran files containing a series of numbers representing accumulated electron counts in the 512 consecutive bins of the data area. The files were then read into a software package known as Speakeasy[48], and stored as 2 x 512 data arrays. The first row of the "raw" array contained the column, or bin number (1 through 512). The second row contained the number of Auger electron counts accumulated in each bin. In Speakeasy, various steps in the data analysis process such as energy calibration, background fitting, normalization, kinematic transformation of Auger electron intensity and kinetic energy were facilitated by the structure and special functions of the Speakeasy language.

Reflection of signals at the MCP edges caused false "noise peaks" to appear in the spectrum. The first step in data analysis was to "chop" the spectrum by setting several of the initial and final elements of the raw data array to zero. The portion of the spectrum to be deleted was located visually using a cursor and a plot of the raw spectrum on a graphics terminal. Also, it can be seen that the background "plateau" in figure 10 has been subtracted from the raw spectrum. This undesirable characteristic is caused by delta

Figure 10 Auger electron spectra shown at various stages of analysis. The transition lines arise from the decays of various excited configurations of ionic carbon following 3 MeV collisions of C^{2+} with Ne. Line identification in terms of the excited and ground electronic configurations are, from left to right :

$1s2s^2\ ^2S \rightarrow 1s^2\ ^1S$ (227.2 eV)

$1s2s2p\ ^4P \rightarrow 1s^2\ ^1S$ (229.6 eV)

$1s(2s2p\ ^3P)\ ^2P_+ \rightarrow 1s^2\ ^1S$ (235.5 eV)

$1s(2s2p\ ^1P)\ ^2P_- \rightarrow 1s^2\ ^1S$ (238.2 eV)

$1s2p^2\ ^2D \rightarrow 1s^2\ ^1S$ (242.2 eV)

$1s2s^22p\ ^3P \rightarrow 1s^2\ ^1S$ (243.4 eV)

$1s2s2p^2\ ^1D \rightarrow 1s^2\ ^1S$ (249 eV)

$1s2s2p^2\ ^3D \rightarrow 1s^2\ ^1S$ (252.6 eV)

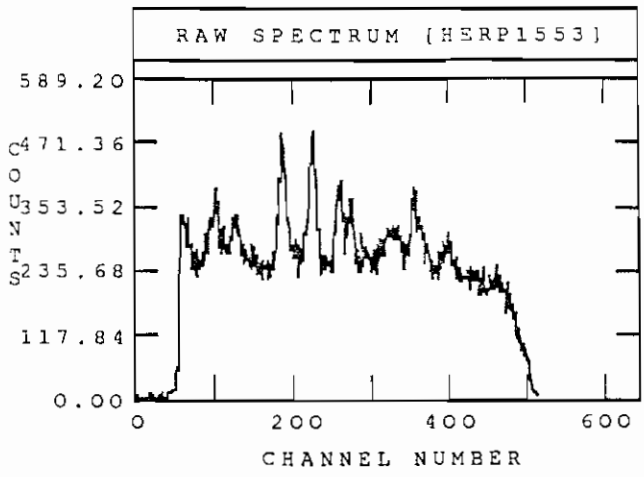
RAW SPECTRUM [HERP1553]
589.20
471.36
353.52
235.68
117.84
0.00
COUNTS
0
200
400
600
CHANNEL NUMBER

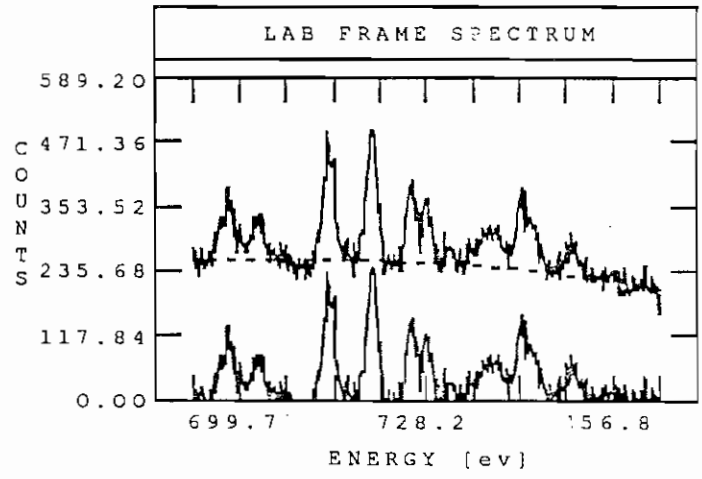
LAB FRAME SPECTRUM
589.20
471.36
353.52
235.68
117.84
0.00
COUNTS
699.7
728.2
156.8
ENERGY [ev]

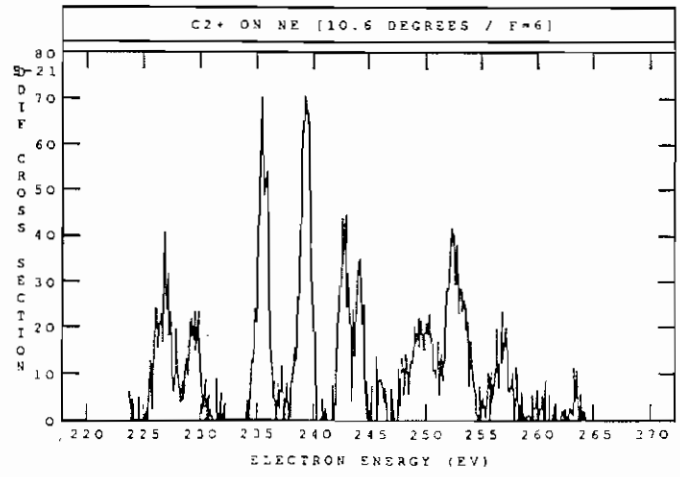
C2+ ON NE [10.6 DEGREES / F=6]
DIF CROSS SECTION
80
70
60
50
40
30
20
10
0
220
225
230
235
240
245
250
255
260
265
270
ELECTRON ENERGY (EV)

Figure 10

electrons[49] which are ionized from either the projectile or the target atom during the collision. Background subtraction was accomplished in Speakeasy by generating a continuous fit to background points lying between Auger lines. This is illustrated in the middle spectrum in figure 10 which shows the raw spectrum and background fit (dashed line) as well as the raw spectrum after background subtraction.

The bottom spectrum in figure 10 shows the data after analysis. The primary objectives of data analysis can be divided into three categories. First, electron counts are normalized to target density, detector solid angle and the number of ions passing through the HRPES viewing region. After normalization, the electron intensity is given as a doubly differential production cross section. The method used to normalize experimental yields into differential production cross sections will be described in detail in section 3.2. Second, the elements in the first row (ie. the channel numbers) of the raw array were transformed into absolute kinetic energy using predetermined calibration intercept and slope values. In order to find the calibration constants, hot wire tests were performed several times during each run period (see page 21). Channel numbers were then calibrated into absolute energy units using a linear equation which will be discussed in section 3.1 (see page 42). Finally, since Auger electrons were emitted by rapidly moving carbon ions (~$1x10^6$ m/s), an analysis of the collision kinematics (see section 3.4 and reference) was used to generate laboratory - projectile frame electron energy and intensity transformation equations. The transformation equations are derived and discussed in section 3.4 .

3.1 Lab Frame Electron Energy Calibration

Position encoding of charge pulses deposited on a resistive anode has been described by several authors[50,51,52,53]. Usually, charge division or rise time encoding techniques are used. The resistive anode element is designed to have a constant resistivity per unit length. Typical guarantees of resistance linearity vs position quote a maximum error of 2%. Charge pulse heights are related to position by:

$$(3.1)\quad \frac{Q_B}{Q} = \frac{R_A}{R} = \frac{X}{L} \qquad \text{and} \qquad \frac{Q_A}{Q} = \frac{R_B}{R} = 1-\frac{X}{L}$$

where X is the position at which the charge pulse was deposited relative to the Q_A preamplifier, L is the length and R is the resistance of the RAE between the Q_A and Q_B preamplifier charge sinks.

Although the charge division method was used in the early stage of this work, the rise time technique gave better results with less signal processing hardware, and no arithmetic processing software. This technique has been described by Borkowski[54], and analyzed by Matheison[55]. The timing signals are derived from the amplified Q_A and Q_B pulses such that a fast NIM signal is generated when the amplified pulse reaches some fraction of its peak voltage. The time delay between the Q_A and Q_B NIM signals can then be converted to a voltage using a Time to Amplitude Converter (TAC). The TAC performs a linear conversion of Q_A - Q_B delay time (the 0-2 μsec scale was used) into TAC output voltage (0 - 8 V scale). Obviously, in order to derive or at some fraction of the total rise time. In our case, however, the timing signals were derived from the bipolar output of a spectroscopy amplifier. A zero level crossing detection circuit[56] produced a NIM signal when the bipolar pulse as an input to a zero level crossing detector.

Measurements of the time between pulses were performed by a time to amplitude converter whose output voltage was digitized by an analog to digital converter. Since pulse propagation time across the RAE is fixed by capacitive coupling, the TAC voltages can be related to detection position and in turn to electron energy. The propagation time for the 50 mm HRPES RAE was 1.85 μs. This was determined by measuring the time between QA and QB pulses with a focused beam of electrons on an extreme edge of the detector. The plate propagation velocity was $\frac{50\text{mm}}{1.85\ \mu\text{s}} = 2.7 \times 10^4$ m/s.

In order to determine the slope and intercept for the linear equation relating spectrum channel number to electron kinetic energy in the analyzer, hot wire spectra were measured at the beginning and end of each run period. 10 to 15 electron energies were chosen so that

the electron peaks were evenly spaced over the MCP and not overlapping. The various peaks were accumulated for equal periods of time so that electron detection efficiency could also be checked.

Calibration spectra were then read into Speakeasy where the actual determination of the energy slope (M_E) and intercept (B_E) was accomplished. The centroid channel numbers for each energy was determined by a Gaussian fit and the ratio of electron energy (V_e) to analyzer plate voltage (V_P) was entered for each peak. A Speakeasy polynomial fitting routine was then used to find M_E and B_E. These values were later used in energy calibration formula:

(3.2) $E = (M_E N + B_E) V_P + V_D$

where E is the lab frame energy of the detected electron, N is the spectrum channel number, and V_D is the deceleration voltage applied to Auger electrons before entering the analyzer.

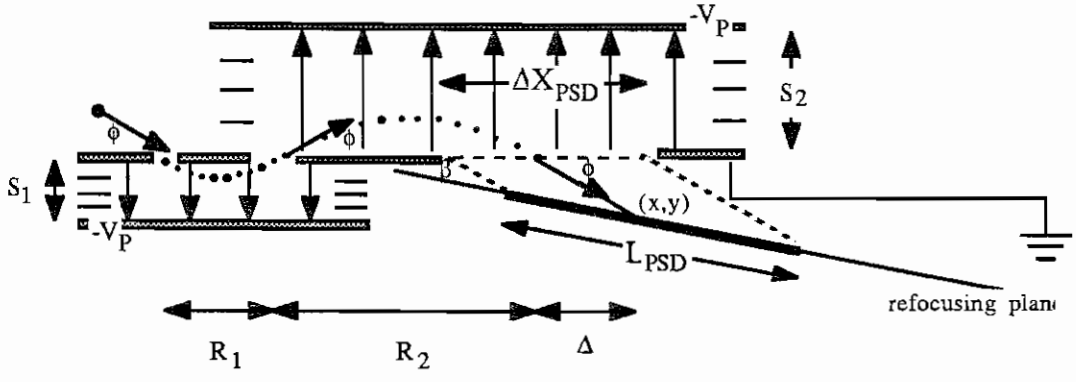

Figure 11 Electron trajectories in the HRPES spectrometer. The slope and intercept used in energy calibration depend on the relative position and orientation of the detector (PSD) and exit window.

Complications of the calibration procedure for projectile Auger emission arise when the lab frame observation angle was significantly different than 9.6°. Near 9.6°, the detector is placed at position giving second order focusing in the dispersion direction. However, the

detector was re-positioned and re-oriented for larger observation angles in order to maximize the focusing properties of the analyzer. This involved changing both the detector distance and angle with respect to the exit window and also influenced the position - kinetic energy relationship. The problem is illustrated in figure 13. Electrons exiting the spectrometer travel in straight line trajectories making an angle of 30° to the exit window. Re-positioning resulted in a shift of the entire spectrum since the translation axis slightly out of alignment with this direction, and re-orientation (changing the angle β) resulted in a stretching or compression of the spectrum.

3.2 Normalization of Auger Yields (Lab Frame Production Cross Section)

The total production cross section (σ) is related to the number of Auger decays (N_A) through the equation:

(3.3) $N_A = N_I (t\,\sigma)$

where N_I is the number of incident ions, and t is the number of target atoms found in a plane having unit area and oriented perpendicular to the ion beam axis. The cross section can be thought of as an effective area for the production of an Auger electron. Assuming that the areal density, (t) in equation (3.3), is uniform and constant in time, the term $(t\,\sigma)$ gives the total number of target atoms expected to pass within an area σ centered about the ion nucleus. The total number of decays is then the product of $(t\,\sigma)$ and the number of incident ions (N_I).

The intensity of spectra measured by the HRPES does not, however, represent a total lab frame production cross section. The spectrum shown in figure 10 was measured with the spectrometer oriented at 10.6° with respect to the axis defined by the ion beam. As a result, only electrons emitted within the small element of solid angle ($\Delta\Omega$) defined by the spectrometer entrance slits, and centered about 10.6° were recorded. In addition, even though the spectrum appears continuous, it is actually composed of 512 discrete bins as explained previously. The number of counts recorded in each bin represents the total

number of electrons transmitted through the HRPES within some range of energies (ΔE). Consequently, the intensities must be expressed as a doubly differential cross section $(\frac{d^2\sigma}{dE\ d\Omega})$ having units of $\frac{cm^2}{eV\ Sr}$. If $N_A(\Delta E,\Delta\Omega)$ denotes the number of Auger electrons emitted by projectile ions having energy within a range ΔE, and emitted into an element of solid angle $\Delta\Omega$, then the doubly differential cross section may be defined as follows:

$$(3.4)\quad N_A(\Delta E,\Delta\Omega) = N_I\, t\, \sigma(\Delta E,\Delta\Omega) = N_I\, t\, \frac{d^2\sigma}{d\Omega dE} d\Omega\, dE$$

In transforming measured Auger electron yields into absolute production cross sections, it is necessary to know the number of projectile ions and the number of target atoms responsible for the observed yield.

Following transit through the target cell, the ion beam was collected in an electrically suppressed Faraday cup and monitored by a commercially available current integration device (BCI meter). The BCI meter generated logic pulses that were counted by a count down preset scalar which halted data taking when the preset value was reached. As discussed in section 2.3, each BCI pulse represented $\frac{1}{100}$ of an amount of charge equal to the full scale current setting times 1 second. Great care was taken in zeroing the meter and balancing the meter amplifier at the start of each run period and whenever the meter scale was changed. Also, a careful written record was kept of the number of logic pulses (BCI) and the current scale setting (S) of the meter. Assuming that the ions did not change charge within the target cell, the number of ions traversing the target cell during each run could be estimated:

$$(3.5)\quad N_I = \frac{Q_{Faraday\ Cup}}{Q_{Ion}} = \frac{\left(\left[\frac{BCI}{100}\right]\right)\left(S \times 10^{-9}\right)}{Q\,(1.6 \times 10^{-19})} = 6.25 \times 10^7 \left(\frac{BCI \times S}{Q}\right)$$

N_I is the desired number of incident ions, Q is the charge of an ion entering the Faraday cup in atomic units, S is the BCI scale in nanoAmperes and 1.6×10^{-19} is the charge of an atomic unit in Coulombs.

Although the assumption that ions do not change charge in transit through the gas cell seems to be in conflict with the results presented in the final chapter that interpret the Auger spectra in terms of single electron capture to incident C^{4+} ions, ions which capture an electron and Auger decay enter the Faraday cup with no net charge change since an electron is lost in the Auger decay. However electron capture to $1s^2\ ^1S$ ions do not decay and represent the strongest contribution (~1% error) to the normalization error. Other transitions in the measured K-Auger spectra showed that K-L shell excitation of a single electron occurred with much less frequency than electron capture. Excitation does not change the charge of an incident ion. Another collision process which would contribute to normalization error would be that of electron ionization from either the L-shell of metastable $1s2s\ ^3S$ incident ions, or the K-shell of either $1s2s\ ^3S$ or $1s^2\ ^1S$ incident ions. Since ionization of a Helium-like system yields configurations which do not decay by Auger emission, the strength of this process as compared to electron capture could not be measured. However, the collision velocities involved in this experiment were far above L-shell velocities so L-shell ionization should be unlikely, and measurement of K-shell ionization of C^{2+} ions[57] shows that K-shell ionization less likely than electron capture by $1x10^3$.

The number of target atoms per unit area within the gas cell (t) is also needed in normalizing electron yields. The target density, t, can be expressed as the product of the number of target atoms in a unit volume and the spectrometer viewing length (ℓ). Using the ideal gas law, the number density of target atoms becomes $\frac{\text{Number of Atoms}}{\text{Volume}} = \frac{P}{k\ T}$ the following expression for t is found:

$$(3.6)\quad t = \frac{(P)\,\ell}{k\ \ (T)} = \frac{(P)\,\ell}{(1.38 \times 10^{-23})\ (300)} = (2.416 \times 10^{20})\ P\ \ell\ \frac{\text{atoms}}{m^3\ (Pa)}$$

where 1.38×10^{-23} is the numerical value of the Boltzmann constant (k) and room temperature (300 °K) was assumed for T. Since pressure and target length were measured in milliTorr and millimeters respectively, multiplication by the appropriate conversion

factors gives:

(3.7) $t = (133.32)\,(.001)\,(2.41 \times 10^{20})\,P\,\ell = (3.22 \times 10^{19})\,P\,\ell \ \left(\frac{\text{atoms}}{m^2}\right)$

For a number of reasons, not all Auger electrons emitted in the decay of excited ions are detected by the spectrometer. As a result, an overall efficiency factor must be included in normalizing measured Auger yields into absolute cross sections. The experimental efficiency is discussed in section 3.3, and is defined as the fraction of the number of electrons detected (η_A) to the total number of electrons from all decays (N_A):

(3.8) $\varepsilon = \frac{\eta_A}{N_A}$ or $N_A = \frac{\eta_A}{\varepsilon}$

Finally, the relationship between the number of Auger electrons detected and the cross section is:

(3.9) $$\sigma = (4.97 \times 10^{-21}) \left(\frac{\eta_A\, Q}{P\ \ell\ S\ \ BCI\ \ \varepsilon} \right) cm^2$$

where:

ℓ = target viewing length measured in millimeters

P = Target gas pressure measured in milliTorr

S = BCI current integration scale in nanoAmperes

Q = Estimated average ion charge in atomic units

3.3 Auger Electron Detection Efficiencies

A number of factors such as the collision geometry, the efficiency of the position sensitive MCP detector, and the focusing of the radial deceleration field contribute to the overall efficiency. Each is discussed briefly below, and analyzed in detail in sections 3.3.1, 3.3.3, and 3.3.4.

The beam - target - analyzer geometry was a major factor in fixing the value of the experimental efficiency. The efficiency associated with the collision geometry is analyzed in section 3.3.1 under the assumptions of straight line electron trajectories and isotropic electron emission in the ion rest frame. The value of the spectrometer entrance slit area

(ΔA) and polar acceptance angle (α) were critical in determining the "geometrical efficiency". These values were measured by normalizing measured target Auger yields to a published K Auger production cross section. Details are given in section 3.3.2.

Since the target viewing length (ℓ) and the geometrical efficiency both depend on the value of the polar observation angle (θ), a formula for the product ($\ell\mathcal{E}$) is derived in section 3.3.1. Equation 3.16 gives a simple expression for ($\ell\mathcal{E}$) in terms of θ, α and ΔA. The Auger spectra presented in chapter 4 of this work were measured with the HRPES entrance slits oriented at 9.6° and 10.2° with respect to the ion beam. At these angles, the HRPES was able to view only a small length (~ 6 mm) of the ion beam within the target cell.

The HRPES micro-channel plate (MCP) detector efficiency was measured during hot wire tests. The electron detection efficiency depended on position along the MCP detector and was found to decrease linearly with distance from the low energy end to the high energy end of the detector. Efficiency at the high energy end was ~20% less than the efficiency at the low energy end. This effect is associated with the relative position and orientation of the HRPES exit window and MCP detector and is discussed in section 3.3.3.

When electron deceleration is used, equation 3.16 is no longer valid. Straight line electron trajectories were used in deriving the formula relating target viewing length to polar observation angle. Deceleration, however, caused electron paths to curve in the radial electric field between the concentric inner and outer gas cells. In section 3.3.4, it is shown that the radial field causes a reduction in the effective target viewing length. An exact expression for the deceleration efficiency depends on several experimental parameters including: deceleration bias; ion beam energy; and Auger transition energy. An exact treatment would require that separate efficiencies be calculated for each Auger transition as the effective target viewing length varies somewhat for the different transition energies. In practice, the decelerated spectra were corrected using an average efficiency for the entire

spectrum (see equation 4.1).

3.3.1 Target Cell and Collision Geometry

Figure 12 shows a cross section of the differentially pumped target cell and the ion beam - spectrometer orientation. The radial field (E_r) between the inner and outer cylinders was present only during runs in which electron deceleration was used. The following analysis, however, applies only to undecelerated data in which electrons follow straight line trajectories. The effect of deceleration is considered in section 3.3.4.

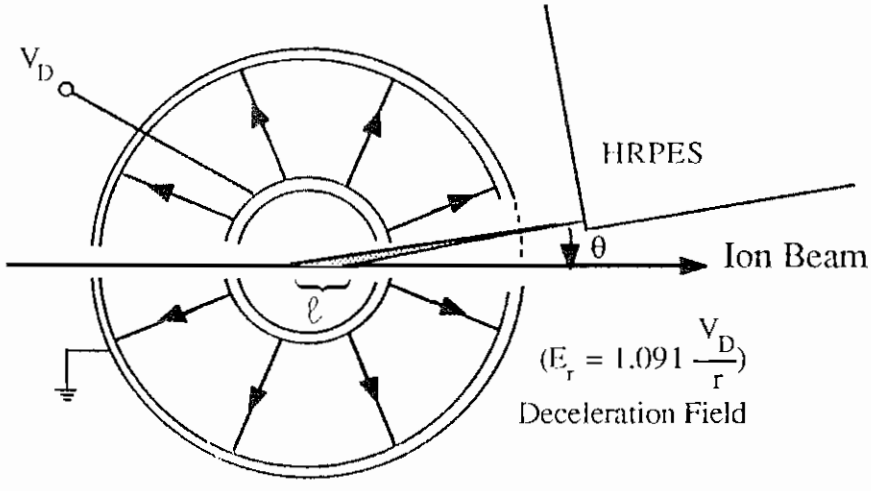

Figure 12 A cross section of the collision cell showing the HRPES viewing region (shaded region). The inner cylinder contains target gas at constant pressure. The target viewing length, ℓ, is the length of the ion beam which borders the shaded region.

The excitation of atomic energy levels of projectiles can occur as the beam passes through the target gas contained in the inner cylindrical cell. The lines at each edge of the shaded region in figure 12 represent the extreme trajectories for electrons able to be transmitted through the HRPES. Auger electrons emitted in the decay of excited ions enter the spectrometer only if the excited ion: 1) decays within the target viewing length (the

portion of the ion beam that borders the shaded region), and 2) emits the Auger electron such that it will pass through the HRPES entrance slits. The second condition is satisfied if the electron's trajectory remains within the shaded viewing region in figure 12.

The total viewing length (ℓ) is the sum of X_1 and X_2 as illustrated in figure 13. The target cell geometry can be used to obtain an expression for these quantities in terms of the polar observation angle (θ) and acceptance angle (α):

(3.10) $$X_1 = \frac{D \sin \alpha}{\sin \gamma_1} \quad \text{with} \quad \gamma_1 = \theta - \alpha$$

and $$X_2 = \frac{D \sin \alpha}{\sin \gamma_2} \quad \text{with} \quad \gamma_2 = \theta + \alpha$$

(3.11) $$\ell = X_1 + X_2 = (D \sin \alpha) \left[\frac{1}{\sin \gamma_1} + \frac{1}{\sin \gamma_2} \right]$$

where D = 3.31 cm = 1.300 in, and $\alpha = 0.664°$ ($\theta \leq 12°$), or $0.802°$ ($\theta > 12°$).

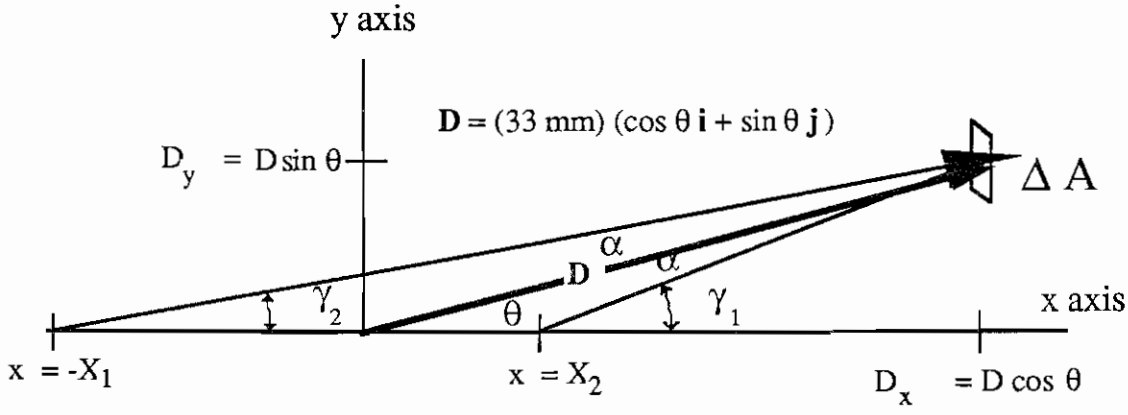

Figure 13 Diagram showing the orientation of the target viewing length along the x axis ($X_2 > x > -X_1$), and the area defined by the spectrometer entrance slits (ΔA).

Substituting for D and α gives:

(3.12) $$\ell = (0.462 \text{ mm}) \left[\frac{1}{\sin(\theta - 0.802°)} + \frac{1}{\sin(\theta + 0.802°)} \right] \quad \text{for } \theta < 12°$$

$$\text{or } \ell = (0.383 \text{ mm}) \left[\frac{1}{\sin(\theta - 0.664^\circ)} + \frac{1}{\sin(\theta + 0.664^\circ)} \right] \quad \text{for } \theta = 20,30,40,50^\circ$$

Assuming that Auger electron emission is equally probable in all directions (isotropic emission), the probability that an electron pass through the HRPES entrance slits is equal to the fractional solid angle subtended by the entrance slit area at the point of emission. At any point along the viewing length ℓ, the solid angle for a point source (Ω) is given by the scalar product:

(3.13) $$\Omega(x) = \frac{\Delta \mathbf{A} \cdot \mathbf{r}}{r^3}$$

$\mathbf{r}$ = the vector from the point at which the Auger electron is emitted to the center of the area ΔA defined by the entrance slits.

$\Delta \mathbf{A} = \Delta A \, \mathbf{D}/D$ where ΔA is the magnitude of the slit area in m^2, and $\mathbf{D}$ is a vector having magnitude D = 1.300 in., and directed from the geometrical center of the target cell to the spectrometer slits (see figure 13).

The product of the effective solid angle and the viewing length can be calculated:

(3.14) $$\mathscr{E}\ell = \frac{\Omega_{AV}}{4\pi} \ell = \frac{1}{4\pi} \int_{-X_1}^{X_2} \Omega(x) \, dx = \frac{1}{4\pi} \int_{-X_1}^{X_2} \frac{\Delta A}{r^3 D} (\mathbf{D} \cdot \mathbf{r}) \, dx$$

$$= \frac{\Delta A}{4\pi D} \int_{-X_1}^{X_2} \frac{D^2 - x D_X}{[D^2 + x^2 - 2 D_x x]^{3/2}} \, dx$$

$$= \frac{\Delta A}{4\pi D} \left(\frac{X_1}{\sqrt{X_1^2 + D^2 - 2 X_1 D_x}} + \frac{X_2}{\sqrt{X_2^2 + D^2 - 2 X_2 D_x}} \right)$$

where the following substitutions have been made:

(3.15) $$\mathbf{r} = (D_x - x)\mathbf{i} + D_y \mathbf{j}$$

$$r = [D^2 - 2D_x x + x^2]^{1/2}$$

$$D_X = D \cos \theta$$

3.3.2 Normalization Using Target K-Auger Yields

Before using equation 3.15 to determine the geometrical efficiency, the area (ΔA), the acceptance angle (α), and the distance (D) from target cell to the HRPES entrance slits had to be measured. D was measured with a micrometer gauge and found to be 1.300 inches (33 millimeters). Due to the possibility of electron shadowing by internal spectrometer components, a simple direct measurement for α and ΔA was not possible. Also, the entrance slits were extremely narrow and difficult to measure.

Normalizing measured Auger electron yields to a known cross section was thought to be a more reliable method. Protons having an energy of 3 MeV were obtained using the Dennis II plasma source and the FN tandem Van de Graaf and made to collide with Ne gas atoms. In the collision process, a K-shell electron is ionized from some of the Neon target atoms. Since the flurescence yield for Neon[58] is nearly 0, each ionization event produces an Auger electron. In the early 1970s, inner shell ionization of low Z target atoms by protons was studied by several authors. In this section we use the results of one such study[59] along with equations 3.9 and 3.14 in determining the values of α and ΔA.

Figure 14 shows two spectra taken with the HRPES at observation angles of 9.6° and 40° respectively. The required quantities for normalizing the yield as well as the total number of detected K-Auger electrons (net area) are also shown.

To obtain the entrance slit area, the 40° yield is first normalized using equation 3.9:

(3.16) $$\sigma = (4.97 \times 10^{-21}) \left(\frac{(3489)\ (1)}{(20)\ \ (600)\ \ (50000)\ \ \ell_{40^\circ}\, \varepsilon_{40^\circ}} \right) \text{cm}^2$$

where: $Q = 1$, $\eta_A = 3489$, $P = 20$ mT, $S = 600$ nA, and BCI = 50000

Using the cross section measured by McKnight ($\sigma_{\text{McKnight}} = 1.29 \times 10^{-19}$ cm^2) and solving for $\ell\, \varepsilon$ gives:

(3.17) $$(\ell\, \varepsilon)_{40^\circ} = \frac{2.89 \times 10^{-26} \text{cm}^2}{1.29 \times 10^{-19}\ \text{cm}^2} = 2.24 \times 10^{-7}$$

At 40°, the HRPES acceptance angle is limited by the .010 inch viewing slot in the inner gas cell ($\alpha_{40^\circ} = .0664^\circ$), and equation 3.14 can be used find a second expression for

Figure 14 Neon K-Auger spectra used to measure the value of the HRPES polar acceptance angle and entrance slit area. The target Auger decays result from inner shell ionization of electrons following bombardment by 3 MeV protons. The top spectrum was taken with the HRPES polar observation angle set at 9.6° with respect to the ion beam. At 9.6°, the HRPES acceptance angle was unrestricted. The bottom spectrum was taken with the HRPES polar observation angle set at 40° with respect to the ion beam. At 40°, the HRPES acceptance angle was limited to 0.664° by a viewing slot in the inner target cell. The total number of Auger electron counts in the region between the cursors is given by the value of the "net area".

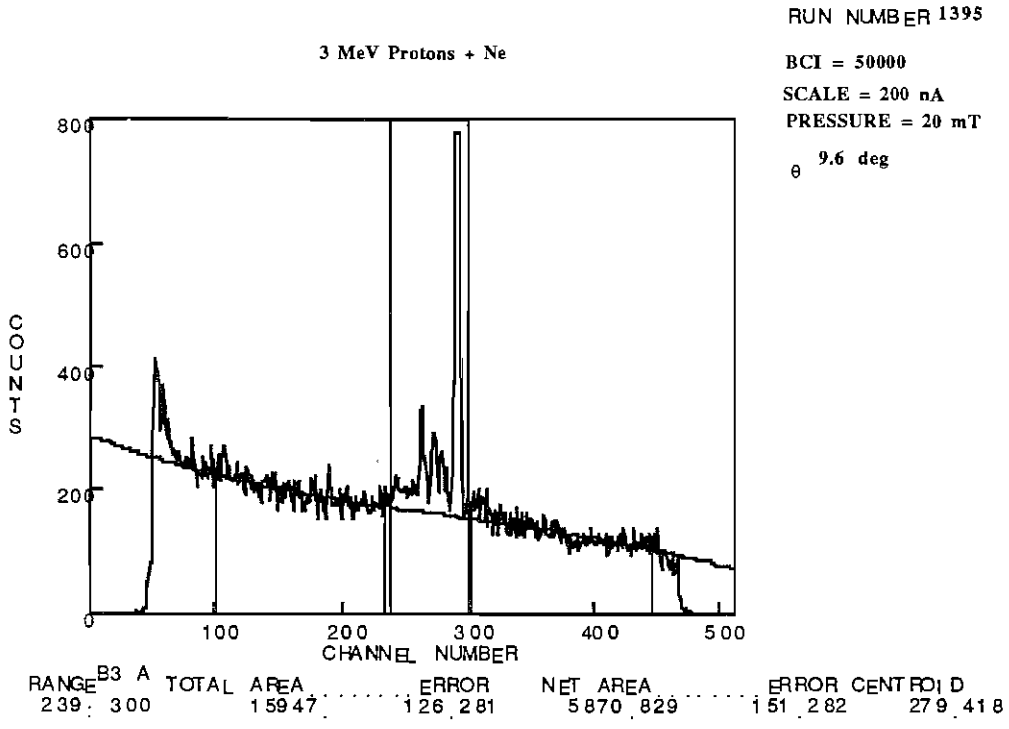
3 MeV Protons + Ne
RUN NUMBER 1395
BCI = 50000
SCALE = 200 nA
PRESSURE = 20 mT
θ 9.6 deg
COUNTS
CHANNEL NUMBER
RANGE B3 A TOTAL AREA ERROR NET AREA ERROR CENTROID
239 : 300 15947 126.281 5870.829 151.282 279.418

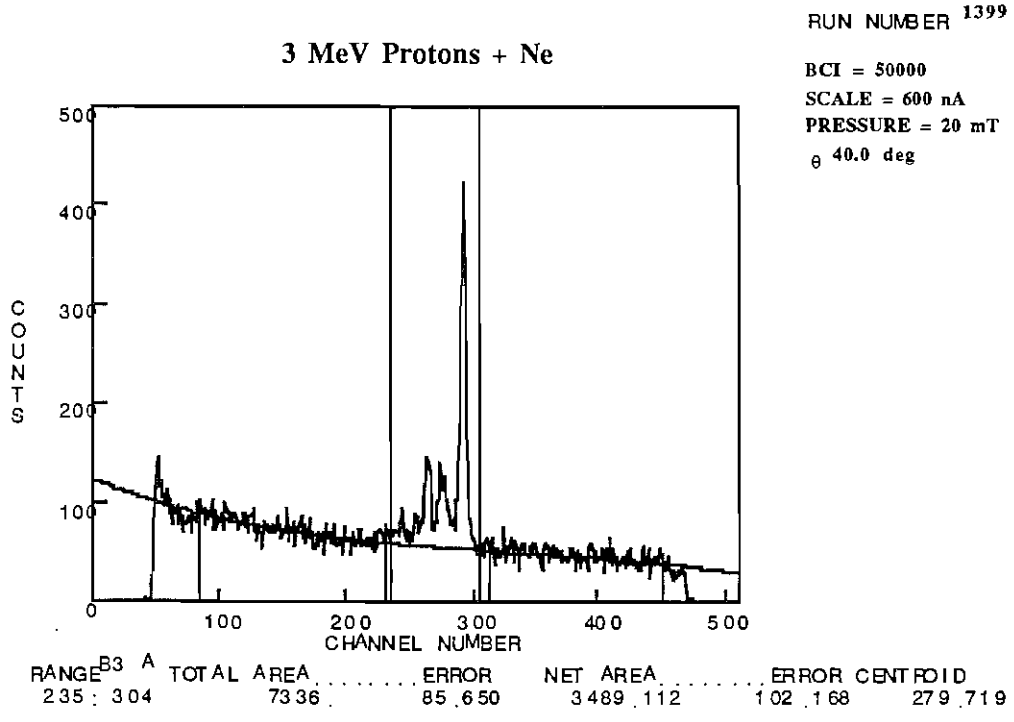
3 MeV Protons + Ne
RUN NUMBER 1399
BCI = 50000
SCALE = 600 nA
PRESSURE = 20 mT
θ 40.0 deg
COUNTS
CHANNEL NUMBER
RANGE B3 A TOTAL AREA ERROR NET AREA ERROR CENTROID
235 : 304 7336 85.650 3489.112 102.168 279.719

Figure 14

the product $\ell\,\varepsilon$:

(3.18) $(\ell\,\varepsilon)_{40^\circ} = 2.24 \times 10^{-7}$

$$= \frac{\Delta A}{(33)}\left(\frac{0.5996}{\sqrt{(0.6)^2 + (33)^2 - 2(0.6)(25.3)}} + \frac{(0.5834)}{\sqrt{(0.58)^2 + (33)^2 - 2(0.58)(25.3)}}\right)$$

where: $$X_1 = (33\text{ mm})\frac{\sin(0.664^\circ)}{\sin(40.000^\circ - 0.664^\circ)} = 0.5996\text{ mm}$$

$$X_2 = (33\text{ mm})\frac{\sin(0.664^\circ)}{\sin(40.000^\circ + 0.664^\circ)} = 0.5834\text{ mm}$$

$$D_X = (33\text{ mm})\cos(40^\circ) = 25.28\text{ mm}$$

Solving 3.18 for ΔA gives:

(3.19) $\Delta A = 0.00254\text{ mm}^2$

The next task is to find the unobstructed acceptance angle. At 9.6°, the inner target cell does not limit the acceptance angle. The first step is to use equation 3.9 to calculate the product $(\ell\,\varepsilon)_{9.6^\circ}$:

(3.20) $$\sigma = (4.97 \times 10^{-21})\left(\frac{(5871)\,(1)}{(20)\;\;(200)\;\;(50000)\;\;\ell_{9.6^\circ}\,\varepsilon_{9.6^\circ}}\right)\text{cm}^2$$

$$= (1.459 \times 10^{-25}\text{ cm}^2)\;\frac{1}{\ell_{9.6^\circ}\,\varepsilon_{9.6^\circ}}$$

and we find that:

(3.21) $$(\ell\,\varepsilon)_{9.6^\circ} = \frac{1.459 \times 10^{-25}\text{ cm}^2}{1.29 \times 10^{-19}\text{ cm}^2} = 1.131 \times 10^{-6}$$

If equation 3.14 is used, a second expression for $(\ell\varepsilon)_{9.6^\circ}$ can be used to find an equation for α_{HRPES}:

(3.22) $(\ell\,\varepsilon)_{9.6^\circ} = 1.131 \times 10^{-6}$

$$= \frac{.00254}{4\pi\,(33)}\left(\frac{X_1}{\sqrt{X_1^2 + D^2 - 2\,X_1\,D_x}} + \frac{X_2}{\sqrt{X_2^2 + D^2 - 2\,X_2\,D_x}}\right)$$

where: $$X_1 = (33)\frac{\sin(\alpha_{HRPES})}{\sin(9.6^\circ - \alpha_{HRPES})}$$

$$X_2 = (33\text{ mm})\frac{\sin(\alpha_{HRPES})}{\sin(9.6^\circ + \alpha_{HRPES})} = 0.5834\text{ mm}$$

$$D_X = (33\text{ mm})\cos(9.6^\circ) = 25.28\text{ mm}$$

Using the approximation that $\cos(9.6^\circ) \sim 1$, equation 3.22 becomes:

$$(3.23)\quad \frac{\dfrac{\sin(\alpha_{HRPES})}{\sin(9.6^\circ - \alpha_{HRPES})}}{1 - \dfrac{\sin(\alpha_{HRPES})}{\sin(9.6^\circ - \alpha_{HRPES})}} + \frac{\dfrac{\sin(\alpha_{HRPES})}{\sin(9.6^\circ + \alpha_{HRPES})}}{1 - \dfrac{\sin(\alpha_{HRPES})}{\sin(9.6^\circ + \alpha_{HRPES})}} = 0.185$$

A value of $\alpha_{HRPES} = 0.81^\circ$ was found to satisfy equation 3.23.

3.3.3 Micro-Channel Plate Detector Efficiency

The 50 mm x 8 mm detector was positioned in the calculated refocusing plane (see section 2.2.1) defined by a translation distance (R_t) and angle (R_θ) with respect to the exit window. The efficiency arises from the fact that the divergence of some electrons leaving the spectrometer exit window may be large enough that they are unable to hit the detector. The situation is pictured below in figure 15.

Electrons leave the spectrometer at various positions along the length of the exit window (the left - right slot in figure 15) and travel in straight line trajectories until reaching the detector. After leaving the spectrometer the electron trajectories are parallel lines oriented at 30° to the exit window plane (see top view shown in figure 16).

As can be seen in figure 16, the angle ($\Delta\phi$) subtended by the 8 mm tall detector depends on the translational distance R_t and orientation angle R_θ. In the home position $R_\theta = 10.9^\circ$, the distance between the window and the MCP detector increases from the low to high energy ends of the exit window. This is shown in figure 16 where equations 2.8 has been used to obtain $R_t = 24.2$ mm.

Since the drift distance depends on electron energy, and since the MCP height is 4 mm,

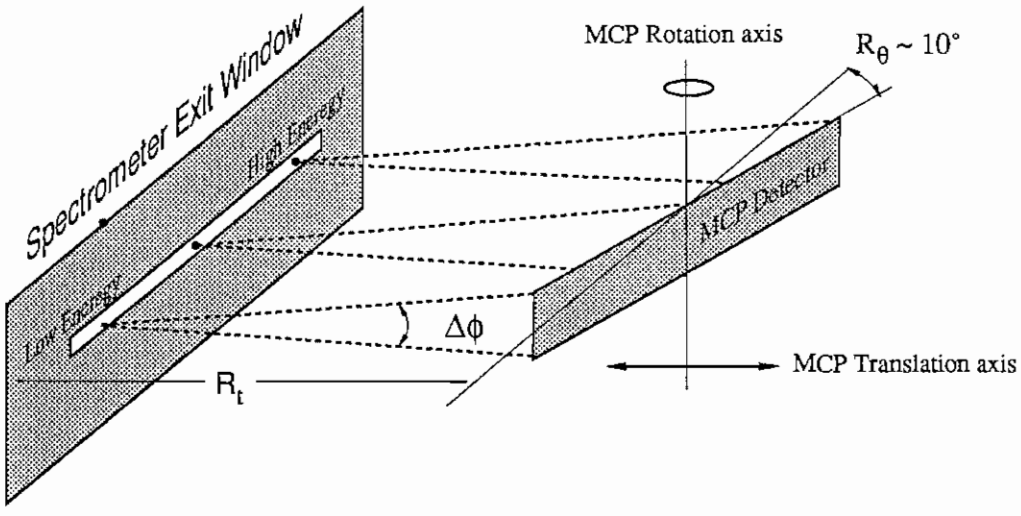

Figure 15 Diagram showing the HRPES exit window - MCP detector orientation. The dashed lines represent extreme rays for electrons trajectories detected experimentally. The angle $\Delta\phi$ is a measure of the detection efficiency and clearly depends on the translational (R_t) and rotational (R_θ) refocusing co-ordinates as well as the electron energy.

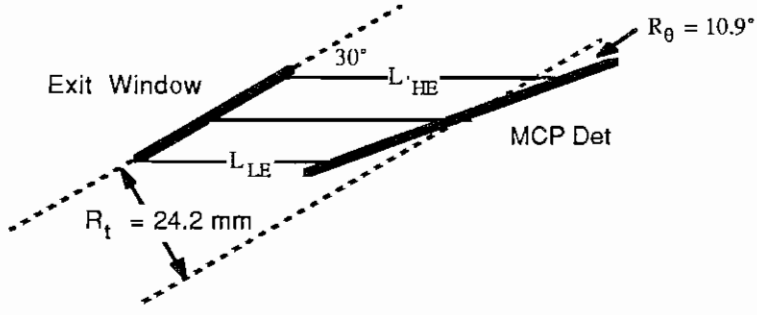

Figure 16 Illustration showing the variation in drift distance with electrons energy with the detector in the "home position". Electrons travel in straight lines making an angle of 30° with the exit window, and 40.9° with the detector.

$\Delta\phi$ can be evaluated:

(3.24) $$\Delta\phi = 2\ \mathrm{Tan}^{-1}\left(\frac{4}{L(E)}\right)$$

The detector subtends a larger angle for low energy electrons. No corrections have been made in the analysis for this effect. The spectra appearing in chapter 4 are most accurate near the center of the spectrum. Using simple trigonometry, and the law of sines in calculating L_{HE} and L_{LE}, the maximum error can easily be calculated:

(3.25) $$\frac{\Delta\phi_{HE}}{\Delta\phi_{LE}} = \frac{4.25^\circ}{5.34^\circ} = 79.6\%$$

where $$L_{LE} = \frac{24.2}{\sin(30^\circ)} - 24.2\frac{\sin(10.9^\circ)}{\sin(60^\circ)} = 42.3$$

$$L_{HE} = \frac{24.2}{\sin(30^\circ)} + 24.2\frac{\sin(10.9^\circ)}{\sin(60^\circ)} = 53.8$$

$$\Delta\phi_{HE} = 2\ \mathrm{Tan}^{-1}\left(\frac{4}{53.8}\right) = 4.25^\circ$$

$$\Delta\phi_{LE} = 2\ \mathrm{Tan}^{-1}\left(\frac{4}{42.3}\right) = 5.34^\circ$$

This result indicates that the highest energy transitions appear with only 80% of the intensity of the lowest energy transitions.

3.3.4 Deceleration

As described in section 2.2.2, the target cell is composed of concentric, electrically isolated cylinders, with the outer aluminum cylinder having a radius R_o = 1.250 in (3.175 x 10^{-2} m) and the inner cylinder having a radius R_i = 0.500 in (1.270 x 10^{-2} m). In order to enhance the experimental resolution, Auger electrons were decelerated in the region between the cylinders by applying a positive deceleration voltage V_D to the inner cylindrical cell while grounding the outer cell. The geometry is the same as that of a cylindrical capacitor and the electric field varies as $\frac{1}{r}$:

(3.26) $$E_r = \frac{V_D}{r\ \ln\left(\frac{R_o}{R_i}\right)}$$

The use of deceleration as a tool to improve energy resolution in an electron spectrometer has been exploited previously[60]. The resolution enhancement factor (f), or deceleration factor, was kept constant for Auger spectra taken at various collision energies.

The deceleration factor is given by the ratio of the electron energy before and after deceleration:

(3.27) $f = \text{Deceleration Factor} = \frac{E_{lab}}{E_{analyzer}}$

If E_{lab} and $E_{analyzer}$ are expressed in eV, the deceleration bias in Volts is given by:

(3.28) $$V_D = E_{lab} - E_{analyzer} = E_{lab}\left(\frac{f-1}{f}\right) = E_{analyzer}(f-1)$$

Along with improved resolution, deceleration introduces complications. First, electron trajectories are altered resulting in a decrease in the geometrical efficiency. Both the target viewing length and the average solid angle decrease in proportion to the deceleration factor. Secondly, in a single run, HRPES measures electrons over a range of energies. Since V_D was determined using E_{lab} for the central Auger energy, the deceleration factor was not exactly the same for all transitions in a spectrum. Consequently, both resolution and efficiency within a single spectrum vary with energy. The trend is such that low energy transition intensities are underestimated and high energy intensities are overestimated. The deceleration resolution, on the other hand, is greatest for the low energy transitions in a given spectrum.

The decrease in ℓ is caused by the fact that only the radial component of the electron's velocity upon entering the field is decelerated. The radial deceleration is given by:

(3.29) $$a_r = \left(\frac{-e}{m}\right) E_r = -\frac{e}{m}\left[\frac{V_D}{r \ln\left(\frac{R_o}{R_i}\right)}\right]$$

where e and m are the charge and mass of an electron and a_r points in the radial direction defined by a cylindrical coordinate system whose z-axis coincides with the symmetry axis of the cell.

The expression for $\Omega_{AV}\ell$ given in equation 3.14 was derived for straight line electron trajectories. When deceleration is used, electrons travel in straight lines until encountering the electric field. Because the acceleration is entirely in the radial direction, the electron's

angular momentum ($\mathcal{L}$) remains constant while the radial component of momentum decreases. The net result is that the extreme rays shown in figure 12 focus in front of the spectrometer.

In the field, electrons travel in complicated trajectories. The trajectories can, in principle, be found by solving the following orbital equation taken from the theory of central forces:

$$\theta(r) = \int [2m(E - U(r) - \frac{\mathcal{L}}{r^2}]^{-1/2} \left(\frac{\mathcal{L}}{r^2}\right) dr \tag{3.30}$$

where $$U(r) = \frac{V_D}{\ln(R_o/R_i)} \ln\left(\frac{r}{R_i}\right)$$

and $\mathcal{L}$ = angular momentum

3.4 Kinematic Transformations

That Auger electrons emitted by a moving ion are influenced by kinematic considerations was pointed out several decades ago by Rudd[61]. The kinematics of Auger decay by a rapidly moving ion has been studied more recently by Gordeev[62], Macek[63], Risley[64], and Stolterfoht[65]. The energy, energy width, and intensity of Auger lines are radically changed by the relative motion of the measuring device with respect to the emitter.

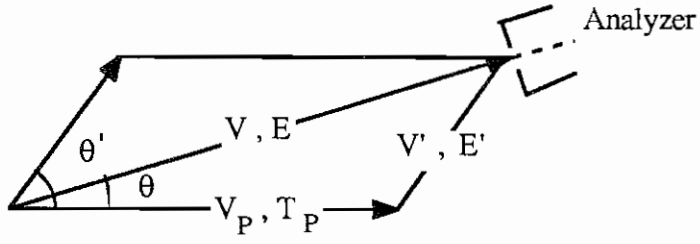

Figure 17 Diagram illustrating the relation between the vector velocity of an Auger electron as seen in the laboratory frame (V), the projectile rest frame (V'), and the projectile velocity (V_P).

Figure 17 shows an Auger electron being emitted by a projectile ion. The ion is moving with a velocity $v_P = \sqrt{\frac{2}{M_P} E_P}$, where M_P is the mass of the projectile and E_P is

the collision energy. The electron is emitted with a characteristic kinetic energy E' relative to the moving ion. E' is determined by the energy difference between the excited and final configurations associated with the Auger transition. The velocity of the electron relative to the projectile is which is $v' = \sqrt{\frac{2}{m}E'}$.

Since the velocity of an Auger electron entering the spectrometer (**v**) is the vector sum of $\mathbf{v_P}$ and **v'**, the kinetic energy of the electron and the spectrometer observation angle (θ) will differ from the emission energy (E') and angle (θ') in the ion rest frame. The emission angle and observation angles can be related if the velocities are known:

(3.31) $$\cos\theta' = \frac{v}{v'}\cos\theta - \frac{v_P}{v'}$$

or $$\cos\theta = \frac{v'}{v}\cos\theta' - \frac{v_P}{v}$$

Also, applying the law of cosines gives:

(3.32) $$v^2 = v'^2 + v_P^2 + 2v_P v'\cos\theta'$$

and $$v'^2 = v^2 + v_P^2 - 2v_P v\cos\theta$$

The energy transformations can be obtained by multiplying 3.31 by half the electron mass ($\frac{m}{2}$)

(3.33) $$E = E' + T_P + 2\sqrt{E'\,T_P}\ \cos\theta'$$

and $$E' = E + T_P - 2\sqrt{E\,T_P}\ \cos\theta'$$

Finally, the difference between the intensity of an Auger line detected in the lab frame and the emission intensity in the ion rest frame can be assigned to the difference in the entrance slit solid angle with respect to a stationary and moving source. The solid angle subtended by the spectrometer entrance slits for a stationary source ($d\Omega$) and a moving source ($d\Omega'$) are related by the kinematic transform for the polar angle, equation 3.30. As can be seen from figure 19,

Expressing the solid angle in polar coordinates, and using equation 3.31 for $\frac{d\cos\theta}{d\cos\theta'}$, the intensity transformation formula can be found:

(3.34) $$\frac{I_{lab}}{I_{ion}} = \frac{d\Omega}{d\Omega'} = \frac{d\cos\theta\, d\phi}{d\cos\theta'\, d\phi'} = \frac{d\cos\theta}{d\cos\theta'} = \frac{E}{E'}\sqrt{1 - \frac{T_P}{E'}\sin^2\theta}$$

4 RESULTS

Projectile K-Auger spectra were measured for C^{4+} ions incident on H_2, He, Ne and Ar gas targets. The spectra were studied as a function of collision energy. Spectra were measured between 4 and 8 MeV ($\frac{1}{3}$ to $\frac{2}{3}\frac{\text{MeV}}{\text{amu}}$) in 1 MeV intervals. Identification of lines in the Auger spectra are based on theoretical and semi-empirical calculations and are summarized in table 1. Transitions shown in table 1 are divided into five groups labeled A, B, C, D, and E in order of increasing energy.

The electronic configurations of excited ions within each group share certain similarities. These characteristics include the number of electrons in the excited ion's orbital cloud as well as similarities in the distribution of those electrons in the various ionic shells.

Most of the transitions observed in this work were the result of single electron capture by metastable 1s2s ^{3}S ions. The excited configuration of the group A transition contain 3 orbital electrons and occur when a single electron is captured into the $n = 2$ shell of a metastable ion. The group E transitions also involve three electron excited configurations, however, they are the result of single electron capture into $n \geq 3$ shells of metastables. Other production mechanisms, such as electron capture by $C^{4+}(1s^2\ ^1S)$ ions accompanied by an excitation of a 1s electron, are possible. However, such double processes are much less probable.

The group C and D transitions are known as hypersatellites. The group D transitions also involve 3 electron excited configurations while the group C excited configurations have 2 electrons. In both cases, however the inner K shell is bare so that all electrons occupy shells with $n \geq 2$. Group C configurations are formed from metastable ions through excitation of a single K shell electron into an L shell orbital. The D configurations arise from 1s2s 3S ions through a process involving both electron capture and K - L shell excitation.

Type B transitions involve double electron capture into the $n = 2$ shell of $1s2s\ ^3S$ ions. These were strongest for collisions involving neon and argon targets, but were weak compared to single electron capture transitions.

In the following figures, K-Auger spectra are organized according to increasing collision energy and deceleration factor. The cross sections are differential with respect to electron energy. All intensities and energies have been transformed into the projectile rest frame, as described in the previous chapter.

Although the decelerated spectra (f=6) are the most detailed and informative, the undecelerated spectra (f=1) are also included for several reasons. Since detector position efficiency and deceleration efficiency (see section 3.3.2) are difficult to calculate explicitly, the primary reason for recording the undecelerated spectra was to obtain a rough correction for the intensities of the decelerated spectra. This was accomplished by multiplying observed intensities for various deceleration factors and detector positions by the an average correction factor:

$$(4.1) \quad I = \frac{\int Y(f=1)\, dE}{\int Y(f=6)\, dE}\, I' \quad \text{deceleration efficiency correction}$$

$$I = \frac{\int Y(0,0)\, dE}{\int Y(R_t,R_\theta)\, dE}\, I' \quad \text{detector position efficiency correction}$$

where I is the corrected intensity, I' is the observed intensity, Y(f=1) is the observed yield without deceleration, Y(f=6) is the decelerated yield using, Y(0,0) is the measured yield with the detector in the "home position" and $Y(R_t,R_\theta)$ is the measured yield with the detector translated and rotated by a given number of steps.

Table 1 Compilation of calculated transition energies in eV for selected K-Auger transitions of Li-like, Be-like and He-like excited configurations. The branching ratios refer to the corresponding decay for ionic Neon. An asterisks indicates that the energy in question was obtained using a semi-empirical formula. The following references were used in compiling table 1.

a. R. Bruch, K.T. Chung, et al[66] c.K.T. Chung and B.L. Davis[67]

b. N. Stolterfoht (ref. 16) d. D. Schneider et al (refs. 19 and 20)

Table 1

	Excited-Final Configuration		Energy (eV)	Br. Ratio	Ref.
A	$1s2s^2\ ^2S$	$1s^2\ ^1S$	227.17	1	a
			227.5		b
	$1s2s2p\ ^4P$	$1s^2\ ^1S$	229.64	1	a
			229.9		b
	$1s(2s2p\ ^3P)\ ^2P$	$1s^2\ ^1S$	235.55	1	a
			235.9		b
	$1s(2s2p\ ^1P)\ ^2P$	$1s^2\ ^1S$	238.78	1	a
			239.3		b
	$1s2p^2\ ^2D$	$1s^2\ ^1S$	242.08	1	a
			242.3		b
B	$1s2s^22p\ ^3P$	$1s^22p\ ^2P$	235.9	.57	b
	$1s2s^22p\ ^1P$	$1s^22p\ ^2P$	238.5	1	b
			238.50		a
	$1s2s^22p\ ^3P$	$1s^22s\ ^2S$	243.6	.43	b
	$1s2s2p^2\ ^3P$	$1s^22p\ ^2P$	243.6	1	b
	$1s2s2p^2\ ^3D$	$1s^22p\ ^2P$	244.3	.12	b
	$1s2s2p^2\ ^1D$	$1s^22p\ ^2P$	248.3	.51	b
	$1s2s2p^2\ ^3P$	$1s^22p\ ^2P$	249.9	1	b
	$1s2s2p^2\ ^1P$	$1s^22p\ ^2P$	251.0	1	b
	$1s2s2p^2\ ^1S$	$1s^22p\ ^2P$	252.2	1	b
C	$2s2\ ^1S$	$1s\ ^2S$	264.34	1	b*
	$2s2p\ ^3P$	$1s\ ^2S$	265.80	1	b*
	$2p^2\ ^1D$	$1s\ ^2S$	272.50	1	b*
	$2s2p\ ^1P$	$1s\ ^2S$	273.64	1	b*
D	$2s^22p\ ^2P$	$1s2s\ ^1S$	275.8	-	c
	$2s2p^2\ ^2P$	$1s2s\ ^3S$	281.3	-	c
	$2s2p^2\ ^2D$	$1s2s\ ^3S$	282.45	-	c
	$2s2p^2\ ^2D$	$1s2s\ ^3P$	282.42	-	c
	$2s2p^2\ ^2D$	$1s2s\ ^1S$	287.87	-	c
E	$(1s2s\ ^3S)3s\ ^2S$	$1s^2\ ^1S$	269.6	-	d
	$(1s2s\ ^3S)3p\ ^2P$	$1s^2\ ^1S$	271.95	-	d
	$(1s2s\ ^3S)3d\ ^2D$	$1s^2\ ^1S$	274.3	-	d
	$(1s2s\ ^3S)4\ell$	$1s^2\ ^1S$	< 286	-	d
	$(1s2s\ ^3S)n\ell\ (n \geq 5)$	$1s^2\ ^1S$	< 299	-	d

Figure 18 Undecelerated projectile K-Auger spectra for 4MeV collisions of C^{4+} ions with molecular Hydrogen, Helium, Neon and Argon gas targets. The laboratory frame observation angle was 10.2°.

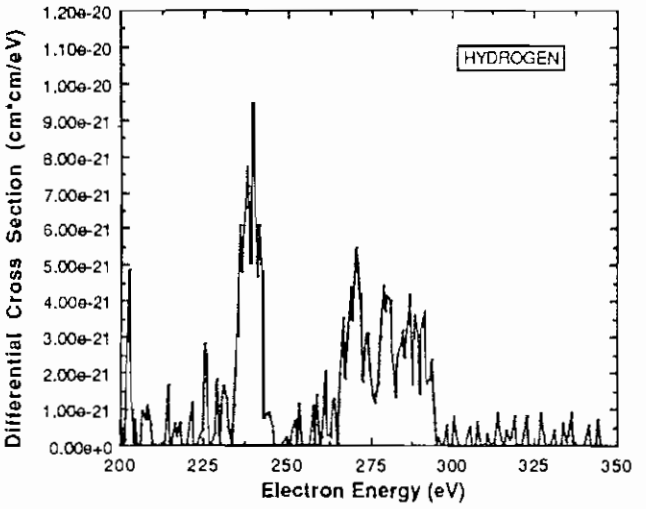
HYDROGEN
Differential Cross Section (cm*cm/eV)
1.20e-20
1.10e-20
1.00e-20
9.00e-21
8.00e-21
7.00e-21
6.00e-21
5.00e-21
4.00e-21
3.00e-21
2.00e-21
1.00e-21
0.00e+0
200 225 250 275 300 325 350
Electron Energy (eV)

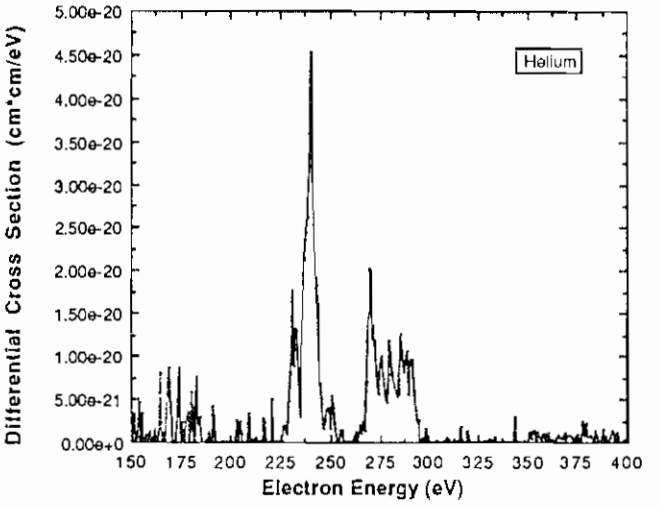
Helium
Differential Cross Section (cm*cm/eV)
5.00e-20
4.50e-20
4.00e-20
3.50e-20
3.00e-20
2.50e-20
2.00e-20
1.50e-20
1.00e-20
5.00e-21
0.00e+0
150 175 200 225 250 275 300 325 350 375 400
Electron Energy (eV)

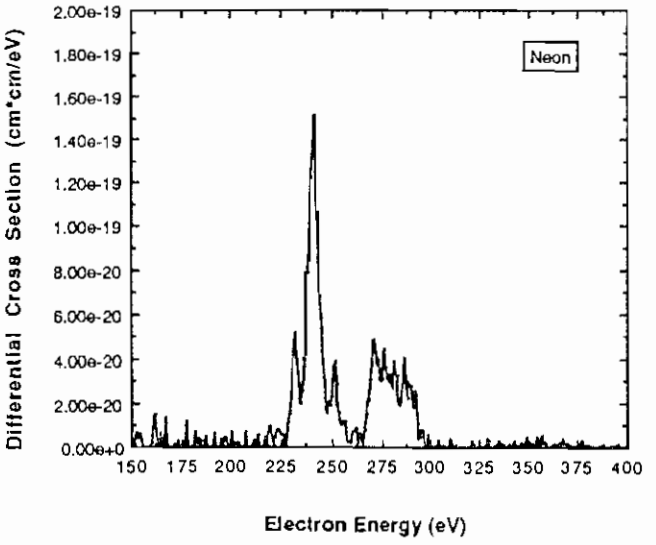
Neon
Differential Cross Section (cm*cm/eV)
2.00e-19
1.80e-19
1.60e-19
1.40e-19
1.20e-19
1.00e-19
8.00e-20
6.00e-20
4.00e-20
2.00e-20
0.00e+0
150 175 200 225 250 275 300 325 350 375 400
Electron Energy (eV)

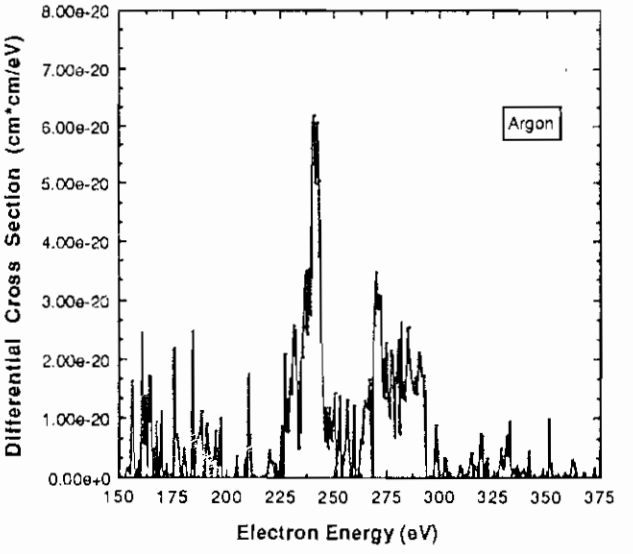
Argon
Differential Cross Section (cm*cm/eV)
8.00e-20
7.00e-20
6.00e-20
5.00e-20
4.00e-20
3.00e-20
2.00e-20
1.00e-20
0.00e+0
150 175 200 225 250 275 300 325 350 375
Electron Energy (eV)

Figure 19 Decelerated projectile K-LL Auger electron spectra for 4MeV collisions of C^{4+} ions with molecular Hydrogen, Helium and Neon gas targets. The deceleration bias was 693.2 Volts and the laboratory frame observation angle was 10.2°.

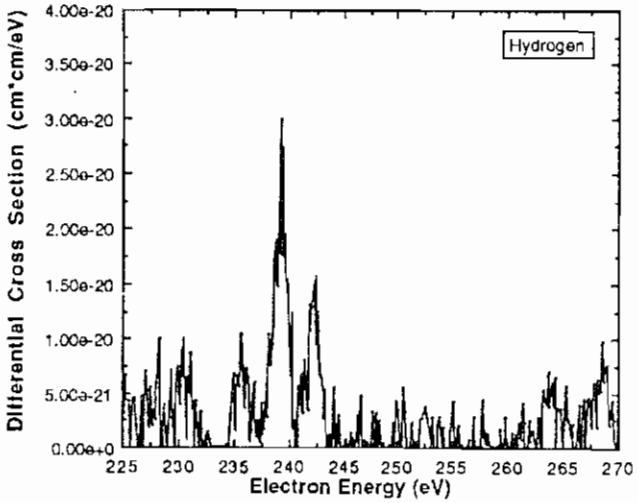
Hydrogen
Differential Cross Section (cm*cm/eV)
4.00e-20
3.50e-20
3.00e-20
2.50e-20
2.00e-20
1.50e-20
1.00e-20
5.00e-21
0.00e+0
225 230 235 240 245 250 255 260 265 270
Electron Energy (eV)

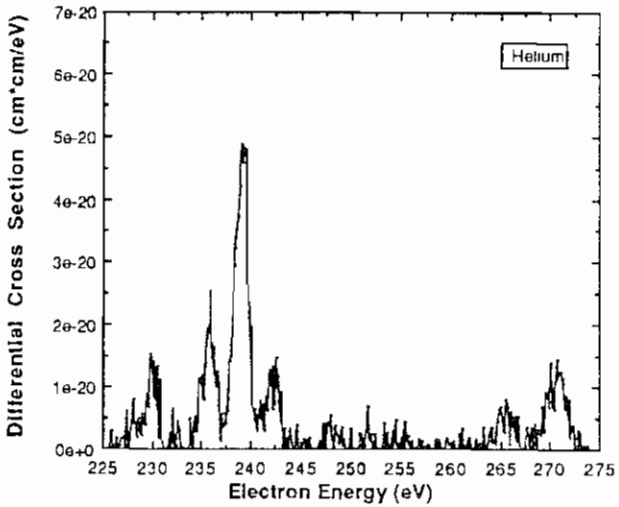
Helium
Differential Cross Section (cm*cm/eV)
7e-20
6e-20
5e-20
4e-20
3e-20
2e-20
1e-20
0e+0
225 230 235 240 245 250 255 260 265 270 275
Electron Energy (eV)

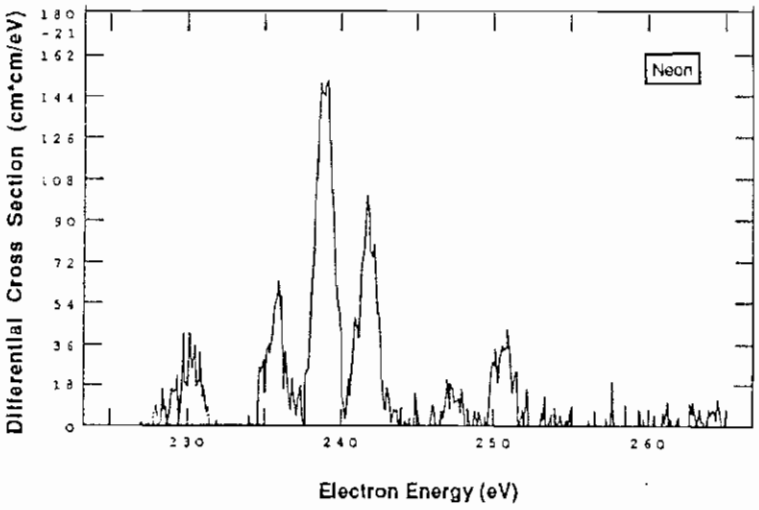
Neon
Differential Cross Section (cm*cm/eV)
180
162
144
126
108
90
72
54
36
18
0
230 240 250 260
Electron Energy (eV)

Figure 20 Decelerated projectile K Auger electron spectra for 4 MeV collisions of C^{4+} ions with molecular Helium and Neon. The deceleration bias was 736 Volts and the laboratory frame observation angle was 10.2°.

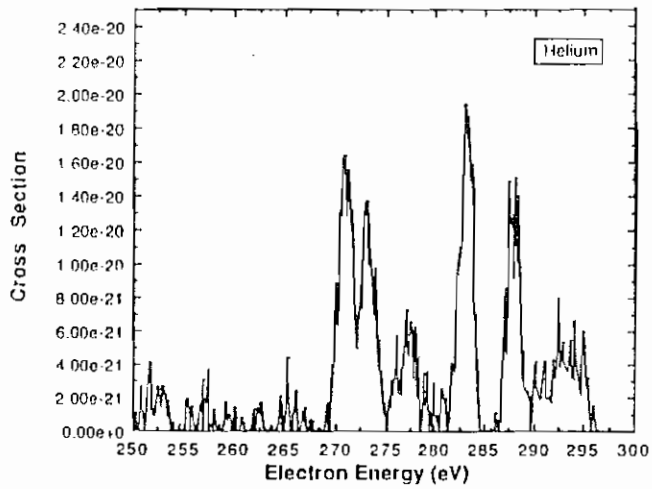
Helium
Cross Section
2.40e-20
2.20e-20
2.00e-20
1.80e-20
1.60e-20
1.40e-20
1.20e-20
1.00e-20
8.00e-21
6.00e-21
4.00e-21
2.00e-21
0.00e+0
250 255 260 265 270 275 280 285 290 295 300
Electron Energy (eV)

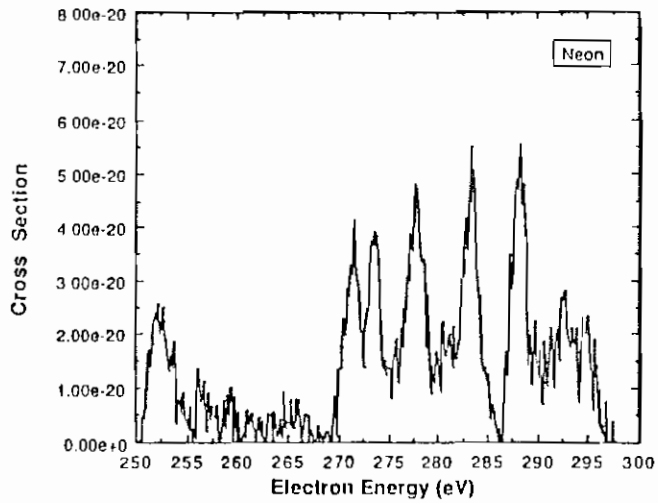
Neon
Cross Section
8.00e-20
7.00e-20
6.00e-20
5.00e-20
4.00e-20
3.00e-20
2.00e-20
1.00e-20
0.00e+0
250 255 260 265 270 275 280 285 290 295 300
Electron Energy (eV)

Figure 21 Undecelerated projectile K-Auger electron spectra for 5 MeV collisions of C^{4+} ions with molecular Hydrogen, Helium and Neon. The laboratory frame observation angle was 9.6°.

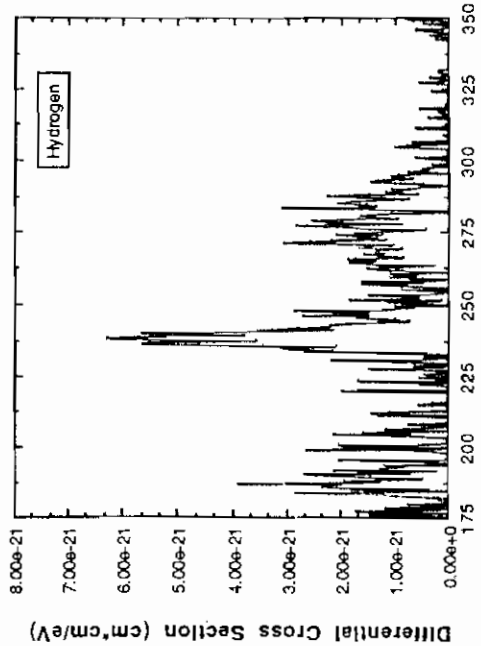
Hydrogen
Differential Cross Section (cm²/cm/eV)
Electron Energy (eV)
8.00e-21
7.00e-21
6.00e-21
5.00e-21
4.00e-21
3.00e-21
2.00e-21
1.00e-21
0.00e+0
175
200
225
250
275
300
325
350

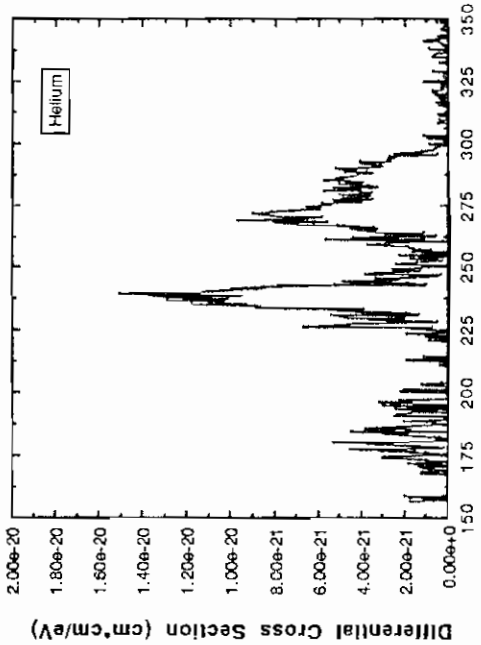
Helium
Differential Cross Section (cm²/cm/eV)
Electron Energy (eV)
2.00e-20
1.80e-20
1.60e-20
1.40e-20
1.20e-20
1.00e-20
8.00e-21
6.00e-21
4.00e-21
2.00e-21
0.00e+0
150
175
200
225
250
275
300
325
350

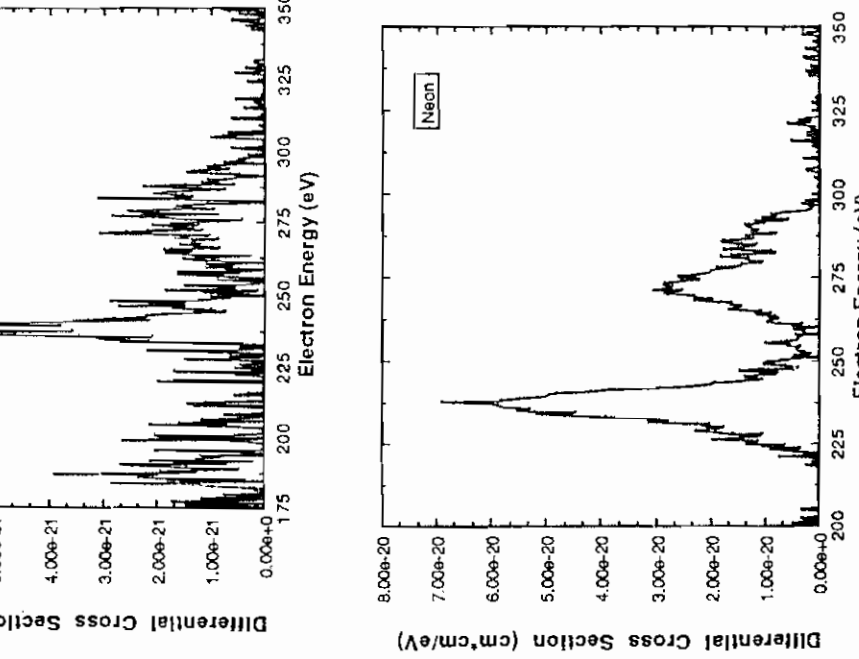
Neon
Differential Cross Section (cm²/cm/eV)
Electron Energy (eV)
8.00e-20
7.00e-20
6.00e-20
5.00e-20
4.00e-20
3.00e-20
2.00e-20
1.00e-20
0.00e+0
200
225
250
275
300
325
350

Figure 22 Projectile K-Auger electron spectra for 5 MeV collisions of C^{4+} ions with molecular Hydrogen, and Helium (Neon not shown) gas targets. The deceleration bias was 759.5 Volts and the laboratory frame observation angle was 9.6°.

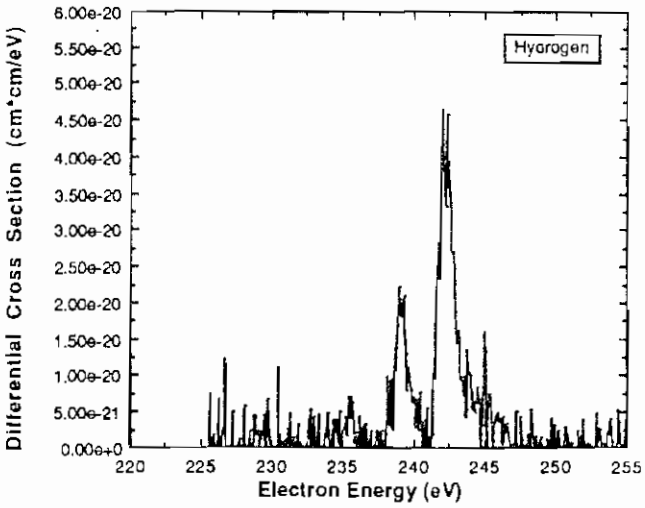
Hyarogen
Differential Cross Section (cm²cm/eV)
6.00e-20
5.50e-20
5.00e-20
4.50e-20
4.00e-20
3.50e-20
3.00e-20
2.50e-20
2.00e-20
1.50e-20
1.00e-20
5.00e-21
0.00e+0
220
225
230
235
240
245
250
255
Electron Energy (eV)

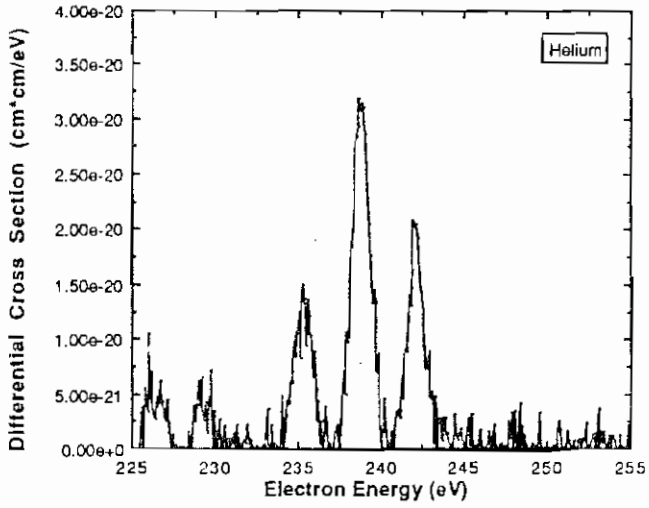
Helium
Differential Cross Section (cm²cm/eV)
4.00e-20
3.50e-20
3.00e-20
2.50e-20
2.00e-20
1.50e-20
1.00e-20
5.00e-21
0.00e+0
225
230
235
240
245
250
255
Electron Energy (eV)

Figure 23 Undecelerated projectile K-Auger electron spectra for 6 MeV collisions of C^{4+} ions with molecular Hydrogen, Helium, Neon, and Argon. The laboratory frame observation angle was 9.6°.

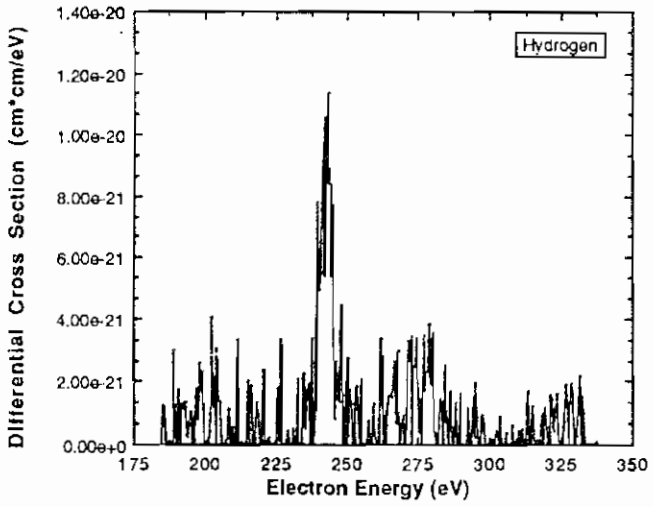
Hydrogen
Differential Cross Section (cm*cm/eV)
1.40e-20
1.20e-20
1.00e-20
8.00e-21
6.00e-21
4.00e-21
2.00e-21
0.00e+0
175 200 225 250 275 300 325 350
Electron Energy (eV)

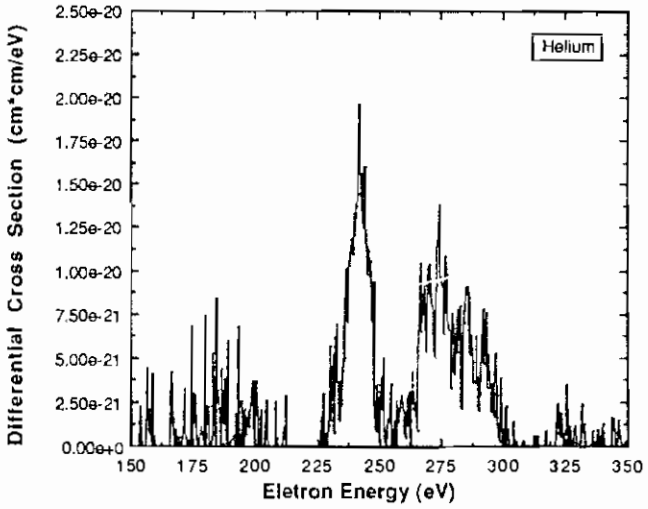
Helium
Differential Cross Section (cm*cm/eV)
2.50e-20
2.25e-20
2.00e-20
1.75e-20
1.50e-20
1.25e-20
1.00e-20
7.50e-21
5.00e-21
2.50e-21
0.00e+0
150 175 200 225 250 275 300 325 350
Eletron Energy (eV)

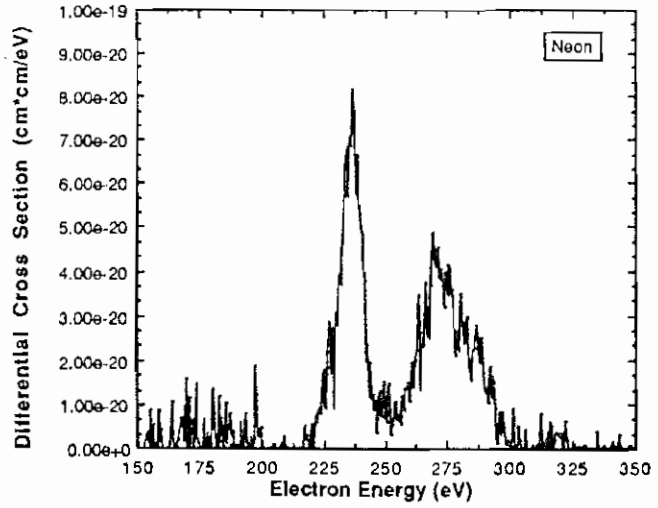
Neon
Differential Cross Section (cm*cm/eV)
1.00e-19
9.00e-20
8.00e-20
7.00e-20
6.00e-20
5.00e-20
4.00e-20
3.00e-20
2.00e-20
1.00e-20
0.00e+0
150 175 200 225 250 275 300 325 350
Electron Energy (eV)

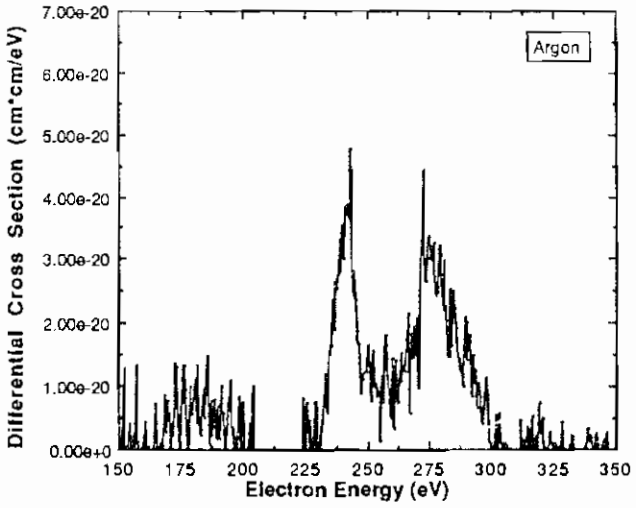
Argon
Differential Cross Section (cm*cm/eV)
7.00e-20
6.00e-20
5.00e-20
4.00e-20
3.00e-20
2.00e-20
1.00e-20
0.00e+0
150 175 200 225 250 275 300 325 350
Electron Energy (eV)

Figure 24 K-Auger electron spectra for 6 MeV collisions of C^{4+} ions with molecular Hydrogen, Helium and Neon gas targets. For the Helium and Hydrogen targets, the deceleration bias was 830.7 Volts, and the lab frame observation angle was 9.6°. For the Neon target, the deceleration bias was 823 Volts, and the lab frame observation angle was 10.4°.

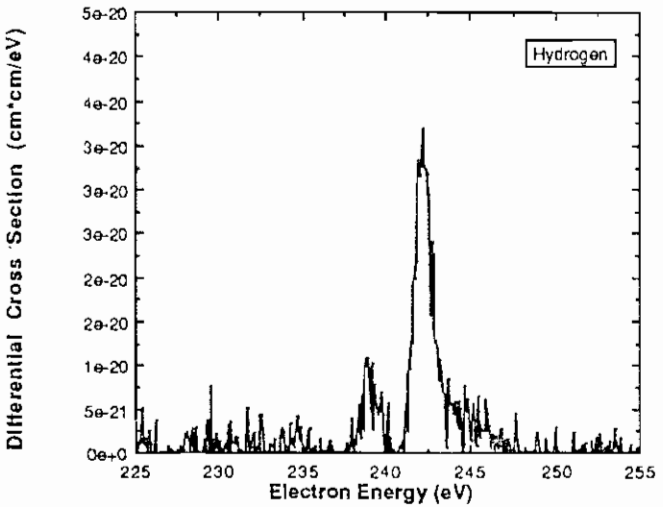
Hydrogen
Differential Cross Section (cm*cm/eV)
Electron Energy (eV)
5e-20
4e-20
4e-20
3e-20
3e-20
3e-20
2e-20
2e-20
1e-20
5e-21
0e+0
225
230
235
240
245
250
255

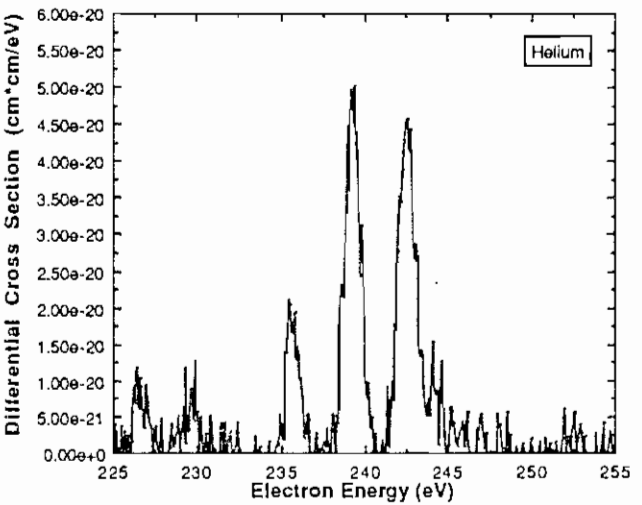
Helium
Differential Cross Section (cm*cm/eV)
Electron Energy (eV)
6.00e-20
5.50e-20
5.00e-20
4.50e-20
4.00e-20
3.50e-20
3.00e-20
2.50e-20
2.00e-20
1.50e-20
1.00e-20
5.00e-21
0.00e+0
225
230
235
240
245
250
255

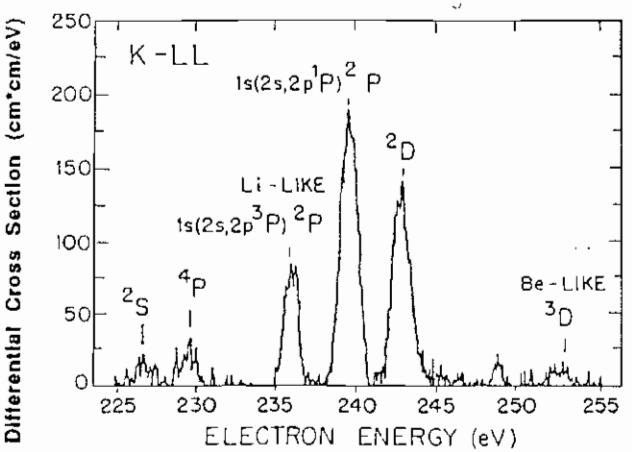
K-LL
1s(2s,2p 1P) 2 P
2D
Li-LIKE
1s(2s,2p 3P) 2P
4P
2S
Be-LIKE
3D
Differential Cross Section (cm*cm/eV)
ELECTRON ENERGY (eV)
250
200
150
100
50
0
225
230
235
240
245
250
255

Figure 25 Undecelerated projectile K-Auger electron spectra for 7 MeV collisions of C^{4+} ions with molecular Hydrogen, Helium, and Neon gas targets. The laboratory frame observation angle was 9.6°.

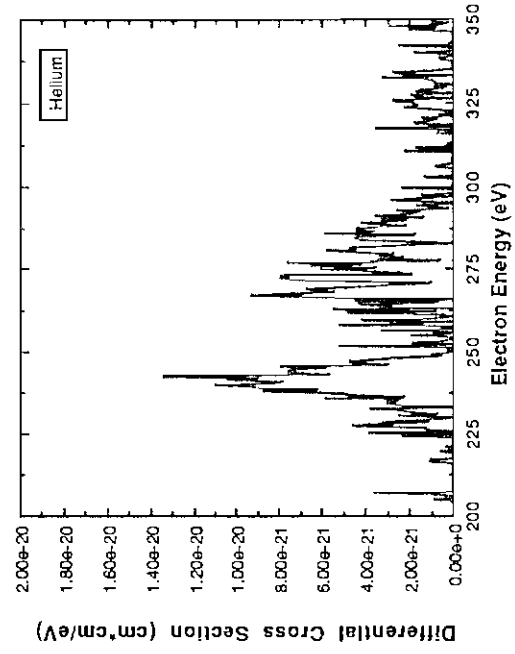
Helium
Differential Cross Section (cm²/cm/eV)
Electron Energy (eV)
2.00e-20
1.80e-20
1.60e-20
1.40e-20
1.20e-20
1.00e-20
8.00e-21
6.00e-21
4.00e-21
2.00e-21
0.00e+0
200
225
250
275
300
325
350

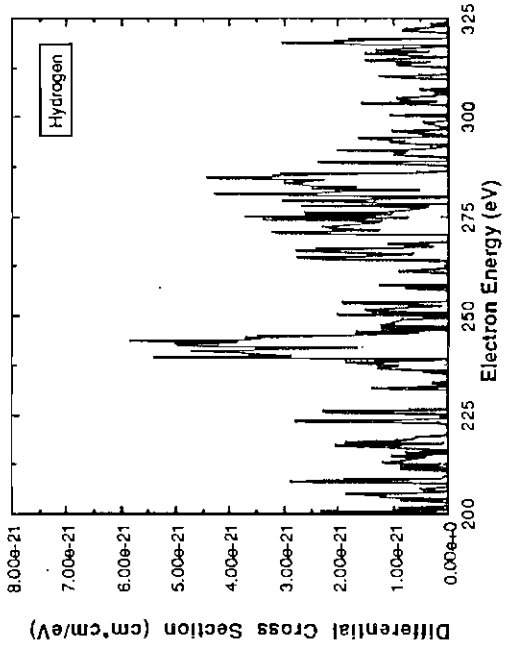
Hydrogen
Differential Cross Section (cm²/cm/eV)
Electron Energy (eV)
8.00e-21
7.00e-21
6.00e-21
5.00e-21
4.00e-21
3.00e-21
2.00e-21
1.00e-21
0.00e+0
200
225
250
275
300
325

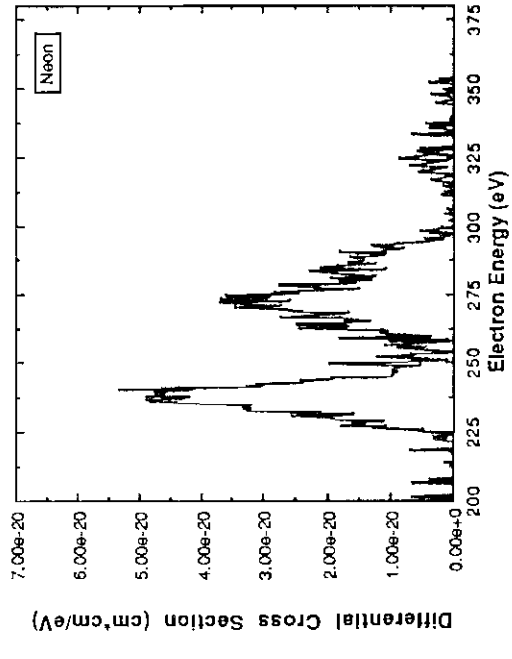
Neon
Differential Cross Section (cm²/cm/eV)
Electron Energy (eV)
7.00e-20
6.00e-20
5.00e-20
4.00e-20
3.00e-20
2.00e-20
1.00e-20
0.00e+0
200
225
250
275
300
325
350
375

Figure 26 Decelerated projectile K-Auger electron spectra for 7 MeV collisions of C^{4+} ions with molecular Hydrogen, Helium, and Neon gas targets. The deceleration bias was 898.6 Volts and the laboratory frame observation angle was 9.6°.

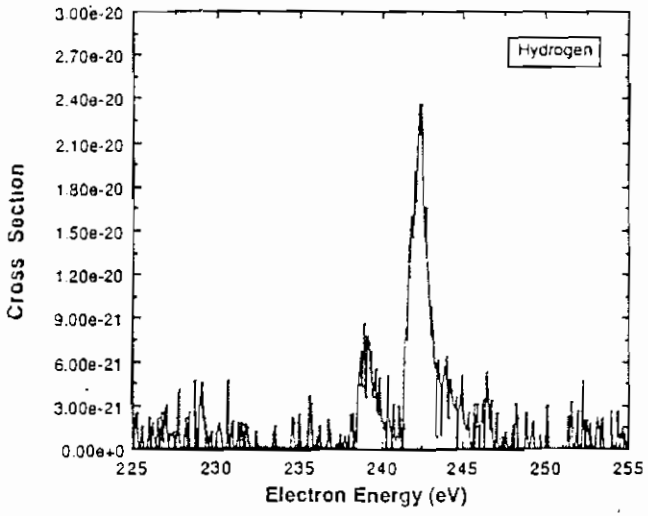
Hydrogen
Cross Section
3.00e-20
2.70e-20
2.40e-20
2.10e-20
1.80e-20
1.50e-20
1.20e-20
9.00e-21
6.00e-21
3.00e-21
0.00e+0
225
230
235
240
245
250
255
Electron Energy (eV)

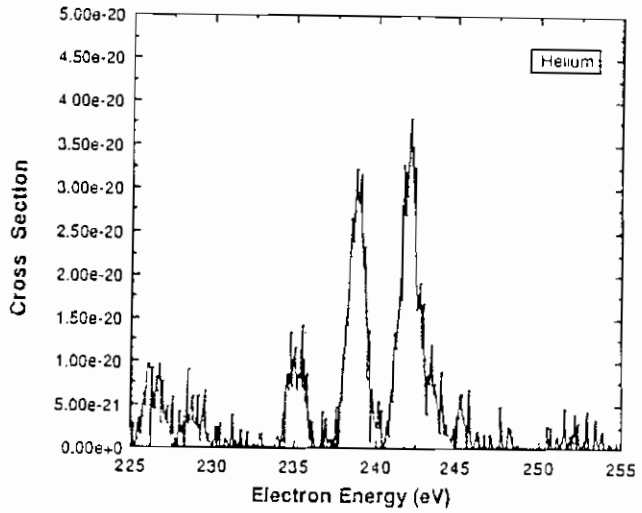
Helium
Cross Section
5.00e-20
4.50e-20
4.00e-20
3.50e-20
3.00e-20
2.50e-20
2.00e-20
1.50e-20
1.00e-20
5.00e-21
0.00e+0
225
230
235
240
245
250
255
Electron Energy (eV)

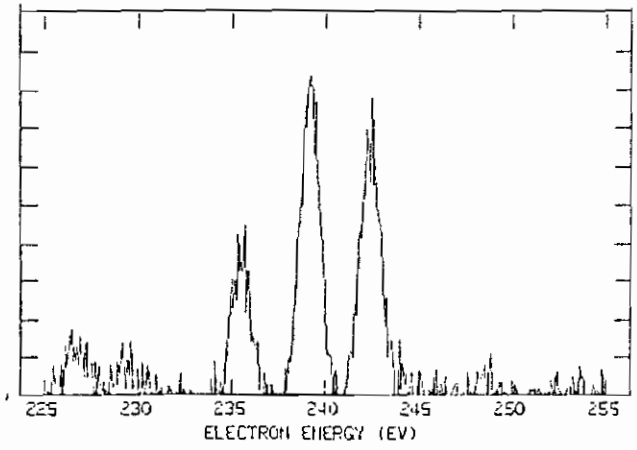
225
230
235
240
245
250
255
ELECTRON ENERGY (EV)

Figure 27 Undecelerated projectile K-Auger electron spectra for 8 MeV collisions of C^{4+} ions with Hydrogen, Helium, and Neon gas targets. The laboratory frame observation angle was 9.6°.

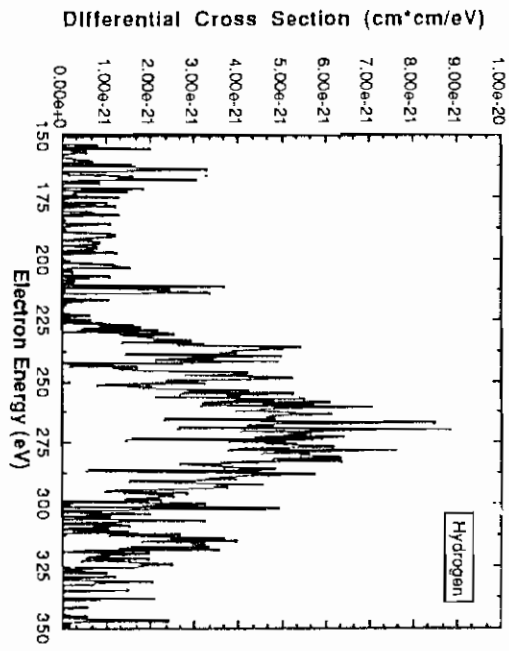
Differential Cross Section (cm*cm/eV)
1.00e-20
9.00e-21
8.00e-21
7.00e-21
6.00e-21
5.00e-21
4.00e-21
3.00e-21
2.00e-21
1.00e-21
0.00e+0
150 175 200 225 250 275 300 325 350
Electron Energy (eV)
Hydrogen

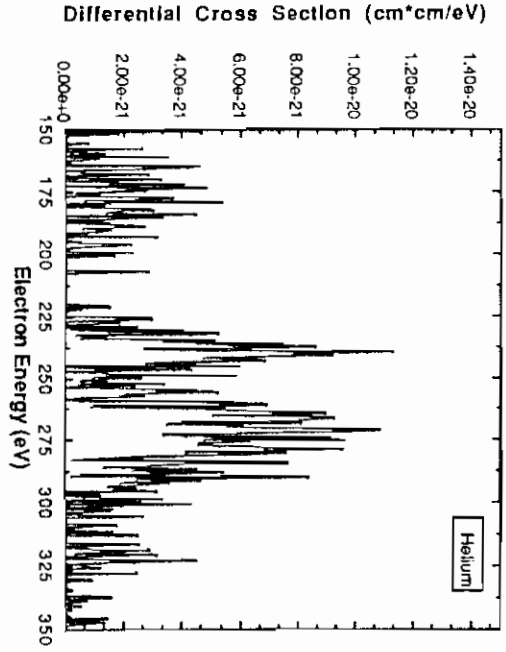
Differential Cross Section (cm*cm/eV)
1.40e-20
1.20e-20
1.00e-20
8.00e-21
6.00e-21
4.00e-21
2.00e-21
0.00e+0
150 175 200 225 250 275 300 325 350
Electron Energy (eV)
Helium

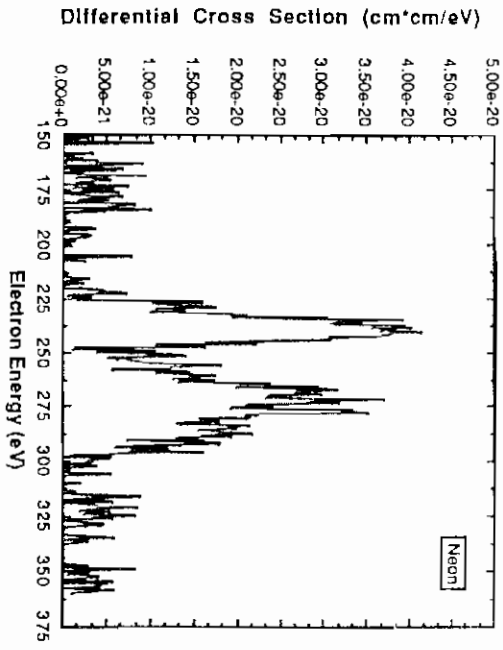
Differential Cross Section (cm*cm/eV)
5.00e-20
4.50e-20
4.00e-20
3.50e-20
3.00e-20
2.50e-20
2.00e-20
1.50e-20
1.00e-20
5.00e-21
0.00e+0
150 175 200 225 250 275 300 325 350 375
Electron Energy (eV)
Neon

Figure 28 Decelerated projectile K-Auger electron spectra for 8 MeV collisions of C^{4+} ions with molecular Hydrogen, Helium, and Neon gas targets. The deceleration bias was 964.2 Volts and the laboratory frame observation angle was 9.6°.

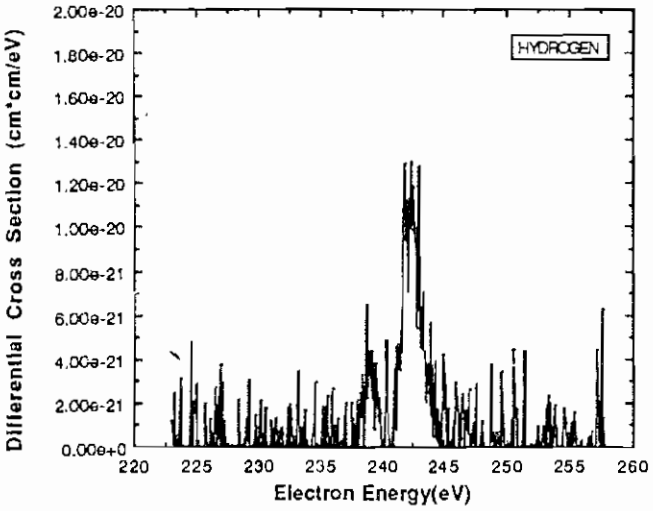
HYDROGEN
Differential Cross Section (cm*cm/eV)
2.00e-20
1.80e-20
1.60e-20
1.40e-20
1.20e-20
1.00e-20
8.00e-21
6.00e-21
4.00e-21
2.00e-21
0.00e+0
220
225
230
235
240
245
250
255
260
Electron Energy(eV)

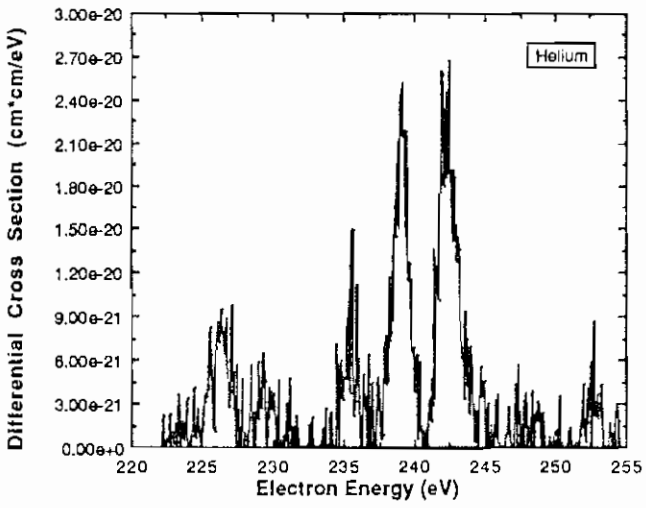
Helium
Differential Cross Section (cm*cm/eV)
3.00e-20
2.70e-20
2.40e-20
2.10e-20
1.80e-20
1.50e-20
1.20e-20
9.00e-21
6.00e-21
3.00e-21
0.00e+0
220
225
230
235
240
245
250
255
Electron Energy (eV)

5 DISCUSSION AND CONCLUSIONS

5.1. Introduction

When stripping is used to increase the charge of fast Carbon ions, excited configurations produced in the process usually decay promptly (eg. $\tau \approx 1.1 \times 10^{-12}$ sec. for 1s2p ^{1}P ions). However, for two-electron ions the metastable 1s2s ^{3}S configuration ($\tau = 2.01 \times 10^{-2}$ sec.[1]) arrives on target without decay. Measurements of the fraction of vacancy bearing two-electron ions at various incident energies can be found in the literature. Their measurement is based on projectile to target K-shell vacancy transfer. 1s2s ^{3}S ions have been used to study partial cross sections for capture to specific n or n,l shells[68] ($n \geq 2$) . When our Auger electron production cross sections are divided by published values of the fraction of 1s2s ^{3}S ions in the incident beam[69], we find that the energy dependance of these inferred electron capture cross sections agrees with a classical Bohr-Linhardt calculation[70] for capture by $C^{4+}(1s^2)$ ions. However, the data overpredict the calculation and we attribute this, in part, to differences in screening by $1s^2$ and 1s2s ions. The high resolution K-LL Auger spectrum is composed of decays of five Li-like configurations. Three are thought to be formed directly by electron capture into the 2p subshell and one by capture into the 2s subshell. Auger electron production from the decay of the $1s2p^2$ ^{2}D configuration exhibits a maximum intensity at a collision energy of 5 MeV, and agrees well with theoretical calculations for resonant transfer and excitation (RTE). Also, a maximum in the cross sections at 6 MeV for unresolved transitions containing capture to $n \geq 3$ as well as the doubly core excited $2s^22p$ ^{2}P and $2s2p^2$ ^{2}D configuration decaying to either 1s2s ^{1}S or ^{3}S, agrees with the predicted collision energy for a maximum in the RTE cross section.

Electron transfer excitation cross sections are needed in the fields of thermonuclear fusion, heavy ion storage ring and x-ray laser design, as well as for astrophysical model

calculations. In particular, RTE is closely related to dielectronic recombination - a significant energy loss mechanism in tokamak plasmas. DR, in which a fast free electron is captured by a slow ion, can be viewed as the inverse Auger process. The probability for DR depends strongly on the kinetic energy of the free electron and, if the time reversal analogy is correct, we expect this dependance to reflect the kinetic energy distribution of electrons emitted during Auger decay. The RTE process occurs in ion atom collisions when the velocity of the ion is varied so that the kinetic energy (in the ion's rest frame) of a loosely bound target electron appears to pass through a DR type resonance.

Recently, two experimenters have reported the observation of RTE using the technique of 0° Auger spectroscopy. Swenson et. al. (see reference 37) studied the O^{5+} + He system and found resonances in the production of $1s2s2p^2\ ^1D$ and ^3D excited states. Itoh et. al. reported a similar resonance (see reference 36) in the production of the $2p^2\ ^1D$ state for the symmetric He^+ + He collision system. In these experiments a target electron is captured by the ion which emerges from the collision complex in an excited configuration. Since no measurement is made on the target fragment, we know only that it is at least singly ionized, but may also be excited and multiply ionized. When the captured electron is emitted during the Auger decay, a new channel for target ionization is opened:

$$(5.1) \qquad P^{Q+}(^{2S+1}L) + T \underset{\text{RTE}}{\rightarrow} P^{(Q-1)+}(^{2S+1}L) + T^{+} \underset{\text{Auger decay}}{\rightarrow} P^{Q+} + T^{+} + e^{-}(E_{Aug})$$

where ^{2S+1}L is the incident ionic configuration, ^{2S+1}L is the excited configuration formed through RTE, T is the target, and T^+ refers to the system composed of the remaining target electrons and nucleus. Destructive interference between this process and direct target ionization has been discussed by Swenson et. al. to explain anomalies in their K-LL Auger spectrum.

As in DR, a maximum in the RTE production probability occurs when the difference between the captured electron's kinetic energy (KE) and its initial binding energy to the target (B) becomes equal to the energy difference between the excited and incident

configurations: KE - B = $E(^{2S+1}L) - E(^{2S+1}L)$. Examination of (1) shows that this occurs when the collision energy is: $E_{RTE} = M_{ion}/m_{electron}\ (E_{Aug} - B)$. Brandt has shown that the momentum distribution of the bound target electron broadens the resonance as a result of orbital motion in the direction of the collision axis. This problem has been treated in the impulse approximation (see reference 33), and a method has been developed to relate DR to RTE using the bound electron's Compton profile.

5.2 Experiment

10-30 μA currents of C^- were produced in a sputter ion source, and accelerated by the Triangle Universities Nuclear Laboratory model FN tandem Van de Graaff. C^{4+} ions were then formed by post acceleration stripping and selected magnetically. The distance from post stripper foil to the target cell was 9 meters. After collimation, the ions passed through a 25 mm long target cell with 2 stages of differential pumping, and were collected in a suppressed Faraday cup. Periodic checks of target current without gas in the cell showed no detectable enhancement or neutralization due to the gas. Pressure studies were done with Neon to insure single collision conditions. Projectile Auger yields were found to be linear up to 30 mTorr (39.5 μbar).

Typical spectra are shown in figure 29. They have been background subtracted and transformed into the rest frame of the projectile. The improved resolution in figure 29 b was obtained by decelerating the electrons to 1/6 of their lab frame energy before passing through the spectrometer. Since the electron pass energy was not a constant for the various collision energies, the decelerated spectra were normalized by a deceleration efficiency factor determined at each collision energy: $\varepsilon_{decel} = \frac{\text{Yield(decelerated)}}{\text{Yield(undecelerated)}}$.

5.3 K-LL Auger Spectrum and Capture to n=2

Figure 30a shows the total capture cross sections into all n≥2 shells of $1s2s\ ^3S$ ions for the various targets, and includes all K-L Auger transitions (227.5 - 299 eV). The Hydrogen data was divided by two, in order to compare with the atomic cross sections for

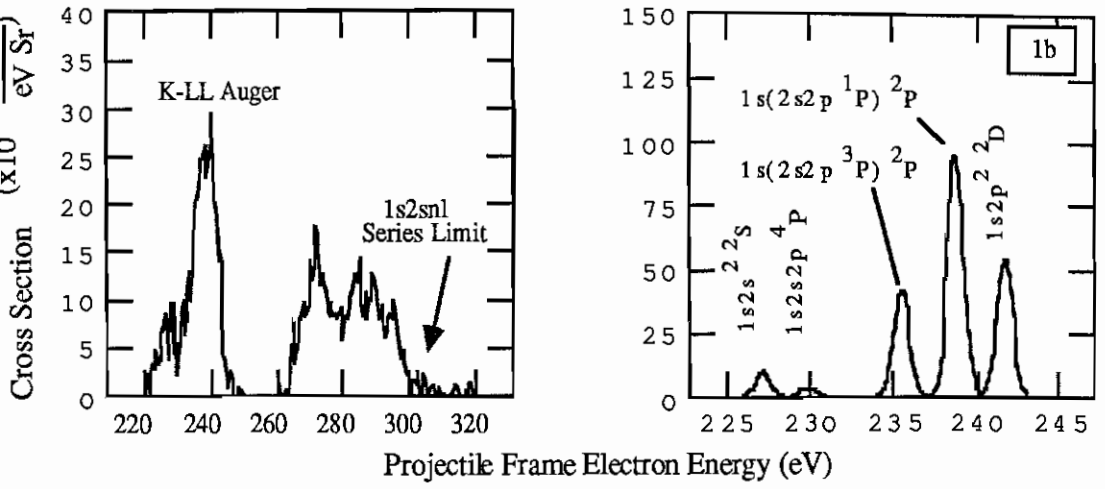

Figure 29 K-L (figure a) and K-LL (figure b) Auger spectrum of Carbon formed in 5 MeV collisions of C^{4+} with Helium. The Gaussian fits to the raw spectra in 1b shows improved resolution (0.5% FWHM) resulting from decelerating Auger electrons before the analyzer. The excited states shown in 1b decay to $1s^2\ ^1S$.

He and Ne. Others have found[71] the ratio for capture from molecular and atomic Hydrogen targets to be 3.89, and we do not mean to attach any special significance to our proceedure. Figure 30a also shows Brandt's semiclassical calculation for the He target (reference 70) as the solid curve. As discussed above, the calculation underpredicts our data by a numerical factor of 4.5.

Ratios of cross sections for capture into specific L-S coupled configurations by 1s2s ^3S ions are shown in table 2. They were obtained from the doubly differential high resolution spectra similar to figure 29b.

Capture into the 2s sub-shell of metastable projectiles always results in the $1s2s^2\ ^2S$, while capture into the 2p sub-shell can result in the $1s(2s2p\ ^3P)\ ^2P$; $1s(2s2p\ ^1P)\ ^2P$; or $1s2s2p\ ^4P$. The relative strengths of the $1s(2s2p\ ^3P)\ ^2P$ and $1s(2s2p\ ^1P)$ configurations indicate that capture into the empty 2p sub-shell is statistical. From tables of fractional

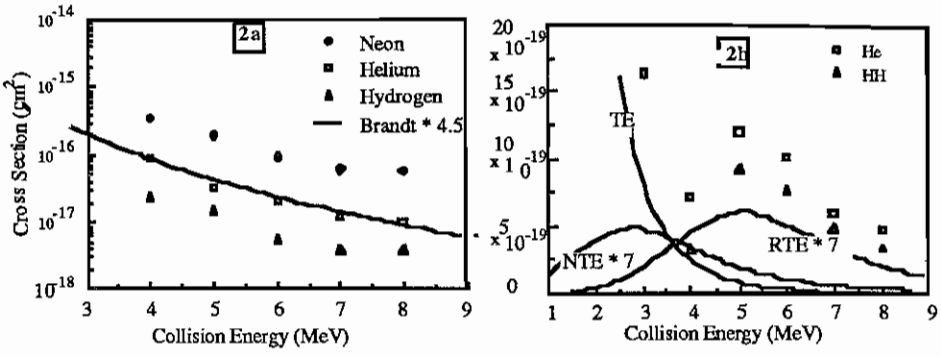

Figure 30 Inferred cross sections for capture into all sub-shells with n≥2 by 1s2s ^{3}S ions from H_2, He, and Ne targets is shown in figure a. (Auger production cross sections were divided by the fraction of metastables at each collision energy). Figure 30b shows shows the 1s2p^2 ^{2}D - 1s^2 ^{1}S Auger production cross section as well as calculations for RTE, NTE, TE production schemes (Auger production cross sections were divided by the fraction of ground state ions at each collision energy).

Table 2 Intensity fraction of metastable ions in the incident beam at the various collision energies. Columns 3 and 4 give observed Auger electron production ratios for configurations formed by direct electron capture into 2s and 2p sub-shells of C^{4+}(1s2s ^{3}S) ions in collisions with He.

COLLISION ENERGY(MeV)	1s2s ^{3}S METASTABLE FRACTION	$\frac{\sigma[1s(2s2p\ ^1P)\ ^2P]}{\sigma[1s(2s2p\ ^3P)\ ^2P]}$	$\frac{\sigma[1s2s^2\ ^2S]}{\sigma[1s(2s2p\ ^3P)\ ^2P]}$
3	0.16	2.80	0.12
4	0.21	2.35	0.21
5	0.24	2.00	0.17
6	0.26	2.89	0.20
7	0.27	2.88	0.28
8	0.28	2.77	0.42
15	0.29	2.2	0.45

parentage coeficients[72]:

$$|< 1s2s\ ^3S,\ 2pl\} \ 1s\ (2s2p\ ^1P)\ ^2P>|^2 = 3\ |<1s2s\ ^3S,\ 2pl\}\ 1s\ (2s2p\ ^3P)\ ^2P>|^2 \quad (5.2)$$

$$\text{and} \quad |<1s2s\ ^3S,\ 2pl\}\ 1s\ 2s2p\ ^4P>|^2 = \frac{4}{3}\ |<1s2s\ ^3S,\ 2pl\}\ 1s\ (2s2p\ ^1P)\ ^2P>|^2$$

This equation gives the statistical ratios for coupling the 1s2s ^{3}S preparent and 2p coparent to either 1s2s2p ^{2}P or 1s2s2p ^{4}P postparents. Specifying either the (2s2p ^{1}P) or (2s2p ^{3}P) intermediate coupling removes any ambiguity in the 1s2s2p ^{2}P postparent. The director (l}) leads from lower symmetry to higher symmetry. We find that the experimental ratio for capture into the different 1s2s2p ^{2}P configurations is nearly equal to the ratio of 3:1 as predicted above.

The excited 1s2p^2 ^{2}D configuration cannot be formed directly by single electron capture to either component of the incident projectile beam. Instead, it is formed when a target electron is captured and an additional projectile electron is excited into a 2p orbital during the same collision. The situation becomes even more complex when we consider that the excitation may result from the time varying potential of either the target nucleus, or the target electrons. The 1s2p^2 ^{2}D configuration can be formed from 1s2s ^{3}S Carbon ions when capture into the 2p orbital is accompanied by 2s-2p excitation. This channel is shown in figure 30b as the monotonically decreasing curve. The probabilities $P_{2s\text{-}2p}(b)$ and $P_{1s\text{-}2p}(b)$ were calculated analytically in the semiclassical approximation with individually screened hydrogenic wave functions[73]. The calculation assumes a straight line trajectory for the projectile, and no target recoil. $P_{capt}(b)$ was formulated by Brandt based on a two step Bohr-Lindhardt model (see reference 70). In the first step, an electron is released by the target when the target binding potential is overcome by the attractive potential of the projectile. Capture by the projectile can then occur if the distance from the projectile at the time of release is smaller than $R_C=2q/(v_{proj})^2$ (that is if the electron's kinetic energy is smaller than its potential energy in the field of the projectile). The TE curve is then calculated according to:

(5.3) $$\sigma_{IE}(1s2s\ ^3S \rightarrow 1s2p^2\ ^2D) = 2\pi \int P_{exc}^{2s\text{-}2p}(b)\, P_{capt}^{2p}(b)\, b\, db \quad \text{where} \quad P_{capt}^{2p}(b) \approx \frac{1}{2} P_{capt}(b)$$

Since the calculation does not give partial probabilities for capture into specific orbitals of the projectile, we have used the $1/n^3$ scaling law in equation 5.3 and assumed that capture into 2s is negligible to estimate that ~1/2 of all capture is into a 2p orbital.

The $1s2p^2\ ^2D$ can also be formed in collisions with $1s^2$ ground state projectiles. In this case, a 1s-2p excitation accompanies capture into the 2p orbital. This process has been considered before and is known as non resonant transfer excitation (NTE). Since the incident ion is now in the $1s^2$ state, the statistical ratio of capture into 2p to capture into all $n \geq 2$ is 1/3:

(5.4) $$\sigma_{NTE}(1s^2\ ^2S \rightarrow 1s2p^2\ ^2D) = 2\pi \int P_{exc}^{1s\text{-}2p}(b)\, P_{capt}^{2p}(b)\, b\, db \quad \text{with} \quad P_{capt}^{2p}(b) = \frac{1}{3} P_{capt}(b)$$

The NTE calculation is shown in figure 30b and peaks at a collision energy of ~3 MeV.

One final mechanism for producing the $1s2p^2\ ^2D$ configuration is through RTE. This production mechanism is similar to NTE in that a 1s-2p excitation occurs when a $1s^2\ ^1S$ ion captures an electron into a 2p orbital. However, the excitation is now the result of internal conversion of the captured electron's kinetic energy. As shown in figure 30b, a maximum in the RTE production for the $C^{4+}(1s^2\ ^1S)$ + He collision system is predicted at ~5 MeV in agreement with the data. The RTE calculation was provided by McLaughlin, and uses the method outlined by Brandt (see reference 33) for folding the target electron's Compton profile with calculated DR cross sections.

5.4 Hyper-satellites and Capture to n≥3

High resolution spectra for Carbon K-Auger electrons with energy greater than 250 eV are shown in figure 31. They are the result of 4 MeV collisions of C^{4+} with He (figure 31a) and Ne (figure 31b). Each peak is labeled and identified in table 3. As shown there, the excited configurations are formed chiefly by capture into $n \geq 3$ shells of $1s2s\ ^3S$ ions. As n increases, it becomes more difficult to resolve the various transitions. Capture into 3s and 3p (peak 1) is resolved from capture into 3d (peak 2). However, for capture into n =

4, we are unable to resolve capture into the various 4l subshells (peak 4). Also, capture into shells with $n \geq 5$ (region 6) are essentially unresolved. The Auger electron energy for the $(1s2s\ ^3S)nl$ series limit to $1s^2\ ^1S$ decay occurs at ~299 eV (reference 19). Also identified in table 3 are the hypersatelite Auger transitions corresponding to $2s^22p\ ^2P$ and $2s2p^2\ ^2D$ configurations decaying to either $1s2s\ ^1S$ or $1s2s\ ^3S$ (peaks 3,4,5). The energies for these transitions were calculated by Chung and Davis[74].

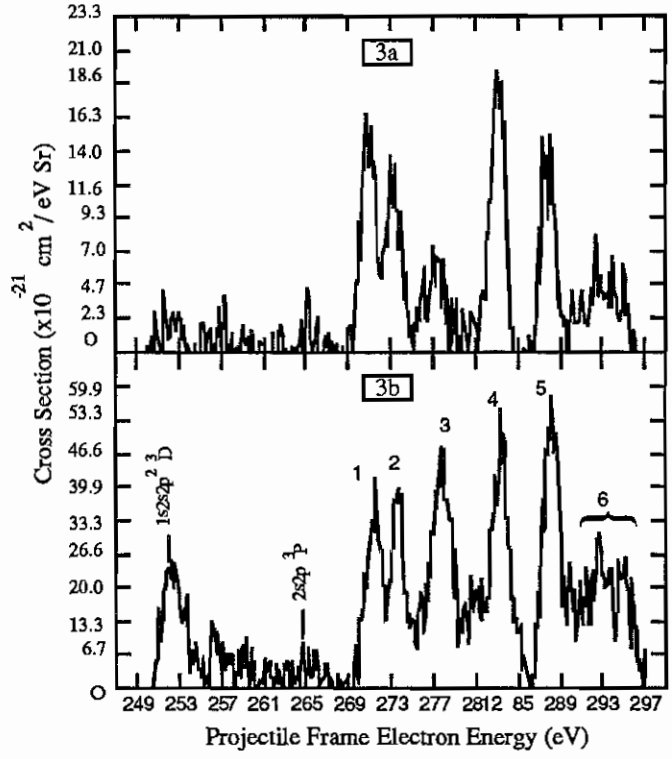

Figure 31 High resolution Auger electron production spectra of Carbon formed in 4 MeV collisions of C^{4+} with He (3a) and Ne (3b).

Figure 32 shows inferred capture cross sections into all $n \geq 3$ shells of metastable C^{4+} ions. They were obtained by dividing production cross sections for all Auger electrons having energies between ~269eV and 299 eV by the metastable fractions given in table 2. Although all of the excited configurations contributing to Auger production in this range of emission energies result from capture into metastables, the hypersatelite transitions also fall

Table 3 Identification of Auger transitions for figure 31. The transitions in bold script are thought to be formed through RTE or NTE with incident $C^{4+}(1s2s\ ^3S)$, and their Auger decay energies were calculated by Chung (reference 74). Other transitions are identified in reference 19.

Table 2

Peak Number	Excited - Final Configuration	Energy (eV)
1	$(1s2s\ ^3S)3s\ ^2S - 1s^2\ ^1S$	269.6
	$(1s2s\ ^3S)3p\ ^2P - 1s^2\ ^1S$	271.9
2	$(1s2s\ ^3S)3d\ ^2D - 1s^2\ ^1S$	274.3
	$2s^2 2p\ ^2P - 1s2s\ ^1S$	**275.8**
3	$(1s2s\ ^1S)3s,p,d - 1s^2\ ^1S$	< 279
	$2s^2 2p\ ^2P - 1s2s\ ^3S$	**281.3**
4	$(1s2s\ ^3S)4s,p,d,f - 1s^2\ ^1S$	< 286
	$2s^2 2p\ ^2D - 1s2s\ ^1S$	**282.4**
5	$(1s2s\ ^1S)4s,p,d,f - 1s^2\ ^1S$	< 291
	$2s^2 2p\ ^2D - 1s2s\ ^3S$	**287.9**
6	$(1s2s\ ^3S)nl$ series limit - $1s^2\ ^1S$	< 299

in this range. The doubly core excited configurations can be formed by n=2 capture into metastable ions accompanied by 1s - 2s or 1s - 2p excitation such as occurs in either RTE or NTE. Indeed, the data shows an increase for all targets near the RTE resonance collisioin energy.

5.5 Discussion

The experimental ratios for production of the 1s(2s2p ^{1}P) ^{2}P to 1s(2s2p ^{3}P) ^{2}P configurations at the various collision energies are given in table 2. The 1s2s2p ^{2}P is formed directly when a Helium electron is captured into the 2p orbital of a metastable ion.

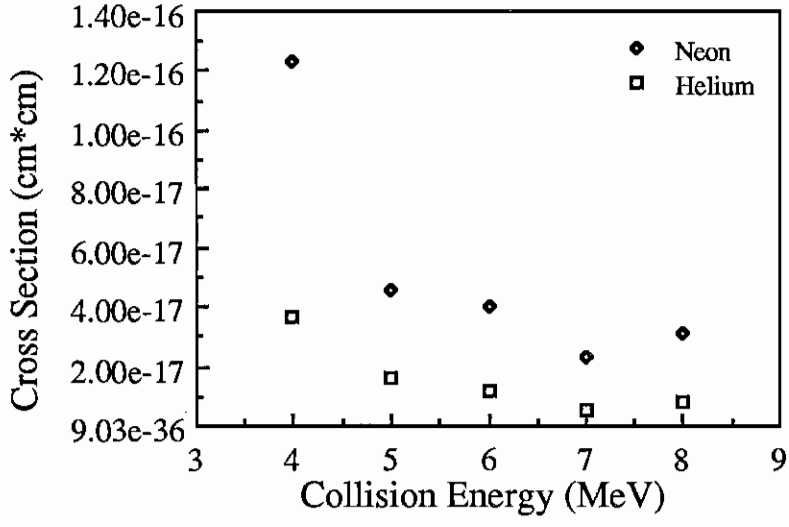

Figure 32 Inferred capture cross sections into all sub-shells with n≥3 by 1s2s ^{3}S projectiles. Capture cross sections are obtained by dividing Auger production cross sections by the fraction of metastable ions in the incident projectile beam at each collision energy.

Fractional parentage coefficients show that this ratio is 3.0 when a 2p electron is coupled into a 1s2s ^{3}S ion, and 1/3 when coupled into a 1s2s ^{1}S ion. Our measured ratios range

from 2.0 to 2.89 and indicate that 80% to 96% of the incident metastables are 1s2s ^{3}S.

Also shown in table 4 are the experimental production ratios for 1s2s^2 ^{2}S and 1s(2s2p ^{1}P) ^{2}P configurations. Based merely on the number of 2s and 2p vacancies in the incident 1s2s ^{3}S ions (one for 2s, and six for 2p) and since 3/8 of all 2p capture into these ions results in the 1s(2s2p ^{1}P) ^{2}P a ratio of 1s2s^2 ^{2}S to 1s(2s2p ^{1}P) ^{2}P production of .444 is expected. The experimental values are lower than .444 indicating that capture into the half full 2s subshell is strongly suppressed at low collision energies. This suppression is the result of the repulsive potential between the spectator and captured electrons. The data indicates that the repulsion becomes less important as the collision velocity is increased. At 3 MeV the collision velocity is about equal to the Bohr orbital velocity of the 2s electron, while at 15 MeV it is about 2.84 v_{2s}.

Since the spin-orbit interaction is negligible for Carbon, the orientation of the total spin vector (**S**) for electrons in the incident ion and that of the captured electron (**s**) should not effect the capture probability. For capture into a 2p orbital of 1s2s ^{3}S ions, 1s2s2p ^{4}P and 1s2s2p ^{2}P configurations should be produced with equal probability. Since the 1s2s2p ^{4}P - 1s^2 ^{1}S decay requires a spin flip, its mean life (eg. t=117 nsec for $^4P_{5/2}$) is greater than the transit time for ions over the spectrometer viewing region and only a fraction of the ^{4}P ions produced in this region decay before the ion exits. This is clearly shown in figure 32b where the 1s2s2p ^{4}P - 1s^2 ^{1}S appears as the weakest transition. In order to obtain absolute production cross sections, the measured intensity for this transition must be divided by an efficiency factor calculated at each collission energy:

$$\varepsilon_{1s2s2p\ ^4P\ -\ 1s^2\ ^1S} = \int_{x_0}^{x_0+x_1} \frac{(1 - e^{-x/v\tau})}{x_1}\, dx \qquad (5.5)$$

where x_0 is the distance from the entrance aperture of the target cell to the start of the viewing region, x_1 is the length of the viewing region and v is the collision velocity. Using

calculated values for $^4P_{5/2,3/2,1/2}$ - $^1S_0$ lifetimes and assuming a statistical population for the multiplets, this correction gives experimental ^4P production cross sections that are significantly larger than ^2P production cross sections. This indicates that the 1s2s2p ^4P may be fed by cascades.

Inferred cross sections for capture into n≥2 shells of K-vacancy bearing ions in collisions with H_2, He and Ne targets are shown in figure 30a. The average ratio of these cross sections for Ne and He is 5.6 indicating an approximate scaling of capture with the number of target electrons (N_{Ne}/N_{He}=5). The trend with energy of the data agrees with the semiclassical calculation for He electron capture by C^{4+} ions, but the calculation had to be multiplied by 4.5. This is expected since the data represents capture into 1s2s ^3S configurations and the calculation assumes a structureless projectile with nuclear charge of 4+ which underestimates the true projectile potential in the region between the projectile nucleus and the spectator electron. As a result, the calculation systematically underpredicts the capture probability for small impact parameters. Other failures of the calculation are the assumption of a straight line trajectory for the projectile in the rest frame of the Helium atom, and the inability to predict partial cross sections for capture into particular nl orbitals. A calculation which would predict partial capture cross sections would be very useful in the various transfer excitation calculations shown in figure 30b.

The primary sources of systematic error in our data are uncertainty in the value of the fraction of metastable ions in the incident beam and the assumption of isotropic Auger electron emission. Isotropic emission is assumed in transforming our measured projectile Auger electron yields into absolute production cross sections (see chapter 3). Preliminary angular studies of the Auger decay of excited states formed through RTE for the O^{5+} + He system show a strong decrease in intensity as the observation angle is increased. We estimate that the absolute uncertainty in the metastable fraction values given in table 2 to be ± 10%.

In figure 30b we show the $1s2p^2\ ^2D$ - $1s^2\ ^1S$ Auger production cross sections and various calculations for capture into 2p accompanied by excitation. A maximum in the data at 5 MeV is present for all targets and agrees with the RTE resonance collision energy: $E_{RTE} = E_{Aug}(1s2p^2\ ^2D - 1s^2\ ^1S)\ M_C/m_e \approx 5.3$ MeV. The resonance width of the scaled RTE calculation describes the Helium target data well, showing that the impulse approximation is valid for the Carbon - Helium collision system. Near the 4 MeV collision energy the RTE and NTE probabilities are nearly equal and the measured cross section seems to be significantly lower than that predicted by summing the various calculations. It would be interesting to obtain more data in this region to see if there is destructive interference between RTE, NTE, and TE.

In the case of $1s2s\ ^3S$ ions, electron capture into n=2 accompanied by 1s-2p excitation results in either a $2s^22p\ ^2P$ or $2s2p^2\ ^2D$ doubly core excited configuration. The calculated Auger electron energies for the hypersatelite transitions that result when these ions decay to either $1s2s\ ^1S$ or $1s2s\ ^3S$ are shown in bold print in table 3. A maximum in the production of the doubly core excited configurations through RTE would be expected at: $E_{RTE}(^2P) = (M_C/m_e)$ (275.8 eV) = 6.1 MeV and $E_{RTE} = (M_C/m_e)$ (282.4 eV) = 6.2 MeV. Inclusive cross sections for capture into $n \geq 3$ of $1s2s\ ^3S$ ions as well as capture into n=2 accompanied by 1s-2s or 1s-2p excitation (RTE and NTE) are shown in figure 32. An increase in the data near 6 MeV is seen for all targets and is thought to be due to RTE. The spectra shown in figure 31a (Helium target) and 31b (Neon target) were measured at a collision energy of 4 MeV. At this collision energy, the probability for production of doubly core excited configurations through NTE is maximum. For both targets, nearly all of the intensity in peaks 3 and 4 are due to hypersatelite decays to $1s2s\ ^1S$. The only other likely source of Auger electrons at these energies would be from decays of $(1s2s\ ^1S)3l$ or $(1s2s\ ^1S)4\ell$ to $1s^2\ ^1S$. This is unlikely since those excited configurations are formed by electron capture into n=3 or n=4 of $1s2s\ ^1S$ projectiles and we already know that only ~10% of the incident

metastables are $1s2s\ ^1S$. Finally, a propensity for forming $2s^22p\ ^2P$ ions for collisions with Neon is seen (peaks 2 and 3).

APPENDIX

```
      PROGRAM REFOC
CCC   CALCULATES DETECTOR POSITION IN REFOCUSING DOUBLE     C
      PASS
C     PSPPA FOR GIVEN ELECTRON TRANSITION ENERGY, BEAM ENERGY,
C     AND OBSERVATION ANGLE. DETERMINES PLATE VOLTAGE FOR
C     ENERGY ANALYSIS OF ELECTRONS INCLUDING DECELERATION
C     USING INNER GAS CELL BIAS.
C
CCC         Link with library KINSUB
CCC         Subroutines called:
C     AREAD,IREAD,YREAD,RREAD,REG,ELAB,THCM,GAMA,COT,ECM

      DIMENSION EPK(16),XSEC(16)
      LOGICAL IS1,IS2,IA,IB,IDP,ISP,IPS
      INTEGER ZSEED,TSEED

      COMMON /CBIG/BIG(512,6),SBIG(20,6),IBIG(4,6)
      COMMON /CREG/K,KS,KD,KS1,KS2,KS3,IL
      COMMON /CINT/S,ES,CPT,ECPT,IA,ID,IDP,IB
      COMMON /CREAL/S1,S2,C1,C2,A,XS,YS,W1,W2,D1,D2,PHI0,PHI,
      DPHI,THL0,E0,E,EC,EC0,EPS

      DATA IB,IPS,K,IDP,METH,AMASS/-1,0,3*1,15.99491/
      DATA S1,S2,C1,C2,A,YS,DS,W1,W2,D1,D2,PHI0,DPHI,THL0,EC0,EION
           c/.189,.5669,2*2.,.25,.0945,-1.25,.063,.013,-.75,.0,30.,3.,9.553
          c,425.,12.8/
      DATA FRAD
         c/.017453293/

          XS = 0
          C = 1.961
          CN = C
          F = 1
```

```
      PHR0  = PHI0*FRAD
      SINPHI = SIN(PHR0)
      COSPHI = COS(PHR0)
      SINPH2 = SINPHI*SINPHI
      COTPHI = COT(PHR0)
      SIN2PH = SIN(2*PHR0)
      COS2PH = COS(2*PHR0)
      COT2PH = COS2PH/SIN2PH

      AYS = 2*A + YS

111       WRITE(3,1111) AMASS
1111      FORMAT(1X,'Ion mass: AMASS = ',1pg15.7,' amu (C)')
   CALL RREAD(AMASS)

          WRITE(3,1112) EION
1112      FORMAT(1X,'Ion energy: EION =',1pg15.7,' MeV (C)')
          CALL RREAD(EION)
          NKIN = 1
          IF(EION.NE.0) NKIN = 0

          EPS = EION*511003.4/AMASS/931.5012

11        WRITE(3,1011) EPS
1011      FORMAT(1X,'Reduced ion energy: EPS =',1pg15.7,' eV (C)'/)

          IF(NKIN) GOTO 12

13        WRITE(3,1013) THL0
1013      FORMAT(1X,'Lab observation angle: THL0 =',1pg15.7,' deg (C)')
          CALL RREAD(THL0)

          THR0  = THL0*FRAD
          SINTHR = SIN(THR0)
```

```
      COSTHR = COS(THR0)

12    WRITE(3,1012) EC0
1012  FORMAT(1X,'Projectile frame electron energy: EC0 =',1pg15.7,'
      c (C)')
      CALL RREAD(EC0)

      E0 = ELAB(EC0,EPS,THR0)

14    WRITE(3,1014) E0
1014  FORMAT(1X,'LAB electron energy: E0 =',1pg15.7,' eV'/)

6     WRITE(3,1006) C
1006  FORMAT(1X,'Spectrometer CONSTANT: C = E/V =',1pg15.7,' (C)')
      CALL RREAD(C)

7     WRITE(3,1007) F
1007  FORMAT(1X,'Deceleration factor: F = E/ED =',1pg15.7,' (C)')
      CALL RREAD(F)

      ED = E0/F
      VD = E0 - ED
      VP = ED/C

      T = (S1 + S2)/VP
      TSIN2P = 2*T*SIN2PH
      D0 = ED*TSIN2P

C     C1=C
C     C2=C
C     CN=C

C     V1 = E0/C1
C     V2 = E0/C2
C     T  = S1/V1 + S2/V2
```

```
C       D0   = E0*TSIN2P

        WRITE(3,1001) VD
1001    FORMAT(1X,'Deceleration bias: VD =',1pg15.7,' volts')

8       WRITE(3,1008) ED
1008    FORMAT(1X,'Electron energy in analyser: ED =',1pg15.7,' eV')

        WRITE(3,1030) VP
1030    FORMAT(1X,'Spectrometer plate voltage: VP =',1pg15.7,' volts'/)

        WRITE(3,1002)
        CALL YREAD(IDUM)

        ZETA = 0

        IF(NKIN) GOTO 31

        IB = -1

        ZETA  = -IB*GAMA(E0,EPS,THR0)

31      YF    = AYS - 2*D0*SINPH2*(COT2PH + ZETA)
        XF    = (AYS - YF)*COTPHI + D0 + XS
        RF0   = 2*D0*SINPHI*ZETA
        EDYFDE = YF - AYS + D0*SINPH2*ZETA/(1-
   SQRT(EPS/E0)*COS(THR0))
        TANALP = EDYFDE/(EDYFDE*COTPHI - D0)
        ALPHR = ATAN(TANALP)
        ALPHA = ALPHR/FRAD

        ISTEP = -RF0*8000 + 0.5
        DALPH = ALPHA -10.89339
        JSTEP = DALPH/.0075 + 0.5
```

```
      WRITE(3,1032) RF0,ISTEP
1032  FORMAT(1X,'Refocusing distance RF =',1pg15.7,' inches (C)'/
     c 1x,'Number of steps from home position (TRAN) = ',I5/)

      WRITE(3,1031) ALPHA,JSTEP
1031  FORMAT(1X,'Angle of focal line =',1pg15.7,' deg (C)'/
     c 1x,'Number of steps from home position (ROT) = ',I5/)

      THC = THCM(EC0,EPS,THR0)/FRAD

40    WRITE(3,1040) THC
1040  FORMAT(1X,'Projectile frame emission angle: THC =',1PG15.7,
     c ' deg')

      WRITE(3,1045)
1045  FORMAT(1X,'CONTINUE? (Y/N)')
      CALL YREAD(ICON)
      IF(1-ICON) GOTO 999

      E=E0

50    WRITE(3,1049)
1049  FORMAT(//1X,'Compute Projectile frame electron energy ECM'//
     c 1x,'Tag channel of peak in calibrated data area'/)

      WRITE(3,1002)
1002  FORMAT(1x,'[RET to continue]')
      CALL YREAD(IDUM)

      WRITE(3,1050) CN
1050  FORMAT(//1X,'Input spectrometer constant of tagged channel: C(N)
     c =',1pg15.7)
      CALL RREAD(CN)

      E = CN*VP + VD
```

```
      WRITE(3,1051) E
1051  FORMAT(1X,'Lab electron energy: E =',1pg15.7,' eV (C)')
      CALL RREAD(E)

      ECM = EPS + E - 2*SQRT(E*EPS)*COS(THR0)

      WRITE(3,1060) ECM
1060  FORMAT(1X,'Projectile frame energy ECM =',1pg15.7/)

      WRITE(3,1065)
1065  FORMAT(1X,'MORE ENERGIES? (Y/N)')
      CALL YREAD(IDUM)
      IF(IDUM) GOTO 50

      GOTO 999

999   END
```

REFERENCES

[1] H. Geiger and E. Marsden, *Proc. Roy. Soc. (London)* **82,** 495 (1909)

[2] H. Geiger, *Proc. Roy. Soc. (London)* **83,** 492 (1910)

[3] H. Geiger and E. Marsden, *Phil. Mag.* **25,** 605 (1913)

[4] E. Rutherford, *Phil. Mag.* **21,** 669 (1911)

[5] J. Chadwick, *Phil. Mag.* **25** (1913) 193; also, J. Chadwick and A.S. Russell, *Phil. Mag.* **27** (1914) 112

[6] P. Auger, *Compt. Rend.* **177** (1923) 169

[7] P. Auger, *J. Phys. Radium* **6** (1925) 205

[8] P. Auger, "On the discovery of a new effect", Proceedings of the X-Ray and inner shell processes conference, Journal de Physique, C9 n°12

[9] G. Wentzel, *Z. Phys.* **43** (1927) 524

[10] W. Bambynek, B. Crasemann, et. al. *Rev. Mod. Phys.* **44** (1972) 716

[11] D. Coster and R. de L. Kronig, *Physica* **2** (1935) 13

[12] T.A. Carlson and M.O. Krause, *Phys. Rev. Lett.* **14** (1965) 390

[13] V.V. Afrosimov, et. al. IX International Conf. on the Physics of Electronic and Atomic Collisions, Abstracts, eds. J.S. Risley, R. Geballe (University Press, Seattle, 1975)

[14] Auger emission takes place durring several hundred revolutions of the jumping electron, while X-ray emission , is a much slower process.

[15] W. Mehlhorn, *Phys. Lett.* **21** (1966) 155

[16] N. Stolterfoht, *Phys. Reports* **146** (19870 315, and references there in.

[17] I.A. Sellin, *Topics in Current Physics, Vol. I: Beam Foil Spectroscopy*, ed. S. Bashkin (Springer Verlag, Heidelberg, 1976) 265

[18] D.J. Pegg, *Methods of Experimental Physics, Vol. 17*, ed. P. Richard (Academic Press, New York, 1980) 529

[19] D. Schneider, R. Bruch, W.H.E. Schwarz, T.C. Chang and C.F. Moore, *Phys. Rev.* **A15** (1977) 926

[20] D. Schneider, R. Bruch, W. Butscher and W. Schwarz, *Phys. Rev.* **A24** (1981) 1223

[21] M. Rodbro, R. Bruch and P. Bisgaard, *J. Phys.* **B12** (1979) 2413

[22] K.T. Chung, *Phys. Rev.* **A20** (1979) 1743

[23] K.T. Chung, *Phys. Rev.* **A28** (1983) 1418

[24] K.T. Chung, *Phys. Rev.* **A31** (1985) 310

[25] G.M. Thomson, W.W. Smith and A. Russek, *Phys Rev* **A7** (1973) 168; also, S. Hagmann, et. al., "Electronic and Atomic Collisions", eds. J. Eichler, I.V. Hertel and N. Stolterfoht (North-Holland, Amsterdam, 1984) p. 385

[26] A. Itoh, T. Schneider, G. Schiwietz, Z. Roller, H. Platten, G. Nolte, D. Schneider and N. Stolterfoht, *J Phys* **B 16** (1983) 3965

[27] J. Newcomb, T.R. Dillingham, J. Hall, S.L. Varghese, P.L. Pepmiller and P. Richard, *Phys Rev* **A29** (1984) 82

[28] M. Terasawa, T.J. Gray, S. Hagmann, J. Hall, J. Newcomb, P. Pepmiller and P. Richard, *Phys. Rev.* **A27** (1983) 2868

[29] T.R. Dillingham, Doctoral Dissertation, Kansas State Univ. 1983 (unpublished) also, see references 27 and 28 above

[30] J.A. Tanis et. al., *Phys. Rev. Lett.* **47**, (1981) 828

[31] P.L. Pepmiller et. al., *Phys. Rev.* **A31**, (1985) 734

[32] Although the thermal root-mean-square velocity of H2 and He gas atoms at 0°C is ~1800 and 1340 m/s respectively, ion velocities ar of the order of $1x10^6$ m/s in the region where RTE is important.

[33] D. Brandt, *Phys. Rev.* **A27**, (1983) 1314

[34] J.M. Feagin, J.S. Briggs and T.M. Reeves, *J. Phys.* **B 17** (1984) 1057

[35] D.J. McLaughlin and Y. Hahn, *Phys. Lett.* **88A** (1982) 394

[36] A. Itoh et. al., *J. Phys.* **B18**, (1985) 4581

[37] J.K. Swenson et. al., *Phys. Rev. Lett.* **57** (1986) 3042

[38] J.K. Swenson, J.M. Anthony, M. Reed, M. Benhenni, S.M. Shafroth, D.M. Peterson and L.D. Hendrick, *Nucl. Instr. and Meth.* **B24/25** (1987) 184

[39] J.M. Anthony et.al., *J. de Phys,* **C9** (1987) 301

[40] J.K. Swenson, Nucl. Instr. and Meth. **B10/11** (1985) 899

[41] L. Goldberg, *Physics Today* **41 no. 8** (1988) 38

[42] General Ionex Corporation model #834 high brightness negative sputter ion source

[43] Brookhave Corporation Model 1000

[44] P. Bachmann, A. Eberlein and R. Bruch, *J. Phys. E: Sci. Instr.* **15** (1982) 207

[45] J.P. Soderstrum, M.A. Boyd, C. Gould, R. Roberson, *XSYS Reference Manual*, Duke University, Durham, N.C. 27706

[46] Computer Automated Measurement And Controle (IEEE-583) is an internationally accepted interface standard. Various modules such as digital and analog converters; scaler counters; waveform recorders etc. are avaliable commercially from numerous vendors.

[47] C.R. Gould et. al., *IEEE Trans Nucl Sci,* **NS-32** (1985) 1447

[48] Stanley Cohen and Steven C. Pieper, *The Speakeasy III Reference Manual*, (Speakeasy Computing Corporation, 22 West Adams Street, Chicago 1980)

[49] Delta electrons were named before their origin was clearly understood (ie. alpha rays, beta rays etc). They are simply electrons that were initially bound to a projectile or target atom are ionized during the collision process. Depending on the amount of energy absorbed from the collision partner, their intensity distribution only depends weekly on kinetic energy.

[50] J.L. Wiza, *Nucl. Instr. and Meth.*, **162** 587 (1979)

[51] M. Lampton and F. Paresco, *Rev. Sci. Instr.*, **45** 1098 (1974)

[52] E. Mathieson, et. al., *Nucl. Instr. and Meth.*, **121** 139 (1974)

[53] J.K. Swenson, Ph.D. Dissertation, University of North Carolina (1983) (unpublished)

[54] C. J. Borokowski, and M.K. Kopp, *Rev. Sci. Instr.*, **46** 951 (1975)

[55] E. Mathieson, *Nucl. Instr. and Meth.* **97** 171 (1971)

[56] Tenelec Corporation Model TC446

[57] J.M. Anthony, et al, *Bull. of the Amer. Phys. Soc.* **31** (1986) 1757

[58] W. Bombeynek, B. Crasemann, R.W. Fink, H.U. Freund, H. Mark, and P.V. Rao, *Rev. Mod. Phys.* **44** (1972) 716

[59] R.H. McKnight and R.G. Rains, *Phys. Rev. A* **14** (1972) 1388

[60] See reference 17 above, and references there in.

[61] M.E. Rudd, T. Jorgenson Jr., and D.J. Volz, *Phys. Rev. Lett.* **16** (1966) 929

[62] Yu. S. Gordeev and G. N. Ogurtsov, *Zh. Eksp. Teor. Fiz.* **60** (1971) 2051 [Sov. Phys.-JETP **33** (1971) 1331]

[63] M.E. Rudd and J. Macek, *Case Studies in Atomic Physics, Vol. 3,* eds. E. W. McDaniel and M.R. C. McDowell (North-Holland, Amsterdam, 1973) p.47

[64] J.S. Risley, A.K. Edwards, R. Geballe, *Phys. Rev.* **A 9** (1974) 1115

[65] N. Stolterfoht, D. Schneider, D. Bruch, B. Aagaard, E. Boving and B. Fastrup, *Phys. Rev.* **A 12** (1975) 1313

[66] R.Bruch, K.T. Chung, W.L. Luken, J.C. Culberson, *Phys. Rev.* **A31** (1985) 310

[67] K.T. Chung and B.L. Davis, *Private Communication,* (1987)

For method, see reference 20 above.

[68] R. Mann, *Phys Rev* **A 35** (1987) 4988 also, H. Cederquist, et al, *J Phys* **B 18** (1985) 3951

[69] T.R. Dilingham, J. Newcomb, James Hall, P.L. Pepmiller and Patrick Richard, *Phys Rev* **A 29** (1984) 3029

[70] D. Brandt, *Nucl Instr and Meth*, **214** (1983) 93, also, M.W. Clark, J.K. Swenson, S.M. Shafroth, *Phys Rev Lett* (1985)

[71] H. Knudsen, H.K. Haugen and P. Hvelpund, *Phys Rev* **A 24** (1981) 2287

[72] C.D.H. Chisolm, A Dalgarno and F.R. Innes in *Advances in Atomic and Molecular Physics*, edited by D.R. Bates (Academic, New York 1969) Vol 5, pg 297

[73] T.L. Mcabee, *Nucl Inst and Meth* **214** (1983) 89

[74] K.T. Chung and B.F. Davis, *Private communication*